The Age of the Milky Way Halo Stars
– Implications for Galaxy Formation –

Paula Jofré Pfeil

München 2010

The Age of the Milky Way Halo Stars
– Implications for Galaxy Formation –

Paula Jofré Pfeil

Dissertation
an der Physik Fakultät
der Ludwig–Maximilians–Universität
München

vorgelegt von
Paula Jofré Pfeil
aus Santiago de Chile

München, den 30 September 2010

Erstgutachter: Dr. Achim Weiss

Zweitgutachter: Dr. Markus Kissler-Patig

Tag der mündlichen Prüfung: 10. Dezember 2010

Contents

Zusammenfassung

Das Studium der Verteilung von Sternen in der Milchstraße anhand der Daten des Sloan Digital Sky Survey (SDSS) liefert nicht nur Hinweise zu ihrer Bildung, sondern beantwortet auch Fragen zur Sternstruktur. Ziel dieser Arbeit ist die Bestimmung des Alter der Sterne, die sich im Halo der Milchstraße befinden. Dazu werden Hauptreihensterne in der Nähe des Abknickpunkts (engl. turn-off) im Hertzsprung-Russell Diagramm analysiert. Die Betrachtung von Sternen nahe des Abknickpunktes ist weitverbreitet in Altersbestimmungen von Kugelsternhaufen, weil Alter und auch Metallizität an diesem Punkt sensitiv zu Änderungen von der Leuchtkraft und der effektiven Temperatur sind. Um die effektive Temperatur und Metallizität aus etwa einhunderttausend Sternspektren des SDSS in einem angemessenen Zeitrahmen zu bestimmen, ist ein effizienter Algorithmus erforderlich. Dafür wurde eine Datenskompressionsmethode angewendet, welche die effektive Temperatur und Metallizität dieser Sterne mit einer Genauigkeit von 120 K bzw. 0.25 dex bestimmt.

Der Abknickpunkt für die jüngste Sternpopulation konnte mit hoher Genaugkeit als Funktion der Metallizität abgeleitet werden. Dabei wurden die heißesten Sterne der Sternpopulation mit einer künstlichen Sternverteilung gleicher Metallizität verglichen. Mit Hilfe von Isochronen aus der Theorie der Sternentwicklung wurde mit den SDSS Daten ein innerer Galaktischer Halo mit einer dominanten Sternpopulation gefunden, welcher keinen Gradienten in seinem Alter bezüglich der Metallizität aufweist. Daraus kann man schließen, dass die dominante Sternpolulation sich sehr schnell, wahrscheinlich während eines Kollapses von proto-galaktischem Gas, gemäß des Szenarios von Eggen (1962) gebildet haben könnte. Weiterhin wurde eine signifikante Anzahl von heißen Sternen am Abknickpunkt gefunden, welche als junge Sterne aus Zwerggalaxien interpretiert werden, die später von der Milchstraße akkretiert worden sind. Diese Interpretation stützt das hierachische Galaxienbildungsmodell von Searle & Zinn (1978).

Motiviert von der gegenwärtigen Debatte in der Theorie der Sternstrukturbildung über das gravitative Absenken von Helium in alten sonnenähnlichen Sternen (atomare Diffusion), wurden für die Altersbestimmung der Halosterne Isochrone mit und ohne atomarer Diffusion verwendet. Diffuse Isochrone lieferten ein Alter der Halosterne von 10 bis 11 Gigajahren. Dieses Alter stimmt mit dem absoluten Alter der Kugelsternhaufen überein. Kanonische Isochrone, ohne Diffusion, lieferten ein Alter vom 14 bis 16 Gigajahren, was im Konflikt mit dem Alter des Universums von 13.7 Gigajahren steht. Dies widerspricht der Annahme, dass atomare Diffusion in alten Halosternen unterdrückt ist.

Abstract

This thesis is about the study of stellar populations of the Milky Way Galaxy using the Sloan Digital Sky Survey (SDSS). The aim was to determine the age of the stellar content of the Galactic halo by considering main-sequence turn-off stars. The turn-off point in the Hertzsprung-Russell diagram is a broadly-used age-indicator in globular clusters, because the color and luminosity at that point are mainly sensitive to age and metallicity. From the immense number of halo stars provided by SDSS, we could accurately detect the turn-off as a function of metallicity, which was done by analyzing the hottest (bluest) stars of a population with the same metallicity. In order to analyze a sample of 100,000 SDSS low resolution stellar spectra an efficient tool was required, which had to be automatic and quick, in order to retain metallicities and temperatures in a timely manner. For this purpose, we employed a data-compression method and estimated metallicities and effective temperatures with accuracies of 0.25 dex and 120 K, respectively.

We looked for the isochrones with turn-off temperature and metallicity of the field stars and found that our stellar sample consisted of one dominating population, with no age gradient as a function of metallicity. This means that the dominating population of the Galactic halo formed rapidly, probably during the collapse of the proto-Galactic gas, according to the Milky Way formation scenario proposed by Eggen et al. (1962). Moreover, we could find a significant number of stars with hotter temperatures than the turn-off, which might be explained as young stars formed in dwarf galaxies and accreted later on to our Milky Way. These stars may be an evidence for the current hierarchical galaxy formation scenarios, as proposed by Searle & Zinn (1978).

Motivated from the current debate about the efficiency of gravitational settling (atomic diffusion) in the interior of old solar-type stars, we used isochrones with and without settling to determine the ages. When using canonical isochrones we obtained ages of 14-16 Gyr. This result is a strong argument against fully-inhibited diffusion in old halo field stars, because if the efficiency of diffusion would be completely inhibited, then the age of these stars would be in serious conflict with the age of the Universe of 13.7 Gyr. The age obtained using diffusive isochrones were of 11-12 Gyr, which is in agreement with the absolute age of the old globular clusters in the inner halo.

Chapter 1

Introduction

Stars are the candles of the sky enclosing exquisite information about the formation and evolution of the galaxies and therefore about the Universe. The more we want to know about the details of the Universe, the better we must understand the stars. The theory of stellar structure and evolution, compared to other fields in astrophysics, is believed to be a mature and well-understood topic. Observations, however, become more accurate every day, and put in check many different aspects in the understanding of the stars.

Our home Galaxy, the Milky Way, offers a unique opportunity to set constraints on theories of stellar structure and evolution, because only in the Milky Way can we observe a large spectrum of stars with high accuracy. It is also only in the Milky Way where we can obtain true three-dimensional stellar spatial density distributions, stellar kinematics and stellar chemical compositions, thereby making our Galaxy a precious laboratory to test the theories of formation and evolution of galaxies. The knowledge of how stars move and how they are distributed in space constrains the Galactic gravitational potential, while the knowledge of their ages and chemistry constrains the star formation history.

Counting stars is one of the few truly classical scientific techniques used to study Galactic structure. Star counts have been used in astronomy for over a century to derive the structure of the Milky Way (Kapteyn & van Rhijn 1920; Gilmore et al. 1989; Croswell et al. 1991; Morrison et al. 2000; Bond et al. 2010). They have led to the conclusion that the Milky Way has different stellar components, such as a central bulge; a thin and a thick disk; and an inner and an outer halo. In the current cosmological simulations of Springel et al. (2006, and references therein), galaxies form hierarchically through the merging of small proto-systems. The Galactic halo is the external part of the Galaxy, that it why is exposed to interactions with the neighbors of the Local Group. This makes the Galactic halo important when studying these hierarchical scenarios. In addition to that, the halo contains the most metal-poor stars in the Galaxy and also some of the oldest ones. Low-mass stars evolve slowly, in timescales larger than the age of the Universe, which means that the old halo stars observed today in the sky contain a fossil record of Milky Way history.

The debate of how the Galaxy was formed is principally based on two classic works. The first one, by Eggen et al. (1962), consists of the analysis of the photometry and kinematics

of nearby stars and concludes that the Galactic halo formed during a rapid, monolithic collapse of the proto-Galactic gas cloud. The second formation scenario was proposed by Searle & Zinn (1978). Based on studies of globular clusters metallicities and horizontal branch morphologies, they claimed that the halo was formed via accretion of small galaxies over several Giga-years (Gyr) in a rather chaotic manner. These contrasting theories have been the subject of critical discussions in astrophysics during the last few decades (see e.g. the reviews of Majewski 1993; Helmi 2008). The knowledge of accurate and absolute ages for the various stellar populations plays an important role in finding the timescale for the formation of the Galactic halo.

The most popular method to determine ages is through stellar evolutionary models. It consists of a comparison between observed stars and calculated isochrones in the Hertzsprung-Russell (HR) diagram, which relates the temperature with the luminosity of the stars. These two properties are mainly dependent on the mass of the star. An isochrone is a curve along the HR diagram of stars with different mass but the same age and chemical composition. When determining the age of a star by this method, its accurate chemical composition, effective temperature, surface gravity and distances (the latter two tell us about the mass and luminosity) are imperative to place the star in a restricted region of the HR diagram. On the other side, stellar evolutionary models must provide an accurate isochrone in order to date the star in a correct time frame.

As extensively discussed in the literature and recently reviewed by Soderblom (2010), uncertainties in the observations of distant halo stars do not allow us to place them in a confined area in the HR diagram. Stellar evolution models also do not provide isochrones accurate enough to constrain the age of the stars.

From the observational point of view, stellar atmosphere parameters are estimated usually by photometry or spectroscopy. When using photometry, empirical calibrations, such as those of Alonso et al. (1996) and Ramírez & Meléndez (2005), are used to transform the observed colors to metallicities and temperatures. The observed magnitude, together with the distance of the star, provide the luminosity. In the case of halo stars, the distances are poorly known and therefore luminosities can have large errors. When using spectroscopy, the analysis of absorption lines of stellar spectra ideally yield all atmospheric parameters. Although this method is independent of distance – theoretically, because for distant faint stars it becomes difficult to retain good spectral quality – it is entirely dependent on the modeling of stellar atmospheres. This modeling introduces errors as well, since the atmosphere models are created under assumptions that can differ significantly from reality, such as local thermodynamical equilibrium (Asplund 2005).

From the theoretical point of view, we do not understand the evolution of stars well enough. The effects of uncertainties in convection and gravitational settling of heavy elements are far from being well understood (Weiss 2002). In particular, the settling of heavy elements towards the stellar center (also called atomic diffusion) leads to chemical changes in the surface and increases the mean molecular weight in the center. This results in a decrease of the effective temperature in the hydrogen-burning phase. The efficiency of this phenomenon in old solar-type stars is currently under debate in stellar astrophysics

(Proffitt & Vandenberg 1991; Salaris et al. 2000; Gratton et al. 2001; Korn et al. 2006). This effect can significantly change the absolute age of old metal-poor stars, leading to up to 4 Gigayear (Gyr) of difference for turn-off field stars depending on whether diffusion is considered or not in the isochrones applied. The determination of the age of individual stars is therefore one of the most difficult measurements in astrophysics. These ages are rarely known to an accuracy better than twenty percent (Gustafsson & Mizuno-Wiedner 2001). This is especially true for old distant stars in the Galactic halo, which is a major obstacle in the exploration of early Galactic history.

Until recently, globular clusters (GC) were the main tracers of the Galactic halo, (see e.g. Searle & Zinn 1978; Chaboyer et al. 1996; Sarajedini et al. 1997). The reason to use GC's is simply because clusters can be treated as a sample of stars with the same age, metallicity[1] and distance; and therefore their properties (in particular the ages and distances) can be better studied than for individual stars. This picture has changed in the last years thanks to the improvement made in the quality of the observations. We are entering a completely new era of Galactic astronomy, where we are reaching an unimaginable view of the Milky Way, mainly due to the immense number of stars collected by current stellar surveys. Those with large impact in the Galactic astronomical community have been the *Hipparcos* satellite (ESA 1997) and the Geneva-Copenhagen survey of the solar neighborhood (Nordström et al. 2004), which have measured distances, proper motions, ages, chemical abundances, etc. of thousands of stars. The HK objective-prism[2] (Beers et al. 1992) and the Hamburg/ESO surveys (Christlieb et al. 2001) are focused on spectroscopic studies of the most metal-poor stars in the Galaxy. But the revolution in the topic is thanks to the data of the Sloan Digital Sky Survey (SDSS, York et al. 2000) and in particular the Sloan Extension for Galactic Understanding and Exploration (SEGUE, Yanny et al. 2009b). These surveys yielded the largest sample of Galactic stars ever, providing more than 240,000 objects with multi-color photometry and spectroscopy. SDSS/SEGUE has mapped a large part of the sky reaching deep regions of the Galactic halo.

The results of the analysis of these deep wide surveys, combined with the better confidence achieved for parameters for GC's in the last years, are reaching a common conclusion about the formation of the Galactic halo. For example, Salaris & Weiss (2002) and De Angeli et al. (2005) using globular clusters; and Schuster et al. (2006) and Carollo et al. (2007) using field halo stars, agree that both authors, Eggen et al. (1962) and Searle & Zinn (1978), are partially right, e.g. one part of the Galactic halo (inner halo) was formed during the initial collapse, whereas the other part (outer halo) was formed slowly and chaotically via accretion. However, the importance of the later infall and accretion, remains to be quantified and the knowledge of absolute ages for the different stellar populations is still key information in this puzzle.

---

[1]Gratton et al. (2004) wrote a review about the evidences for multiple populations in GC's, showing that they actually are not simple at all. As tracers of the Galaxy, they can still be approximated as simple populations.

[2]"HK" is the name that comes from the metallicity determination using the spectra the absorption H & K calcium lines (Beers et al. 1985).

On the determination of absolute ages for the Galactic field halo stars

One of the most beautiful aspects of science is to consider alternative options and be able to come up with solutions and answers of what appears to be impossible. This thesis aims to obtain ages for the field stellar populations of the Galactic halo and contribute to the understanding of the formation and structure of the Milky Way.

Even considering that we do not know the distance and mass of distant halo stars with enough accuracy, we can still estimate ages of stellar populations by looking at a crucial evolutionary point: the main-sequence turn-off. It is defined as the point where the star leaves the main-sequence phase (i.e. the hydrogen in the core is exhausted) to become a red giant. A turn-off star has the highest effective temperature for the main part of its evolution. In a dominating coeval stellar population of a certain metallicity, the turn-off point corresponds to the stars with the *highest* temperature and the isochrone with this turn-off temperature represents its age, independently of the distance and mass of these stars. The only requirement is to have a large sample of stars, from where the hottest ones can be found. This approach to estimate the age can be visualized in Fig. 1.1, where the upper panel is an HR diagram with a theoretical isochrone of 11 Gyr and metallicity of
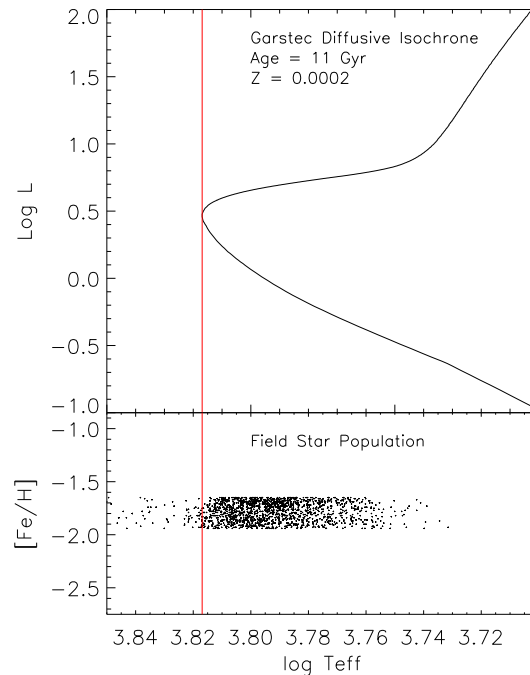
Figure 1.1: Lower panel: Effective temperature of a SDSS field star population with metallicities in the range of $[Fe/H] = -1.70 \pm 0.15$. Upper panel: 11 Gyr isochrone with metal fraction $Z = 2 \times 10^{-4}$, which corresponds to the metallicity of the field population. The turn-off point of the isochrone is represented by the vertical red line, which agrees with the hottest stars of the field population. This agreement suggests an age 11 Gyr for the field stars at the turn-off.

[Fe/H] = −1.70. The lower panel shows the temperature distribution of SDSS halo field stars at the metallicity of the isochrone. The red vertical line is the turn-off of the 11Gyr isochrone from the upper panel, which agrees with the hottest stars of the field population. This suggests an age of 11 Gyr for this population. It is important to mention here that this method is affected by uncertainties too. The effective temperatures, for example, are difficult to obtain more accurate than 100 K. The effective temperature depends on the atmosphere model and also on internal convection processes, which are uncertain too. Globular clusters ages are determined using the turn-off luminosity, which is a more robust theoretical quantity than the turn-off temperature (Meissner & Weiss 2006). Being aware of these uncertainties, we still can give an age estimate of the Milky Way halo and discuss implications of Galaxy formation.

The general methodology of this approach is: Firstly, select a sample of halo stars and estimate their stellar atmosphere parameters, in particular the effective temperature and metallicity. Secondly, indentify the main-sequence turn-off and determine ages and thirdly, calibrate the ages to absolute values. Although this methodology seems simple and straight-forward, on the way one has to face many different and independent aspects of stellar and Galactic astrophysics. For this reason, this thesis consists of chapters separated into single topics, each of them containing an introduction (or motivation) and a summary with conclusions. Like this the reader is free to read the chapters independently. The basic structure, particular data and models employed in the course of this thesis, together with the main achievements are summarized for these three points below.

1. *Massive Spectroscopy*: The rich number of stars with spectroscopy and photometry from SDSS and SEGUE is not yet completely exploited. This project uses these stars to determine the ages. In order to estimate the atmosphere parameters from such a large amount of data an appropriate tool was created, which is automatic and quick. A large part of the project was spent in developing this tool, because in order to obtain accurate parameters, we had to understand the details of technical and fundamental stellar spectroscopy. The MAssive compression of χ^2 for stellar spectra (MAχ, Jofré et al. 2010) is an algorithm that returns estimates for metallicity, effective temperature and surface gravity from low and high resolution spectra. A detailed description of MAχ is found in Chap. 2; the application of this method to SDSS spectra is described in Chap. 3, while a test with high-resolution spectra can be found in Chap. 4. The first main achievement of this thesis was the experience gained in analyzing large spectroscopic data sets, as well as the excellent performance of this algorithm in processing stellar spectra automatically. The MAχ code is a powerful new tool in the modern era of Galactic astronomy, where the Milky Way is being scanned through massive spectroscopic surveys.

2. *Isochrone age determination*: Chapter 5 contains an extensive study of the identification of the main-sequence turn-off for the SDSS/SEGUE halo stars with temperatures and metallicities obtained with the MAχ method. The ages for this turn-off

temperature are determined in Chap. 6. This method has been employed before by Unavane et al. (1996), Allende Prieto et al. (2006) and (Schuster et al. 2006, and references therein), although none of them has fully exploited the theoretical aspects of the isochrones employed to determine ages. As introduced above, the turn-off temperature is much affected by the sedimentation of heavy elements. Another milestone is that we found a reduction of 4 Gyr due to atomic diffusion in the age determination of metal-poor field halo stars using the Garching Stellar Evolutionary Code (GARSTEC; Weiss & Schlattl 2008). The result explains the different ages obtained by the previous works of the literature. When considering diffusion in the isochrones, we obtained an age for the dominating halo field population of 11-12 Gyr.

3. _Globular Clusters as calibrators_: Chaboyer et al. (1992a) explored the different age-dating techniques for globular clusters and concluded that those which do not depend on the turn-off temperature are unaffected by atomic diffusion. If the halo field stars and globular clusters share a similar history, then absolute ages of globular clusters can be used to calibrate ages for the halo field. Observational evidences for a common age between clusters and field stars are presented in Chap. 7, where we also compare our results for the field stars with those for GC's.

The relevance and innovation of this work, especially in the contribution to the understanding of the structure and formation of the Milky Way halo, is finally summarized in Chap. 8.

Chapter 2

MAχ

The **MA**ssive compression of χ^2 for stellar spectra (MAχ, Jofré et al. 2010) is a method that allows fast estimates of stellar atmosphere parameters with sufficiently high accuracy. This chapter contains a summary of the technique developed principally by Mark Tegmark, Alan Heavens, Raul Jimenez and Ben Panter (Tegmark et al. 1997; Heavens et al. 2000; Panter et al. 2003) and also explains the MAχ code in Appendix A. Although some algorithms and routines were originally written by Ben Panter, the code has been mainly written during this work. The reason for the development of this code from scratch is that this is the first time that the compression algorithm is applied directly on stellar spectra, for the specific task of effective temperature and metallicity estimation from SDSS/SEGUE stars.

2.1   Overview and Motivation for MAχ

The use of the main-sequence turn-off (MSTO) is crucial to the determination of age for field stars when the distance and mass cannot be measured accurately enough. This can be done when a large sample of a dominating star population is available, because the turn-off can be found by looking at the hottest stars.

To estimate the age of the MSTO field halo stars, it is therefore necessary to know previously the metallicity and temperature independently. The stellar surveys SDSS (York et al. 2000) and SEGUE (Yanny et al. 2009b) contain spectra of more than 240,000 stars from where these properties can be estimated. In 2006, when this project began, the SEGUE stellar atmosphere parameters pipeline for the SDSS stellar spectra was not published so we had to came up with a method to process the spectra. Also, an integrated analysis is worthwile to check the reliability of the pipeline. A multiple parameter estimation from the SDSS/SEGUE spectra, each with more than 3000 flux measurements, becomes extremely time-consuming if it is done through a classical spectral fitting with a brute-force search in the multi-dimensional likelihood surface, even more so if one wants to explore the errors on the recovered parameters. It was of prime importance to create an efficient and automatic tool capable of producing robust results in a timely manner.

Efforts to reduce the computational burden of characterizing the likelihood surface include Markov-Chain Monte-Carlo methods (Ballot et al. 2006), where the exploration of the likelihood surface is done by evaluating certain points that follow a random chain which determine finally the global solution. An alternative method is to start at an initial estimate and hope that the likelihood surface is smooth enough that a gradient search will converge on the solution. An example of this approach can be found in Allende Prieto et al. (2006) and Gray et al. (2001), based on the Nelder-Mead downhill simplex method (Nelder & Mead 1965), where the derivatives of the likelihood function give the direction toward its maximum. In both cases, the likelihood is evaluated only partially, leaving large amounts of parameter space untouched. Moreover, the time needed to find the maximum depends on the starting point and the steps used to evaluate the next point. Another efficient parameter estimation method utilizes neural networks, for example Snider et al. (2001) and Re Fiorentin et al. (2007). While these non-linear regression models can obtain quick accurate results, they are entirely dependent on the quality of the training data, in which many parameters must be known previously. Careful attention must also be paid to the sampling of the model grid which is used to generate the neural network.

An alternative approach to spectral analysis is the Massively Optimized Parameter Estimation and Data compression method (MOPED[1], Heavens et al. 2000). This novel approach to the maximum likelihood problem involves compressing both data and models to allow very rapid evaluation of a set of parameters. The evaluation is fast enough to do a complete search of the parameter space on a finely resolved grid of parameters. Using

---

[1]MOPED is protected by US Patent 6,433,710, owned by The University Court of the University of Edinburgh (GB)

carefully constructed linear combinations, the data is weighted and the size is reduced from a full spectrum to just one number per parameter. This number, with certain caveats (discussed later), encapsulates all the information about the parameter contained in the full data.

The idea of applying the MOPED method to the parameter estimation of stellar spectra from the SDSS survey appear straightforwardly because of the success of MOPED in processing SDSS galaxy spectra (Panter et al. 2003). The creation of a derivative of MOPED (termed MAχ in the following) as a new specific tool, was necessary because to estimate the metallicity history of a galaxy for instance, MOPED needs models where the spectra are the sum of single stellar populations. This work, on the contrary, consists in the study of single populations, meaning the metallicity has to be estimated from the spectrum of each individual star.

In this chapter we describe the application of the method to determine parameters from stellar spectra. A history of the method to compress large datasets can be found in Sect. 2.2 followed by a description of its mathematical formalism in Sect. 2.3. Section 2.4 explains the steps needed to analyze stellar spectra using the compression algorithm and a documentation of the MAχ code is found in Appendix. A. Finally, a summary and conclusions of this chapter are given in Sect. 2.5

2.2 History of the MAχ data-compression method

One of the first situations where the acceleration of a likelihood surface analysis became necessary was the discovery of fluctuations in the cosmic microwave background (CMB) by the *Cosmic Background Explorer* satellite (*COBE*; Smoot et al. 1992). At that time, galaxy redshift surveys started to became popular, especially the Sloan Digital Sky Survey York et al. (2000). CMB maps and galaxy surveys have produced such large data sets that a large number of sophisticated data-analysis methods were developed specifically to tackle them.

The Karhunen-Loève (KL) eigenvalue method Karhunen (1947) is a data- compression method that has been applied successfully for both CMB maps and galaxy redshift surveys. An extensive description and discussion of this method, together with applications to the data sets mentioned above, can be found in Tegmark et al. (1997) and Bond (1995). This method consists basically of a linear data compression that can be performed by the multiplication of the data with weighting vectors. These vectors are chosen carefully such that no information is lost or gained through the compression. This condition is treated with an eigenvalue problem, where the solution gives the shape of the weighting vectors.

A direct application of the KL method was employed then by Heavens et al. (2000) in MOPED for the simultaneous estimation of multiple parameters from galaxy spectra. They showed that if the noise of the spectra behaves as a Gaussian, then the KL method results in a lossless compression of the multi-dimensional likelihood surface. Ben Panter's PhD thesis[2] consisted in using MOPED to determine parameters such as star formation and

---

[2]http://www.era.lib.ed.ac.uk/handle/1842/774

metallicity of over 37,000 galaxy spectra from the Early Release of Sloan Digital Sky Survey. Furthermore, Panter et al. (2003) demonstrated that recovering these parameters for such a large sample becomes intractable without data compression methods, particularly the exploration of the likelihood surface.

Later releases of SDSS brought the attention to the stellar community, where a significant product of the survey were resolved stellar spectra from our Galaxy combined with deep, accurate multicolor photometry. In this work we process over 140,000 stellar spectra with the KL eigenvalue method to determine stellar parameters such as effective temperature, metallicity and surface gravity. We called this application MAχ; it was introduced recently to the astronomical community in Jofré et al. (2010).

In addition to MAχ, two other derivatives of MOPED have been created in the last years. The first one is VESPA (Tojeiro et al. 2007), a modern version of MOPED, which handles better the errors in the galaxy spectra measurements of later SDSS releases and allows an even faster parameter estimation than MOPED. The second one is the creation of the company Blackford Analysis[3] where Ben Panter, Alan Heavens and collaborators have applied the MOPED algorithm to medical images analyses.

2.3 Description of the MAχ method

This section describes the KL method used by MAχ to treat a likelihood surface of three stellar atmosphere parameters. It contains first a brief review of the classical maximum-likelihood method, where a parametric model is used to describe a set of data. Then it presents the algorithm that compresses the data, which speeds up the likelihood surface exploration. Finally, a subsection is dedicated to show for the lossless nature of the compression procedure. The purpose here is not to rewrite of what is published in Tegmark et al. (1997)[hereafter T97] and Heavens et al. (2000)[hereafter H00], but to describe the procedure in the direct application of stellar spectra (see also Jofré et al. 2010).

2.3.1 Maximum likelihood description

Suppose the data – e.g. the flux of a spectrum – are given by N real numbers $x_1, x_2, ..., x_N$, which are arranged in an $N-$dimensional vector $\mathbf{X}$. They represent the flux measurements at N wavelength points. It is possible to treat each data point x_i of the spectrum as a signal part μ_i and a noise contribution σ_i

$$x_i = \mu_i + \sigma_i. \tag{2.1}$$

Assuming that the measurements of the spectrum have a noise with zero mean, $\langle \mathbf{X} \rangle = \langle \boldsymbol{\mu} \rangle$, $\mathbf{X}$ is a random variable of a probability distribution $L(\mathbf{X}, \boldsymbol{\Theta})$, which depends in a known way on a vector $\boldsymbol{\Theta}$ of m model parameters. In the present case $m = 4$ with

$$\boldsymbol{\Theta} = (\theta_1, \theta_2, \theta_3, \theta_4) = ([\text{Fe/H}], \text{T}_{\text{eff}}, \log g, A_s), \tag{2.2}$$

---

[3]http://blackfordanalysis.com/

with the first three ones representing the physical parameters iron abundance [Fe/H] (see Sect. 6.2.2 for definition), effective temperature T$_{\text{eff}}$ and surface gravity $\log g$. The last one, called *scaling factor for normalization A_s*, represents an internal fitting property (see below). A certain combination of θ_j ($j = 1, 2, 3, 4$) produces a theoretical model $\mathbf{F} = \mathbf{F}(\mathbf{\Theta})$, which can be used to build an m-dimensional grid of models by varying the θ_j parameters. To estimate parameters, the major interest is to test whether the observed data supports the modeled parameter values for each grid point. If the noise in the measurements distributes as a Gaussian and the parameters have uniform priors, then the likelihood

$$L_f(\mathbf{X}, \mathbf{\Theta}) = \frac{1}{(2\pi)^{N/2}\sqrt{\sigma_{\text{av}}^2}} \exp \frac{-\chi^2}{2} \tag{2.3}$$

gives the probability for the parameters, where σ_{av}^2 is the averaged square of the noise of each data point and

$$\chi^2 = \sum_{i=0}^{N} \frac{(F_i - \mu_i)^2}{\sigma_i^2} \tag{2.4}$$

is the chi-square goodness-of-fit (Pearson 1900). The chi-square statistics provides a non-parametric test for comparing data and model. For reviews of the chi-square distributions and its use in likelihood analyses see Babu & Feigelson (1996) and Press (1993). The position of the maximum in the likelihood estimates the set of parameters $\mathbf{\Theta_0}$ that best describe the data $\mathbf{X}$. The fit between $\mathbf{F}(\mathbf{\Theta_0})$ and $\mathbf{X}$ is good if $\chi^2 < \text{DOF}$, where $\text{DOF} = N - m$ are the degrees of freedom. In the most basic form one finds the maximum in the likelihood surface by exploring all points in the parameter space, with each likelihood estimation calculated using all N data points. This procedure is of course very time-consuming if N and m are large.

2.3.2 Karhunen-Loève data compression

In practice, not all data points carry information about the parameters, because either they are noisy or not sensitive to the parameter under study. The KL algorithm uses this knowledge to construct weighting vectors which neglect some data without losing information. A way to do this is by forming linear combinations of the data. The procedure to compress the information of a given parameter θ_j from a spectrum is explained below.

The idea is to capture as much information as possible about θ_j. The definition of the weighting vector $\mathbf{b}_j = (b_{j,1}, b_{j,2}, ..., b_{j,N})$ is

$$\mathbf{b}_j = \frac{1}{|\mathbf{b}_j|} \frac{1}{\sigma^2} \frac{\partial \mathbf{F}}{\partial \theta_j}, \tag{2.5}$$

where $|\mathbf{b}_j| = \sqrt{\mathbf{b}_j \cdot \mathbf{b}_j}$. This definition assures that each data point of the spectrum is less weighted if σ is large and more weighted if the sensitivity in the flux – meaning the

Table 2.1: Strong absorption lines of a typical spectrum at SDSS resolution of a F-G dwarf star. The first column indicates the name of the line and the second its wavelength position in Å.

line	CaIIK	CaIIH	Hδ	G band	Hγ	Hβ	MgIb triplet
λ Å	3933	3969	4101	4300	4340	4861	5183

derivative of $\mathbf{F}$ respect to the parameter θ_j – is high. The creation of this vector needs, on one hand, the information about the behavior of the parameters from a theoretical fiducial model, and on the other hand, the error measurement from the data.

Figure 2.1 shows the example of the weighting vectors for the parameters of the set (2.2) using a the synthetic spectrum with [Fe/H] $= -2.0$, T$_{\text{eff}} = 6000$ K, $\log g = 4.0$ and $A_s = 1$ as fiducial model (for details of the modelling of this spectrum see Sect. 3.3). The upper panel corresponds to the synthetic spectrum at the SDSS resolving power (R = 2000) and the panels B, C and D to the weighting vector for metallicity, effective temperature and surface gravity, respectively. This figure is a graphical representation of Eq. (2.5), and helps to better visualize the weight in relevant regions of the spectrum. The main absorption lines of the synthetic spectrum, which are also present in some of the weighting vectors, are listed in Table 2.1.

For metallicity (panel B), the major weight is concentrated in the two peaks at 3933 and 3969 Å, which correspond to the CaIIK and H lines, respectively, seen in the synthetic spectrum in panel A. The second important region in wavelength with considerable weights is close to 5180 Å, corresponding to the MgIb triplet. A minor peak is seen at the G-band of the CH molecule. These three features are metallic lines, therefore show a larger dependency on metallicity than the rest of the vector, which is dominated by a zero main weight.

For the temperature (panel C) the greatest weight is focused on the hydrogen Balmer lines at 4101, 4340 and 4861 Å. Peaks at the previous metallic lines are also seen, but with a minor amplitude. Finally, the surface gravity (panel D) presents the strongest dependence on the MgIb triplet. The wings of the CaII and Balmer lines also present small dependence. As in the case for metallicity, the rest of the continuum is weighted by a mean close to zero.

It is worthy to mention our statement that in the continuum the weight is not *equal* to zero, but with *zero mean*. This is because the synthetic spectrum of the fiducial model – even at the low SDSS resolution – shows weak metallic lines that are dependent on the parameters, which can be observed in the panel A of Fig. 2.1. These dependencies are negligible when compared with the strong absorption lines mentioned above. In addition, the dependencies at these wavelength regions divided by the noise of the observed spectrum yield a weight with zero mean.

The weighting is done by multiplying these vectors with the spectrum, where the information kept from the spectrum is given by the peaks of the weighting vector. This procedure is called *compression*, where the information about the parameter θ_j is expressed
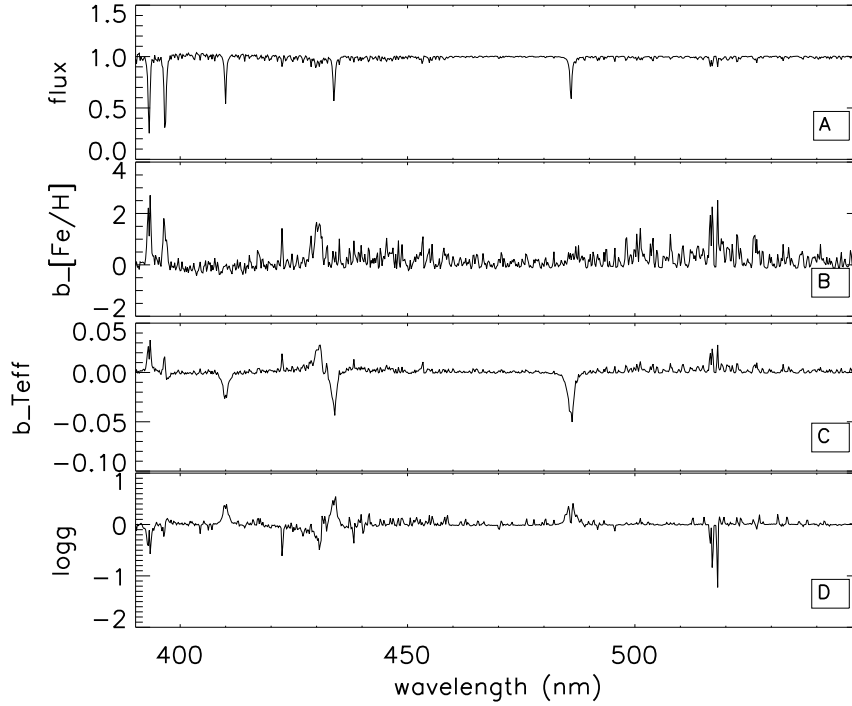
Figure 2.1: (A) Fiducial model with parameters [Fe/H] = −2.0, T_{eff} = 6000 K, $\log g$ = 4.0 and $A_s = 1$. Other panels indicate the weighting vectors according to Eq. (2.5) for metallicity (B), temperature (C) and surface gravity (D).

as

$$y_{j,\mathbf{X}} = \mathbf{b}_j \cdot \mathbf{X}, \qquad j = 1, 2, 3, 4 \tag{2.6}$$

with $\mathbf{X}$ being the spectrum. The weighting vector defined in Eq. (2.5) can compress data ($\mathbf{X}$) and model ($\mathbf{F}$) using Eq. (2.6). Since $\mathbf{b}_j$ and $\mathbf{X}$ (or $\mathbf{F}$) are $N-$dimensional, the product y_j in Eq. (2.6) is a number, which stores the information about the parameter θ_j.

In order to perform a compression for all the parameters simultaneously, y_k must be uncorrelated with y_j, with $j \neq k$. This means that the $\mathbf{b}$-vectors must be orthogonal, i.e. $\mathbf{b}_k \cdot \mathbf{b}_j = 0$. Following the procedure of Heavens et al. (2000) and as explained in Ben Panter's PhD thesis, the compressed data for the next parameter $y_k = \mathbf{b}_k \cdot \mathbf{X}$ (see Eq. 2.6) must be orthogonal and can be found with the standard Gram-Schmidt orthogonalization method

$$\mathbf{b_k} = \frac{1}{|\mathbf{b}_k|} \left[\frac{1}{\sigma^2} \frac{\partial \mathbf{F}}{\partial \theta_k} - \sum_{q=1}^{m-1} \left(\frac{\partial \mathbf{F}}{\partial \theta_k} \mathbf{b}_q \right) \mathbf{b}_q \right] . \tag{2.7}$$

For $m = 4$ the numbers $y_{1,\mathbf{X}}$, $y_{2,\mathbf{X}}$, $y_{3,\mathbf{X}}$, $y_{4,\mathbf{X}}$, represent the data and $y_{1,\mathbf{F}}, y_{2,\mathbf{F}}, y_{3,\mathbf{F}}, y_{4,\mathbf{F}}$ the models, corresponding to the information about the parameters of $\mathbf{\Theta}$ given in Eq. (2.2)
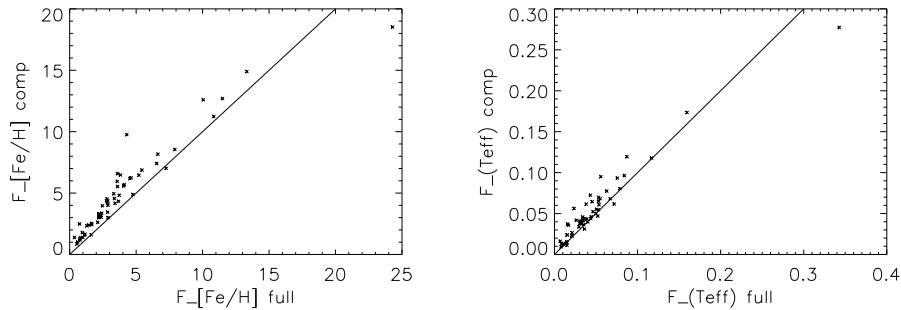
Figure 2.2: Correlations between the Fisher matrix values obtained from the full and compressed likelihoods for metallicity (left panel) and effective temperature (right panel) for 75 randomly selected stars of SDSS/SEGUE. The line correspond to the one-to-one relation.

2.3.3 Goodness of fit

Motivated by the Pearson's chi-square distribution introduced in Sect. 2.3.1, where the goodness-of-fit is given by the mean square difference between model and data, MAχ uses its own *compressed goodness-of-fit*, which is the square difference of the compressed data and compressed model:

$$\chi^2_{c,\theta_j} = \frac{1}{\sigma^2_{av}}(y_{j,\mathbf{X}} - y_{j,\mathbf{F}})^2, \tag{2.8}$$

and as in Sect. 2.3.1, this compressed goodness-of-fit gives the probability for the parameter θ_j.

$$L_{c,j}(\mathbf{X},\theta_j) = \frac{1}{(2\pi)^{N/2}\sqrt{\sigma^2_{av}}} \exp \frac{-\chi^2_{c,\theta_j}}{2} \tag{2.9}$$

Because the y_j numbers are by construction uncorrelated, the *compressed likelihood* of the parameters is obtained by multiplication of the likelihood of each single parameter $L_{c,j}(\mathbf{X},\theta_j)$

$$L_c(\mathbf{X},\mathbf{\Theta}) = \prod_{j=1}^{m} L_{c,j}(\mathbf{X},\theta_j) = \frac{1}{\left((2\pi)^{N/2}\sqrt{\sigma^2_{av}}\right)^m} \exp \frac{-\chi^2_c}{2}, \tag{2.10}$$

where

$$\chi^2_c = \frac{1}{\sigma^2_{av}}\sum_{j=0}^{m}(y_{j,\mathbf{X}} - y_{j,F})^2 \tag{2.11}$$

is the *compressed χ^2*.

As in the classical approach, the peak of the compressed likelihood estimates the parameters $\mathbf{\Theta}_0$ that generate the model $\mathbf{F}(\mathbf{\Theta}_0)$, which reproduces best the data $\mathbf{X}$. The advantage of using the compressed likelihood is that it is fast, because the calculation of χ^2_c needs only m iterations and not N as in the usual χ^2 computation. The search of the

maximum point in the likelihood is therefore done in a $m-$dimensional grid of $y-$numbers and not of $N-$length fluxes.

2.3.4 Retaining the information after the compression

The Fisher Information Matrix (Fisher 1935; Heavens 2009) describes the behavior of the likelihood close to the maximum. Here it is only used to show the lossless compression offered by the KL method, but a more extensive study is given in T97 and H00.

To understand how well the compressed data constrain a solution consider the behavior of the logarithm of the likelihood L near the peak. Here L denotes a generic likelihood that can correspond to the compressed one L_c or the full one L_f, since the procedure is the same. In the Taylor expansion the first derivatives $\partial(\ln L)/\partial\theta_j$ vanish at the peak and the behavior around it is dominated by the quadratic terms

$$\ln L = \ln L_{\text{peak}} + \frac{1}{2}\frac{\partial^2 \ln L}{\partial\theta_j\partial\theta_k}\Big|_{\text{peak}}\Delta\theta_j\Delta\theta_k, \tag{2.12}$$

The likelihood function can be approximated to a Gaussian near the peak and the second derivatives, which are the components of the inverse of the Fisher Matrix $\mathcal{F}_{jk}$, measure the curvature of the peak. Because the dependence of the parameters is not correlated, the matrix is diagonal with values

$$\mathcal{F}_{jj} = -\frac{\partial^2 \ln L}{\partial\theta_j^2}. \tag{2.13}$$

In Fig. 2.2 are plotted the values $\mathcal{F}_{[\text{Fe/H}]}$ and $\mathcal{F}_{\text{T}_{\text{eff}}}$, corresponding to the parameters of metallicity and effective temperature, respectively, for likelihoods of 75 randomly selected stars of SDSS/SEGUE, using the classical (full) and the compressed (comp) dataset. The line corresponds to a one-to-one relation. If the compressed and entire data sets behave similar next to the peak, it is expected that the values of the Fisher matrices agree. In Fig.2.2 it is possible to see how well the values correlate.

The same is expected to be found when both likelihoods are compared next to the maximum. Figure 2.3 shows full and compressed likelihood surfaces of metallicity and temperature for four randomly selected stars, where eight equally spaced contour levels have been plotted in each case. This is another way to visualize the statement that the Fisher Matrices correlate. The curvature of both likelihoods is the same close to the peak, as predicted. In Fig. 2.3 is also plotted the maximum point of the compressed likelihood as a triangle and the maximum point of the full one as a diamond. It can be seen that the maximum points of the compressed and full data set lie inside the first contour level of the likelihoods. This shows that the compressed data set gives the same solution as the full one - even after the dramatic compression.
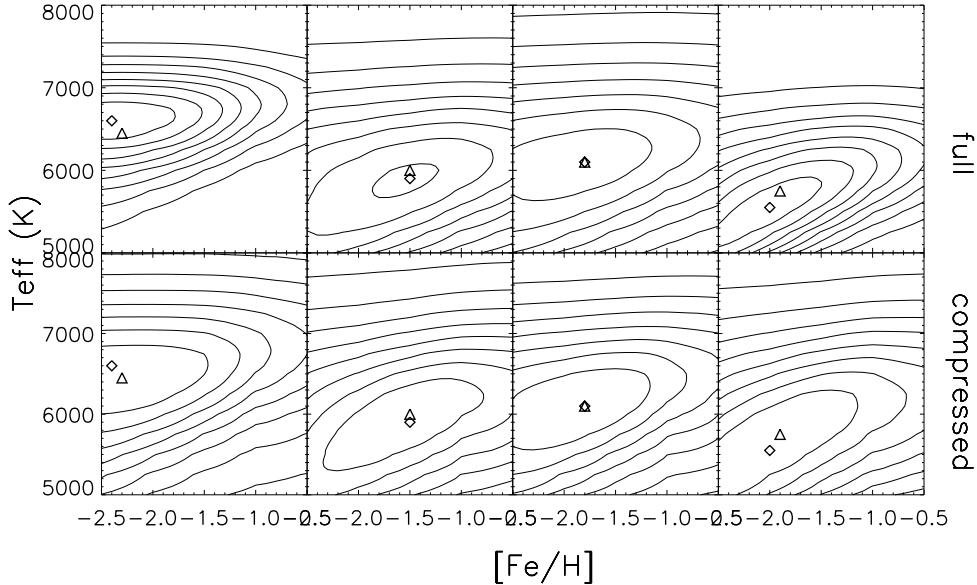
Figure 2.3: Likelihoods of the compress data set (upper panels) and full data set (lower panels) in the parameter space of effective temperature and metallicity for 4 randomly selected SDSS/SEGUE stars. In each panel 8 equally spaced contour levels are plotted. The triangle and diamond correspond to the maximum point of the compressed and the full data set, respectively. Both maxima lie in the first confidence contour level, meaning that both data sets reach the same solution for these two parameters.

2.4   MAχ Cookbook

This section is a description of the steps to follow for the fitting and parameter estimation. Here we focus on the general aspects that must be considered for performing a match between data and models, but for further details about the specific routines that build up the MAχ core, together with a schematic plot of MAχ, see Appendix A. We explain first separately the preparation that must be done for the spectra – real or synthetic – in Sect. 2.4.1, then we explain the steps to be done for the compression in Sect. 2.4.2 and Sect. 2.4.3 is a description of how we recover the parameters.

2.4.1   Configuration of spectra

Synthetic and real spectra: Continuum Subtraction

A stellar spectrum can be understood as a function that relates the bolometric flux of the star with its wavelength. This flux has two main components: a continuum and absorption lines. The continuum spectrum is known as the blackbody (e.g. Carroll & Ostlie 2006), which is the radiation of an *ideal emitter*. As a first rough approximation stars are blackbodies. However, the light coming from the photosphere of the star to us has to cross the atmosphere, which is not a blackbody, and photons will be absorbed by atoms

at specific wavelengths producing a lower intensity of the radiation at these wavelengths.

There are two ways to work with a stellar spectrum. One is to use the full spectrum, meaning to use the continuum and the lines, and the other one is to use the lines only, i.e. subtract the continuum. Unfortunately there is no rule of a best way to analyze the spectrum, meaning that each one has to decide what is most convenient way for his/her own particular purpose. Indeed, there are in the spectroscopic community critical discussions of how to proceed with a stellar spectrum because the quantities inferred (i.e. abundances, stellar parameters, etc) depend on the method employed in the analysis. It would be very welcome by the new young spectroscopists to have a complete documentation available about the methods, including their advantages and disadvantages.

In any case, the MAχ method compares synthetic spectra with observed spectra. In this case, both fluxes must be considered consequently, i.e. both with absolute fluxes or both with continuum subtracted. For an automatic fitting of an extensive sample of stars with a large grid of models, we decided to normalize the flux to a fitted continuum. In this way, we scale every spectrum to the same reference value (continuum at unity) and we focus the dependence of the parameters mainly on the line profiles. As discussed above, there are also many different methods to subtract the continuum, again with no rule of the best way of doing it. The final subtracted continuum can vary from method to method, therefore it is better to use the same method for data and model, although this is not always possible (see Chap. 4).

Due to noise of the spectra and the subtraction method uncertainties, the subtracted continuum will not be necessary at unity. This is the reason why MAχ has the 4th parameter A_s introduced in Eq. (2.2). The *scaling factor for normalization* basically multiplies the final flux by a factor such as 0.85, 1.1, etc. This scaling gives freedom to the fitting of the lines in case that the subtraction was too uncertain.

Synthetic spectra: Reproduce well the data

The resolution and wavelength range of the models must be according to the data; and the features modeled in the spectra must contain information about the parameters that want to be estimated. Finally, the physics involved in the models must be a good approximation of reality if the results want to be trustable.

Creating the grid of synthetic spectra has been one of the most difficult task that we have encountered during this thesis. The choice of line lists, wavelength range, continuum treatment, atomic and molecule data, interpolation of models, changes from star to star. In Chap. 3 and Chap. 4 we have created our own special grids of spectra, one for the analysis of low-resolution SDSS/SEGUE and other one for high-resolution UVES/VLT spectra. Both synthetic spectra are built differently because we were not able to reproduce both, SDSS/SEGUE and UVES/VLT spectra simultaneously. Detailed discussions and explanations of how we decided to create both grids can be found in Chap. 3 and Chap. 4. For the purpose of this chapter, where we explain how the MAχ method works, we refer to a generic grid of synthetic spectra.

Under the assumption that models reproduce well the data, each node of the grid

of models is represented as a synthetic spectral flux $\mathbf{F}(\mathbf{\Theta})$, which varies with different set of parameters. The set of parameters is represented by Eq. (2.2), meaning that the grid of models has 3 physical dimensions plus the scaling factor for normalization. It is certainly possible to include more dimensions in the grid, by modeling synthetic spectra with varying other parameters, such as single chemical abundances like [α/Fe], [C/Fe], etc, or microturbulence velocity.

Real Spectra: Move to laboratory frame

The data need to be corrected from the vacuum wavelength frame of the observations to the air wavelength frame of the laboratory. In addition, they need to be corrected for the Doppler effect zc due to the motions of the star, which in this case is done by using the flux minimum of the strong lines. It is possible to fit a gaussian to each strong line profile, where the mean of the gaussian corresponds to the flux minimum. The doppler shift given by this line is

$$zc = \frac{\lambda_o - \lambda_f}{\lambda_f} \tag{2.14}$$

where λ_o is the observed wavelength of the line profile, i.e. the mean of the gaussian, and λ_f is the wavelength flux minimum of this line in the frame of the laboratory. The final doppler shift is given by the averaged z_c of each line. To translate this effect into radial velocity, consider the formula:

$$v_r = c * z_c \tag{2.15}$$

where c is the speed of light in vacuum and v_r the radial velocity. Another widely used technique to measure the radial velocities is by cross-correlating the spectrum against a set of standard stars templates (Griffin 1967). While the cross-correlation can be time consuming (Yanny et al. 2009b), this appears to result in somewhat higher accuracy than the gaussian fit. Giving accurate radial velocities goes beyond the purpose of this thesis, therefore MAχ uses the gaussian fit technique to correct by Doppler effect. The test of the effect of the radial velocities in the final parameter estimation for SDSS/SEGUE stars is discussed with more detail in Chap. 3.

After this correction, the data have to be interpolated to the wavelength points of the models to get the same data points. The final step is to choose the spectral range for the analysis.

2.4.2   Compression procedure

For the compression of spectra it is necessary to choose a fiducial model $\mathbf{FM}(\Theta)$ to calculate the weighting vectors $\mathbf{b}_{[\mathrm{Fe/H}]}$, $\mathbf{b}_{\mathrm{T_{eff}}}$, $\mathbf{b}_{\log g}$ and $\mathbf{b}_{A_s}$, corresponding to metallicity, effective temperature, gravity and scaling factor for normalization, respectively. This model can be a random model taken from the grid of synthetic spectra. The systematic effects of different fiducial models in the final parameter estimation is discussed with detail in Sect. 3.6.1

The $\mathbf{b}-$vectors are employed then to calculate the set of $y-$numbers using Eq. (2.6) for each point in the grid of synthetic spectra obtaining a four dimensional $y-$grid, with

every point a single number. For the fitting, the respective $\mathbf{b}-$vectors are also employed to calculate the $y-$numbers for the observed spectra. Finally the compressed likelihood is computed with Eq. (2.11) for every point in the $y-$grid.

2.4.3   Parameter recovery

The minimum value in the $y-$grid corresponds to the maximum point of the compressed likelihood. It is important here to remark that the information of our interest is not this minimum value, but the *position* where this value is located. By tracing this position to the original grid, we know which synthetic spectrum is the responsible for the best fit.

Since the position of the compressed likelihood maximum lies in the 1σ confidence contour of the full likelihood, as seen in Fig. 2.3, to refine the solution we decided to switch at this point to the full data set, because the full χ^2 has a broad documentation (e.g Fisher 1935; Press 1993; Babu & Feigelson 1996), which facilitates the understanding of the parameters obtained. In addition, we are interested in getting a continuous parameter distribution, i.e. we want to obtain a temperature of 6462 K for instance, and not be restricted to have a value for the temperature of 6450 or 6500. The grid of synthetic spectra has discrete combinations of parameters, therefore we interpolate between the grid points. To calculate the classical *real* χ^2 we consider a quadratic interpolation using the grid points where the maximum is located and its two neighbor points for each parameter.

Another advantage to work with the full data set at this stage is the search for the 1σ errors, which correspond to the models within the confidence contour of $\chi^2 = \chi^2_{min} + \Delta\chi^2$ with $\Delta\chi^2 = 4.72$. This value comes from the 1σ contour in a likelihood with 4 free parameters, (for further details see chapter 14 of Press 1993). To find the *real* error – and not discrete values – we decided to perform this time a linear interpolation between the two grid points where the corresponding χ^2 is located. This requires the χ^2 value of only two grid points and therefore the calculation of the errors is less time consuming as if we would perform a quadratic interpolation like for the real χ^2 minimum.

2.5   Summary

This chapter described the **MA**ssive compression of χ^2 for stellar spectra (MAχ, Jofré et al. 2010), a method that allows estimates of stellar atmosphere parameters. This new tool was developed for the first time for this thesis, with the specific task to estimate effective temperature and metallicity of 140,000 stellar spectra from Sloan Digital Sky Survey.

We explained the need for the development of efficient ways to assess 140,000 stellar spectra, because the classical techniques, such as the maximum likelihood analysis, is too time consuming. The MAχ algorithm, which is based on the Karhunen-Loève eigenvalue problem, compresses the information stored in the stellar spectra to accelerate the evaluation of the likelihood.

This compression algorithm was explained, showing also how the information about the parameters is not lost after the compression. Since the KL method has been applied

for stellar spectra for the first time here, this chapter contains a cookbook explaining the steps to follow in the analysis.

Finally, Appendix A explains in detail the main routines that build up the MAχ core. Chapter 3 and Chap. 4 show examples for the application of the MAχ method to the estimation of stellar atmosphere parameters from SDSS and UVES/VLT, respectively. But the method can be applied for any kind of stellar spectra, making MAχ an attractive tool for the next generation of stellar surveys, such as Gaia (Perryman et al. 2001), SDSS-III (Rockosi et al. 2009), LAMOST (Zhao et al. 2006) and HERMES (Wylie-de Boer & Freeman 2010).

Chapter 3

MAχ for Low-Resolution Spectra

The largest sample of field stars currently available is provided by SDSS and SEGUE. It has more than 240,000 stellar spectra, from where atmosphere parameters can be determined. This survey is therefore attractive for studying stellar populations in a massive scale.

The MAχ method explained in Chap. 2 is an efficient method that assesses quickly and automatically stellar spectra and estimates atmosphere parameters. In this chapter we present the direct application of this method in SDSS spectra to estimate metallicities, effective temperatures and surface gravities of a sample of about 17,000 stars. We obtain accuracies of 0.24 dex for metallicity, 130K for effective temperature and 0.5 dex for surface gravity. Our results agree sufficiently well for our purpose, which is to determine the ages of main-sequence turn-off stars, with those obtained by the SSPP. This application shows that our method is a new and powerful tool for the next generation of large spectroscopic surveys.

3.1 Introduction

Our present view of the structure of the Milky Way is mainly built upon star counts. Spectroscopic surveys are extremely valuable to complement star count analyses and unravel coexisting stellar populations. Extensive surveys with high resolution have so far primarily been restricted to the solar neighborhood. Surveys of medium resolution have the advantage of being able to observe large number of distant stars, allowing thus to study the structure and formation of the different components of the Galaxy in large scale.

The Sloan Digital Sky Survey (SDSS, York et al. 2000) and its follow-up Sloan Extension for Galactic Understanding and Exploration (SEGUE, Yanny et al. 2009b) have revolutionized the knowledge of the Milky Way stellar contents. The more than 240,000 stars with multicolor photometry and spectroscopy allow to measure the properties of the thin and thick disk (Jurić et al. 2008) and to see a complex structure of the halo. There is an incredible amount of stellar streams detected with SDSS data (Belokurov et al. 2006; Yanny et al. 2009a), which prove the hierarchical scenario of galaxy formation (see e.g. Springel et al. 2006). Carollo et al. (2007) have used the kinematics of the stars to show that the halo has an inner and an outer component, which is an apparent result of a formation between a gravitational collapse proposed by Eggen et al. (1962) and the merging of small galaxies of Searle & Zinn (1978).

This rich amount of field stars with spectroscopy and photometry is still not completely exploited. In our attempt to determine ages for the turn-off SDSS stars we aim to contribute to the understanding of the formation and structure of the Milky Way halo. For this purpose we need to know the temperature and metallicity of a large sample of halo stars. By the time this thesis began, the SEGUE Stellar Parameter Pipeline (Lee et al. 2008a) was not available, so we had to process the spectra our selves to know these parameters. We developed MAχ as described in Chap. 2 for this specific purpose. Here we show the application of this method in a sample of about 17,000 stars, which was also recently published in Jofré et al. (2010).

We first explain the SDSS/SEGUE data in Sect. 3.2, then we describe the grid of models in Sect. 3.3 and we explain the specific match between this grid and SDSS spectra in Sect. 3.4. Different approaches to fit SDSS spectra are found in Sect. 3.5, where also a detailed comparison with the new SSPP is shown. Sect. 3.6 explains systematic errors of the method and finally a summary and conclusions of this chapter are given in Sect. 3.7.

3.2 Data: SDSS/SEGUE

The Sloan Digital Sky Survey (SDSS, York et al. 2000) has completed its Seventh Data Release (DR7, Abazajian et al. 2009). The survey uses a wide-field 2.5 m telescope (Gunn et al. 2006) located at the at the Apache Point Observatory in Southern New Mexico. The telescope has two instruments. The first one is a wide-field imager in the *ugriz* photometric system (Fukugita et al. 1996), where the limited magnitude of the images are at $u, g, r, i, z = 22.0, 22.2, 22.2, 21.3, 20.5$, respectively (Abazajian et al. 2004). The images

are processed through a series of pipelines that determine positions, brightnesses, shapes, etc of the objects. The photometric catalogs of the detected objects are used to identify objects for spectroscopy with the second of the instruments on the telescope. In the spectroscopic mode, up to 640 fibers can be simultaneously positioned, providing coverage from 3800 Å to 9200 Å, with a resolving power of $R \simeq 2000$.

Spectra have been acquired for one million galaxies and one hundred thousand quasars by SDSS. The major science program consists of constructing a large three-dimensional map of the Universe and constraining cosmological models. However, a significant product of the SDSS has been the large number of Milky Way stellar spectra combined with deep, accurate and multicolor photometry. Near the conclusion of the original SDSS program in 2004, partially as a result of the productive Galactic science enabled by SDSS, a set of three individual surveys were designed, under the designation of SDSS-II:

- Legacy, a survey following the same goals as the initial one

- SNIa: a survey for redshift type Ia supernovae

- Sloan Extension for Galactic Understanding and Exploration (SEGUE, Yanny et al. 2009b), which is the stellar survey of the Milky Way and its surrounding halo.

The data used in this work are a collection of stars detected by SDSS, Legacy and SEGUE. We first used photometry to select the sample from the SDSS database using the sqlLoader (Thakar et al. 2004). For the purpose of this chapter, which consists in showing the application of the MAχ method to a sample of F-G dwarfs, our constraints were that the objects must be a star and must have colors of $0.65 < u - g < 1.15$ and $0.05 < g - r < 0.55$. This color-cut photometrically selects the dwarfs of the stellar locus in color-color diagrams (see Sect. 5.4 for more details of color constraints using color-color diagrams). We verified the spectral type by also downloading the values 'seguetargetclass' and 'hammerstype', which classify our stars mainly as F-G dwarfs. We also constrained the metallicity to be in the range of $-999 < [Fe/H] < -0.5$, because for $[Fe/H] > -0.5$ the CaIIK line is saturated and does not serve as metallicity-indicator (see below). The latter values were taken from the new SEGUE Stellar Parameter Pipeline (Lee et al. 2008a,b; Allende Prieto et al. 2008b), were the -999 indicates that the pipeline has not estimated the metallicity of this particular star. Our final sample contains spectra of 17,274 stars with signal-to-noise above 10.

We choose metal-poor stars because we want to study the Galactic halo stars in further parts of this thesis. Metal-poor stars, in addition, do not have the problem of the saturation of metallic lines such as CaIIK (Beers et al. 1999), which is a very strong spectral feature that serves as a metallicity indicator in the low-resolution spectra from SDSS. Dwarf F-G halo stars near the turn-off fall in the temperature range where Balmer lines are sensitive to temperature and the spectral lines are not affected by molecules (Gray 1992). With these considerations it is correct to assume that the spectra will behave similar under changes of metallicity, temperature and gravity. This allows the choice of a random fiducial model from our grid of models for the creation of the weighting vectors, which will represent well the dependence of the parameters in all the stars.

3.3   Grid of models

The synthetic spectra were created with the synthesis code SPECTRUM (Gray & Corbally 1994), which uses the stellar atmosphere models of Kurucz (1992) and computes the emergent stellar spectrum under the assumption of local thermal equilibrium (LTE). The stellar atmosphere models assume the solar abundances of Grevesse & Sauval (1998) and a plane parallel line-blanketed model structure in one dimension. For the creation of the synthetic spectra, we set a the parameter of microturbulence velocity of 2 km/s, which is based on the atmosphere model value. Different microturbulence values do not affect significantly the shape of strong lines, which are used here for the analysis of low resolution spectra. The opposite is found in the analysis of high-resolution spectra, where a careful choice must be set to analyze weaker lines (see Chap. 4). The line list file and atomic data were taken directly from the SPECTRUM webpage[1]. In these files, the lines were taken from the NIST Atomic Spectra Database[2] and the Kurucz webside[3]. For these low resolution spectra, the line list used does not play a particular role in the final parameter estimation, because most of the weak lines contained in it will be hidden by the noise of the data. Strong lines, such as CaIIK, CaIIH and Balmer lines are produced in the computation of the SPECTRUM automatically and are not included in the line list. Our models try to reproduce old low-mass metal-poor turn-off stars, which have atmospheres without molecular lines. Therefore, no molecular opacity was considered in the model generation.

The creation of a grid of models is a difficult task, because the synthetic spectra have to agree with the observed one, which usually is not the case. On one side, the handling of the data concerning its noise and doppler effect introduce errors. On the other side, current LTE 1D stellar atmosphere models can be far away from reality (Collet et al. 2005; Asplund 2005). The creation of realistic models is difficult and computing-expensive, making the approximations of LTE 1D models still the best available for massive spectroscopic analyses. Creations of more realistic and sophisticated grid of models is one of the current hot topics in Galactic astronomy, especially for the analysis of the next generation of high resolution spectroscopic surveys.

We created an initial three dimensional grid of synthetic spectra starting from the ATLAS9 stellar atmosphere models (Castelli & Kurucz 2003) by varying the parameters Θ of Eq. (2.2). They cover a wavelength range from 3800 to 7000 $\mathring{A}$ in steps of $\Delta\lambda = 1\mathring{A}$, based on the wavelength range of SDSS spectra together with our line list. This wavelength range is broad enough for a proper continuum subtraction, as described in Sect. 3.4. The spectra have an absolute flux and were finally smoothed convolving a Gaussian line spread function to obtain a resolving power of $R = 2000$, according to SDSS resolution.

In order to have a finer grid of models, we linearly interpolated the fluxes created for the initial grid. It contains models with $-3.0 \leq$ [Fe/H] ≤ -0.5 with Δ[Fe/H] $= 0.1$ dex, $5000 \leq T_{\text{eff}} \leq 8000$ with $\Delta T_{\text{eff}} = 50$ K and $3.5 \leq \log g \leq 5$ with $\Delta \log g = 0.1$ dex. The scaling factor for the normalization varies linearly from 0.85 to 1.15 in steps

---

[1]http://www1.appstate.edu/dept/physics/spectrum/spectrum.html
[2]http://physics.nist.gov/PhysRefData/ASD/index.html
[3]http://kurucz.harvard.edu/linelists.html

of 0.01 (see below). The final grid has $21 \times 61 \times 16 \times 30 = 614,880$ models. In order to reproduce the abundance of α elements in the Milky Way, we set a linearly varying $[\alpha/\text{Fe}]$ of $[\alpha/\text{Fe}] = [0.2, 0.4]$ for stars in the metallicity range of $-0.5 \geq [\text{Fe/H}] \geq -1.0$ and $[\alpha/\text{Fe}] = 0.4$ for stars with $[\text{Fe/H}] \leq -1.0$, as in Lee et al. (2008a). The varying $[\alpha/\text{Fe}]$ abundances were also calculated with interpolation of fluxes created from solar and $\alpha-$enhanced ($[\alpha/\text{Fe}] = 0.4$) stellar atmosphere models.

We are aware that our metallicity [Fe/H] is estimated from lines of α elements (Ca, Mg). These elements scale different to iron for population II halo stars, where $[\alpha/\text{Fe}]$ = 0.4 for low metallicities as described above. In a ideal analysis, one should estimate metallicity from iron lines and the abundance of α elements from Ca and Mg lines. In our low resolution spectra, iron lines are usually hidden by the noise and we cannot separate the iron lines from those of α element ones. For that reason we prefer to base our grid of models assuming the values of the α abundances and scaling the iron abundance from the lines of α elements.

The grid discretization steps is smaller than the accuracies expected from the low resolution SDSS data. The extra time required to calculate the compressed likelihood (Eq. (2.10)) in this finer grid is not significant, and retaining the larger size of the grid allows us to demonstrate the suitability of the method for future more accurate data.

3.4   Matching models to data

We prepared data and models for the analysis as explained in Sect. 2.4. The correction for Doppler effect zc was done by using the flux minimum of the lines indicated in Table 2.1. The MgI triplet line is excluded, because it is not seen clearly enough in every spectrum, driving the automatic zc calculation to unrealistic values. A comparison of the radial velocity found with this method with the value given by the SEGUE database is shown in Fig. 3.1. The difference of the radial velocities (SEGUE - MAX) has a mean (offset) of -20.15 km/s with standard deviation (scatter) of 7.85 km/s. The effect of this difference on the final parameter estimation is discussed in Sect.3.5.

For automatic fitting of an extensive sample of stars with a large grid of models, we decided to normalize the flux of the observed spectra to a fitted continuum. In this way the dependence of the parameters is concentrated mainly on the line profiles. We adopted the normalization method of Allende Prieto et al. (2006), because it works well for the extended spectral range of SDSS spectra. It is based on an iteratively polynomial fitting of the pseudo-continuum, considering only the points that lie inside the range of 4σ above and 0.5σ below of the fitted pseudo-continuum. Then we divided the absolute flux by the final pseudo-continumm.

To compress the data we chose the fiducial model with parameters $[\text{Fe/H}] = -2.0$, $T_{\text{eff}} = 6000$ K, $\log g = 4.0$ and $A_s = 1$ and used it calculate the weighting vectors. The compression procedure and parameter recovery is done following the steps explained in Sect. 2.4.2 and Sect. 2.4.3, respectively.
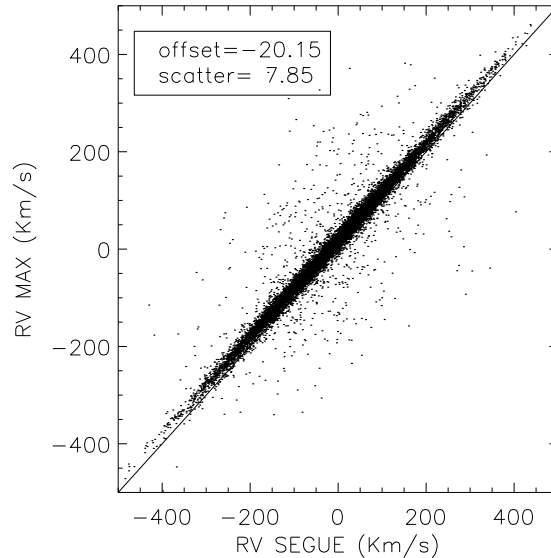
Figure 3.1: Radial velocities found using minimum fluxes of strong lines given by Table 2.1 (MAX) compared with those of the SEGUE database. The difference of the radial velocities given by the SEGUE database from those obtained by our method is indicated in the legend as "offset", with its standard deviation as "scatter".

3.5   Application to SDSS spectra

We chose to use the wavelength range of [3850,5200] Å, where we have information about metallicity, temperature and gravity, which is given by the absorption lines listed in Table 2.1. These spectral lines are strong in F-G stars, meaning they can be identified at low resolution without difficulty. The wings of Balmer lines are sensitive to temperature and the wings of strong Mg lines are sensitive to gravity (Fuhrmann 1998). Beacuse iron lines are not strong enough to be distinguished from the noise of othese low resolution spectra, the CaIIK and MgIb lines are our indicators of metallicity (Beers et al. 2000; Allende Prieto et al. 2006; Lee et al. 2008a).

It is important to discuss the carbon feature known as the G-band at 4304 Å in our spectral window. The relative number of carbon-enhanced metal-poor (CEMP) stars respect to the total number of stars at a given [Fe/H] value is expected to increase with decreasing metallicity (Beers et al. 1992) to about 20% at below [Fe/H] = −2.0 (Lucatello et al. 2006), possibly implying a strong carbon feature in the observed spectrum. As discussed by Marsteller et al. (2009), a strong G-band may also affect the measurement of the continuum at the CaII lines, which could result in an underestimation of the stellar metallicity. We commented in Sect. 2.3 on the influence of the lines in the weighting vectors used for the compression and we saw that the G-band also displays minor peaks (see Fig. 2.1). The role of this minor dependence compared with those from the CaII, Balmer and MgIb lines can be studied by comparing the final parameter estimation when using the whole spectral
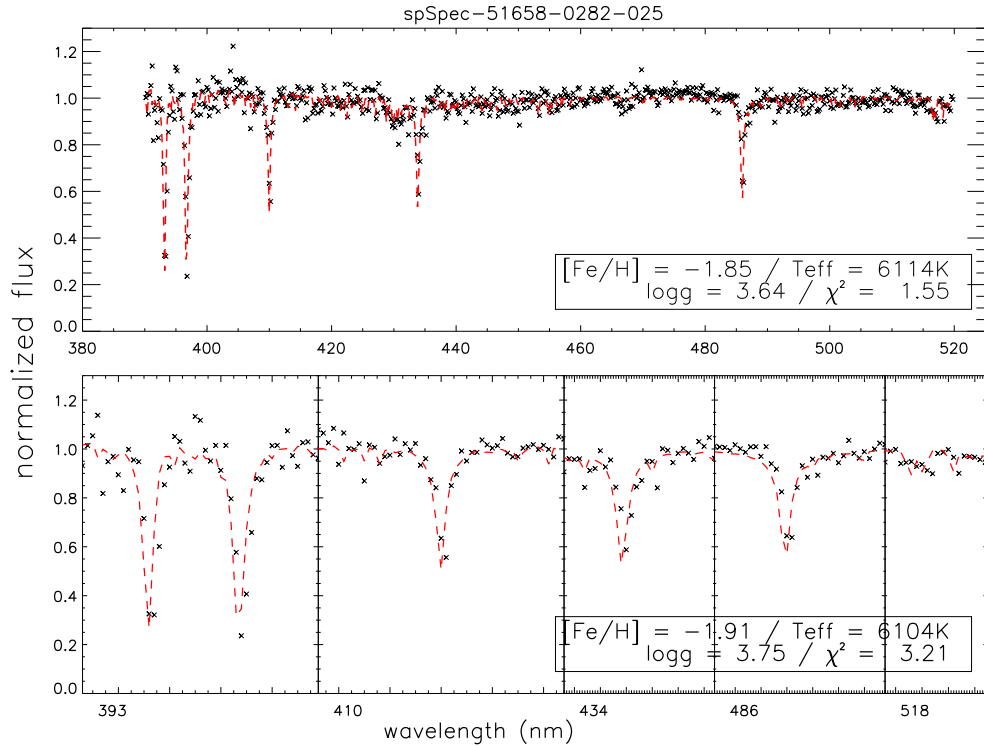
Figure 3.2: Example of the fit between the SEGUE star spSpec-51658-0282-025 (crosses) and a synthetic spectrum (red dashed line). The legend indicates the stellar atmosphere parameters of the model and the value of the reduced χ^2 of the fit. The upper panel is the fit using all the points of the spectral region [3850,5200] Å. The lower panel is the fit using only spectral windows given by the absorption lines of Table 2.1.

range or only those regions with the lines of Table 2.1, where the G-band is not considered. A further motivation for performing an analysis of an entire range against spectral windows is also explained below, where the implications of this tests in terms of fraction of CEMP stars are also discussed.

3.5.1   Whole wavelength domain vs. spectral windows

The classical χ^2 fitting procedure uses every datapoint; therefore, a straight-forward method to speed up the analysis would be to mask those parts of the spectrum which do not contain information about the parameters, essentially those that are merely continuum. Certainly, by considering only the CaII, Balmer and MgI lines, the number of operations becomes smaller, thus increasing the processing speed of χ^2 calculations. This is clumsy however: an empirical decision must be made about the relevance of pixels, and no extra weighting is considered - and the time taken for the parameters estimation is still long if one decides to do it for many spectra. The use of the **b**-vectors in the MAχ method means that very little weight is placed on pixels which do not significantly change with the parameter un-

der study, automatically removing the sectors without lines. The remarkable result of the MAχ method is that it is possible to determine the maximum of the compressed likelihood in 10 milliseconds with a present day standard desktop PC. This is at least 300 times faster than the same procedure when doing an efficient evaluation of the uncompressed data. The 1 σ confidence contours indicate errors in the parameters of 0.24 dex in metallicity on average, 130 K in temperature and 0.5 dex in gravity. Examples of fits are shown in Fig. 3.2. The upper plot shows the fit between a randomly selected SDSS spectrum and the best model, where the crosses correspond to the observed spectrum and the dashed red line to the model. The stellar atmosphere parameters are denoted in the legend, as well as the resulting reduced χ^2 of the fit. The plot in the bottom is the fit of the same star, but considering only the data points within the line regions identified in Table 2.1, as discussed above. Again, the red dashed line indicates the model with parameters in the legend, where the χ^2 of the fit is also given.

Because the lines contain the information about metallicity, temperature and gravity, we expect to obtain the same results whether we use all the data points or only those corresponding to the lines. The legends in Fig. 3.2 show the parameters estimated in both analyses. The small differences between them are within the 1 σ errors. We plotted in the upper panel of Fig. 3.3 the comparison for metallicity (left panel), temperature (middle) and gravity (right) of our sample of stars when using the whole spectral range ("whole") or only spectral windows with the lines ("win"). The offsets and scatters of the distribution as well as the one-to-one relation are indicated in the legend of each plot. Here we randomly selected 300 stars to plot in Fig. 3.3 to visualize better the correlations of the results. Offsets and scatters are calculated with the entire star sample. The metallicity has excellent agreements, with a small scatter of 0.094 dex, as shown in the legend of the plot. The temperature has a negligible offset of 38 K and a scatter of 69 K, which is also less than the accuracies obtained in the temperature estimation. The gravity has the largest scatter offset of 0.1 dex and a scatter of 0.34 dex, but this is still within the errors.

The negligible offsets obtained when using the entire spectral range against the limited regions is an encouraging result in terms of the effect of the G-Band on the spectrum. As pointed out above, the dependence on this feature in the parameters under study is not as strong as the rest of the lines of Table 2.1. This is translated into less weight for the compression, as seen in Fig. 2.1, meaning the G-band does not play a crucial role in our compressed data set for the parameter recovery.

Let us remark that this does not mean a lack of CEMP stars in our sample, we simply do not see them in the compressed space. A spectrum with a strong observed CH molecule gives a similar <u>compressed</u> χ^2 as one with a weak one, because the compression does not consider variations in carbon abundance. The <u>full</u> χ^2, on the other hand, will certainly be larger for the spectrum with a strong G-band, because our models do not have different carbon abundances. The fraction of CEMP stars is in any case high and it is certainly interesting to locate them with the MAχ method in the future. This implies that we would need to create another dimension in the grid of synthetic spectra – models with varying carbon abundances – and increase the number of parameters to analyze to five. One more dimension certainly means a heavier grid of models, but in terms of parameter
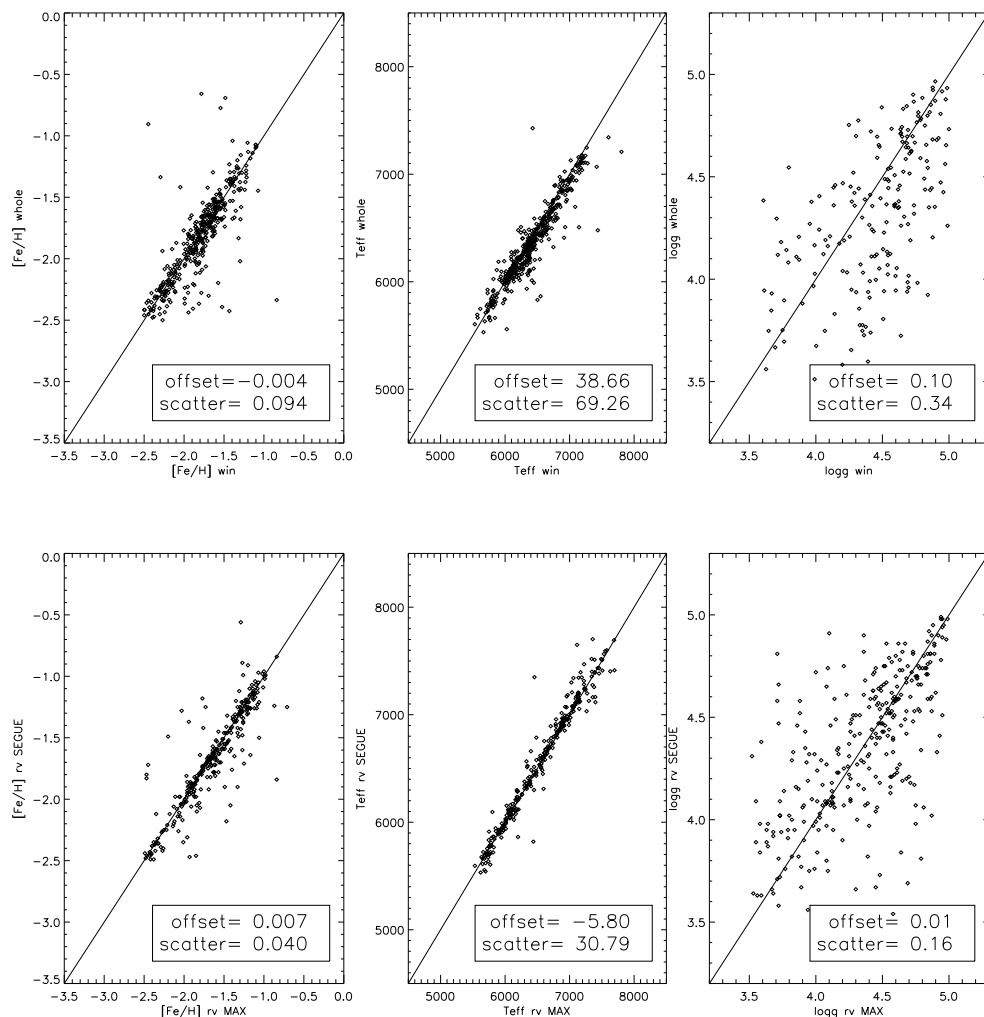
Figure 3.3: Upper panel: Metallicity (left), effective temperature (middle) and surface gravity (right) obtained using MAχ for the entire spectral range of [3900, 5200] $\mathring{A}$ (whole) compared to that with the selected spectral windows given by the absorption lines of Table 2.1 (win) for a sample of 300 randomly selected stars. The offset (mean difference of "win - whole") of the results and its scatter (standard deviation) is indicated at the bottom right of each plot. The line has a slope of unity. Lower panel: as upper panel, but investigating the influence of using our radial velocities (rv MAX) or the SEGUE ones (rv SEGUE). Offset and scatters are calculated from the difference "SEGUE-MAX".

recovery, there is no big difference to use four or five $y-$numbers for the compressed χ^2 calculation. This study goes beyond the scope of this chapter, where we are only interested in the estimation of the three basic atmosphere parameters using the MAχ method.

3.5.2 Effect of radial velocity uncertainties

As mentioned in Sect. 2.4 and seen in Fig. 3.1, radial velocities given by the SEGUE database have a mean difference of 20 km/s compared to ours. To study the effect of this difference in the final parameter estimation, we analyzed a subsample of randomly selected 2,500 stars using SEGUE radial velocities. The comparison of the metallicity, effective temperature and surface gravity obtained when using our radial velocities ("rv MAX") and the SEGUE ones ("rv SEGUE") can be seen in the lower panel of Fig. 3.3. In this plot a small sample of randomly selected 300 stars was used to better visualize the results. The offsets and scatters were calculated considering the 2,500 stars. A difference in 20 km/s produces offsets and scatters in the three parameters, with 0.007 ± 0.040 dex for metallicity, -5.08 ± 30.79 K for temperature and 0.01 ± 0.16 dex for gravity. These offsets and scatter are negligible when compared with the 1σ errors obtained for the parameter estimation, as can be seen in the legend of Fig. 3.1.

Table 3.1: Offsets (Δ) and scatter (σ) of the differences (raw - column) between the methods: MAχ (this work). ADOP (Lee et al. 2008a), NGS1 (Lee et al. 2008a), ANNSR (Re Fiorentin et al. 2007) and k24 (Allende Prieto et al. 2006) for the entire sample of selected SEGUE stars.

	ADOP Δ/σ	NGS1 Δ/σ	ANNSR Δ/σ	k24 Δ/σ
[Fe/H]				
MAχ	-0.32 / 0.23	-0.41 / 0.29	-0.17 / 0.33	-0.34 / 0.26
k24	0.04 / 0.14	-0.07 / 0.25	0.17 / 0.27	
ANNSR	-0.13 / 0.22	-0.22 / 0.23		
NGS1	0.08 / 0.17			
T$_{\mathrm{eff}}$				
MAχ	-61 / 112	80 / 132	-76 / 170	-159 / 160
k24	98 / 101	244 / 166	88 / 195	
ANNSR	1 / 114	147 / 173		
NGS1	-142 / 93			
$\log g$				
MAχ	0.51 / 0.39	0.38 / 0.43	0.63 / 0.47	0.41 / 0.48
k24	0.08 / 0.35	-0.02 / 0.42	0.26 / 0.48	
ANNSR	-0.14 / 0.36	-0.27 / 0.45		
NGS1	0.09 / 0.23			

3.5.3 Comparison with the SEGUE Stellar Parameter Pipeline

The SEGUE Stellar Parameter Pipeline (SSPP, Lee et al. 2008a,b; Allende Prieto et al. 2008b) is a combination of different techniques to estimate the stellar parameters of SEGUE. Some of these techniques are to fit the data to a grid of synthetic spectra like the k24 (Allende Prieto et al. 2006), and the k13, NGS1 and NGS2 ones (Lee et al. 2008a). Another method are the ANNSR and ANNRR of Re Fiorentin et al. (2007), which are an artificial neural network (ANN) trained to use a grid of synthetic (S) or real (R) spectra to estimate the parameters of real spectra (R). Other options are absorption CaIIK indices (Wilhelm et al. 1999; Beers et al. 1999).
We compared our results with the final adopted SSPP value (ADOP), and those of the k24, NGS1 and ANNSR grids of synthetic spectra. Each of these results can be found in the tables of the SDSS database. The grids of models are created using Kurucz stellar atmosphere models, but k24 and NGS1 cover the wavelength range of [4400,5500] Å. The ANNSR grid includes the CaII triplet close to 8600 Å.

Figure 3.4 shows the correlations between the results of these methods and our own. As in Fig. 3.3, we plotted a random selection of 150 stars to better visualize the correlations, but values of offsets and scatters were made using the entire sample of 17,274 stars. The left panels correspond to the metallicity, the middle ones to temperature and the right ones to the surface gravity. The top row of plots shows a general comparison of all the different methods, plotted with different colors. The $y-$axis indicates the ADOP results and the $x-$axis the methods MAχ (black), NGS1 (blue), ANNSR (red) and k24 (green). For each distribution a histogram of (method$_i$ − method$_j$) with $i \neq j$ was fitted with a Gaussian to obtain estimations for offset (mean Δ) and scatter (standard deviation σ). The results are summarized in Table 3.1. In the lower panel of Fig. 3.4 we plotted the comparisons of individual methods for 150 randomly selected stars. These panels help to better visualize how the single methods of the pipeline and our own correlate with each other. Figure 3.4 and Table 3.1 show that our results reasonably agree with the pipeline, and that the scatter is of the same order on magnitude as that between the individual SSPP methods.

Considering individual parameters, our metallicities have a general tendency to be ~ 0.3 dex lower than adopted metallicity of SSPP (ADOP). A similarly large offset exists between ANNSR and NGS1, with -0.22 dex. This could be due to the consideration of the CaII lines in the fit, which are not included in the NGS1 and k24 ones. ANNSR also includes CaII lines, the offset of -0.17 dex to our results is smaller than the 1 σ error. If the same lines are used in the fitting, no offset should be seen, as will be shown in Sect. 4.5.

It is interesting to mention recent papers of the SEGUE collaboration (Carollo et al. 2010; Smolinski et al. 2010), where they comment that SSPP is actually conservative in the assignment of metallicities of lower [Fe/H]. Their high-resolution estimates of [Fe/H] actually are of the order of 0.2 - 0.3 dex lower than those reported by the SSPP. Indeed, this was the major subject discussions during the last SDSS collaboration meeting in Paris 2010. In Fig. 3.4 we see that at low metallicities our estimates of [Fe/H] deviate the most with respect to the ADOP ones. It is interesting to realize that the SSPP is not giving the "final absolute number" of metal-poor stars contained in the SDSS database.
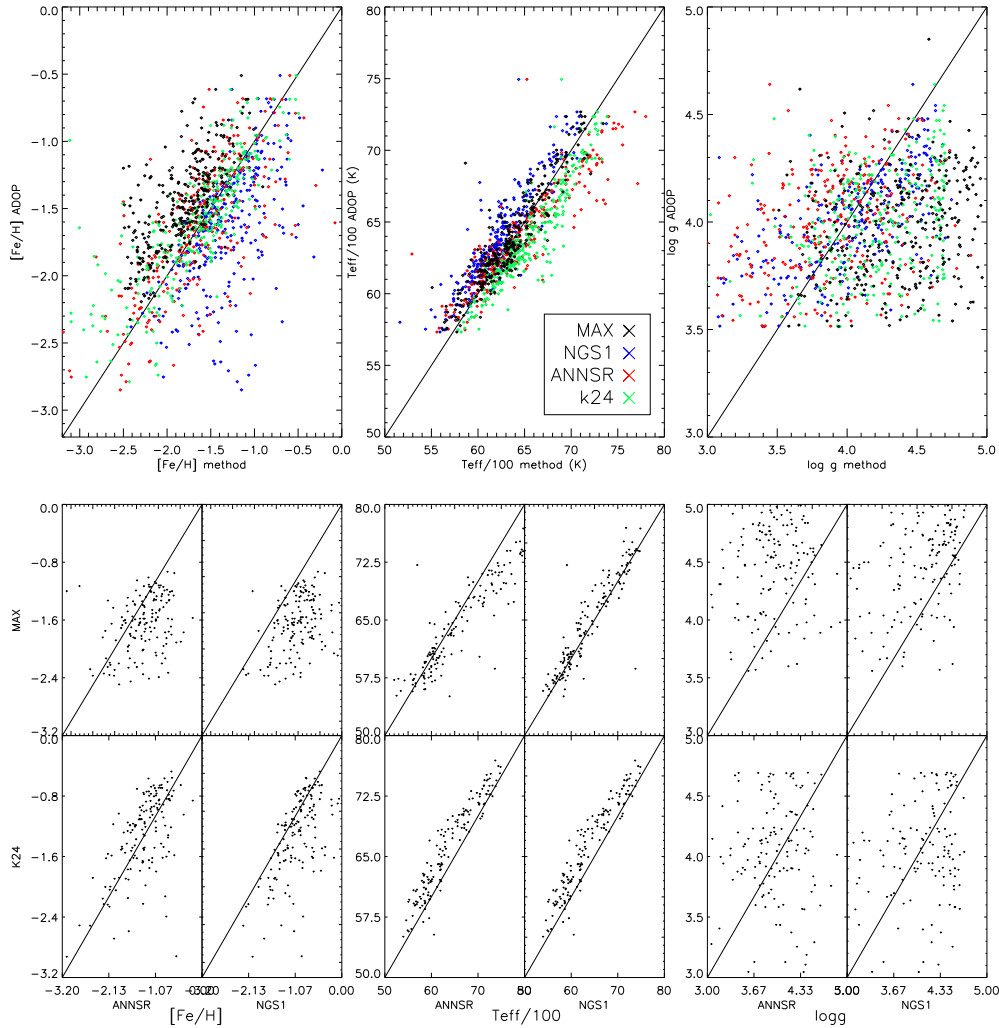
Figure 3.4: Upper plot: Comparison of the results from the SEGUE Stellar Parameter Pipeline (SSPP) with different methods: This work (MAX, black), (Lee et al. 2008a, NGS1, blue), (Re Fiorentin et al. 2007, ANNSR, red) and (Allende Prieto et al. 2006, k24, green). Lower part: Comparisons of individual methods for a randomly selected subsample of stars. Each plot has a line with slope of unity. The different offsets and scatters between the results are indicated in Table 3.1. In each plot, a selection of 150 random stars has been used.

Given the current activity in calibrations of the pipeline, we think that it is very useful to have independent results. We will see in the next chapters how important is to have independent estimates of parameters, because they are useful when comparing results of more fundamental questions, such as the age of the Galactic halo.

The temperature, on the other hand, shows a small offset of -61 K with respect to the

ADOP value of the pipeline. It is encouraging to see that we obtain the best agreement, except for ANNSR, which has no offset. A large mean difference is found between k24 and NGS1, where the offset is 244 K. The scatter in the various comparisons varies from 100 K (NGS1 v/s ADOP) to 200K (k24 v/s ANNSR); our scatter of 112 K with respect to ADOP is one of the lowest values.

Finally, $\log g$ shows the largest offset. We derived gravity values 0.51 dex higher than the ADOP ones. The worst case is the comparison between our method and ANNSR with 0.63 dex. Between the methods of the pipeline, the largest difference (0.27 dex) is found between ANNSR and NGS1. The best agreement we found for gravities are with NGS1, with an offset of 0.38 dex. The scatter for gravities varies from 0.23 dex (NGS1 v/s ADOP) to 0.48 dex (ANNSR v/s k24 and MAχ v/s k24). A possible approach to correct our gravities would be to shift the zero point by -0.38 dex to agree with those of NGS1. We prefer to accept that gravity is our least constrained parameter, given the lack of sensitive features except for the wings of the MgIb lines, and the noise in the spectra does not restrict $\log g$ effectively. In order to deal with this problem, k24 and NGS1 smooth the spectra to half of the resolution, gaining a better signal-to-noise by this procedure. We remark that the k24 grid includes $(g - r)$ colors to constrain the temperature. This automatically leads to different gravity values. A more extensive discussion of this aspect will be given in Sect. 4.5.2. The right panels of Fig. 3.4 shows that all $\log g$ estimates are rather uncorrelated with each other with respect to the other ones.

3.6   Systematic effects

When developing any method, it is important to find systematic effects because they tell us the power and limitation of othe method. In this section we discuss two important sources of systematic effects related with MAχ. The first one is connected to the fiducial models used to build the $\mathbf{b}-$vectors and the second one is connected to the construction of the grid of synthetic spectra.

3.6.1   Choice of fiducial model

The $\mathbf{b}-$vectors are derivatives with respect to the parameters. With the assumption that the responses of the model to these derivatives are constant, the choice of the fiducial model (FM) used to build the $\mathbf{b}-$vectors is free. This assumption, however, is only correct for certain regions of the parameter space. For example, Balmer lines are good temperature indicators for stars not hotter than 8000K (Gray 1992), and for cold stars spectral lines are affected by molecular lines. Limiting our candidate stars to the range of 5000K to 8000K we know that we have a clean spectra with Balmer lines as effective temperature indicators. This allows to choose a FM with any temperature in that range to construct our weighting vector $\mathbf{b}_{\mathrm{Teff}}$, which will represent well the dependence of the model spectrum on temperature. Similar assumptions are made for the other two model parameters.
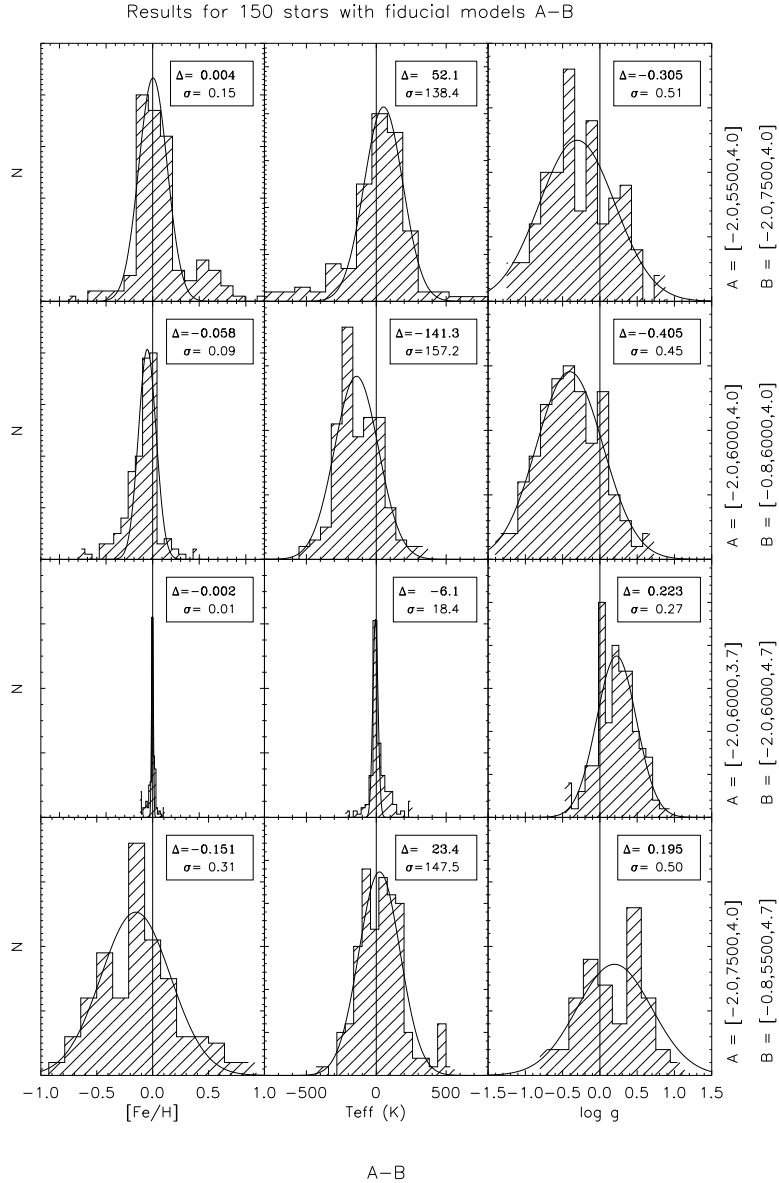
Figure 3.5: Histograms of the differences of the results of 150 test stars obtained using 8 different fiducial models for the compression. Left: metallicity, middle: temperature and right: gravity. The parameters of the fiducial model are indicated in the right side of each plot, labeled as [[Fe/H], T_{eff}, $\log g$]. Each histogram has a Gaussian fit, where the peak (Δ) and the standard deviation (σ) are indicated in the top legend. From top to bottom we have varied T_{eff}, [Fe/H], $\log g$ and all parameters.

In order to test this assumption we studied the effect of employing different fiducial models in the final results of the parameter estimation. In Fig. 3.5 we plot the results of metallicity (left), temperature (middle) and gravity (right) for 150 randomly selected SDSS/SEGUE stars. We have considered two different sets of fiducial models, labeled as A and B, and we have analyzed the distribution of the difference in the results obtained between the FM of the set A and the set B, respectively. This was done for four sets of different fiducial models [A,B]. The parameters of the FM are indicated at the right side in each comparison panel. From top to bottom the first one compares the results of a cold ($T_{eff} = 5500$ K) and a hot ($T_{eff} = 7500$ K) fiducial model of our grid of synthetic spectra, the second one a metal-poor ([Fe/H] = −2.0) and a metal-rich ([Fe/H] = −0.8) one. The third one considers two different gravities ($\log g = 3.7$ and $\log g = 4.7$). For these three sets, all other parameters are identically calculated. Finally, the last one uses models which vary all three parameters. The histograms of each plot correspond to the difference of the results obtained with the fiducial model with a set of the parameters A and B, respectively. The Gaussian fit of the histogram is overplotted and its mean (Δ) and standard deviation (σ) are indicated in the legend at the top.

Metallicity shows a well defined behavior under different **b**-vectors. There are negligible offsets when varying only one parameter in the FM, except for the case where the FM is totally different. But even in that case the offset of -0.15 dex is less than the 1 σ errors of 0.25 dex obtained in the metallicity estimation. We conclude that this parameter does not show real systematic offsets due to the choice of fiducial model. The scatter obtained in the metallicity is also less than the 1 σ errors of the results. Only in the last case (bottom left) it becomes comparable with the errors. Because gravity is a poorly constrained parameter (see discussions above) and the $y-$numbers are uncorrelated, the effect when using different gravities in the FM should be completely negligible in the result of the other parameters. This can be seen in the third panel from top to bottom of Fig. 3.5, where metallicity and temperature show extremely small offsets and scatters. The derivation of temperature using different fiducial models shows a similar behavior. The discrepancies between results when using different FM are on the order of 50 K, except when the metallicity is varied. The mean difference of the final temperature estimates when using a metal-poor fiducial model and a metal-rich one is of 141 K, which is smaller than some differences seen in Table 3.1 between the methods of the SEGUE Stellar Parameter Pipeline. This probably happens because the spectrum of a metal-rich star presents more lines than a metal-poor one, which is translated into the **b**-vector as temperature-dependent regions that do not exist. In the case of SDSS data, many of the weak lines seen in a metal-rich synthetic spectrum and(or) the **b**-vector of a metal-rich fiducial model are hidden by the noise in the observed spectra and the assumption of a temperature dependence due to these weak lines may not be correct. For the analysis of low signal-to-noise spectra, it is preferable to choose a FM with a rather low metallicity. But even when using a high metallicity for the FM, the offset is comparable with the 1 σ error of 150 K for the temperature estimations. We conclude that temperature does not show a significant systematic offset due to choice of fiducial model either.

Finally, gravity shows larger discrepancies in the final results when varying the FM. The differences can be as large as 0.4 dex in the worst case when using different metallicities in the FM. This could also be because a metal-rich FM contains more lines and therefore greater sensitivities to gravity, which in our low signal-to-noise spectra is not the case. These sensitivities are confused with the noise in the observed spectrum. Scatters of 0.5 dex are in general on the order of the 1σ errors.
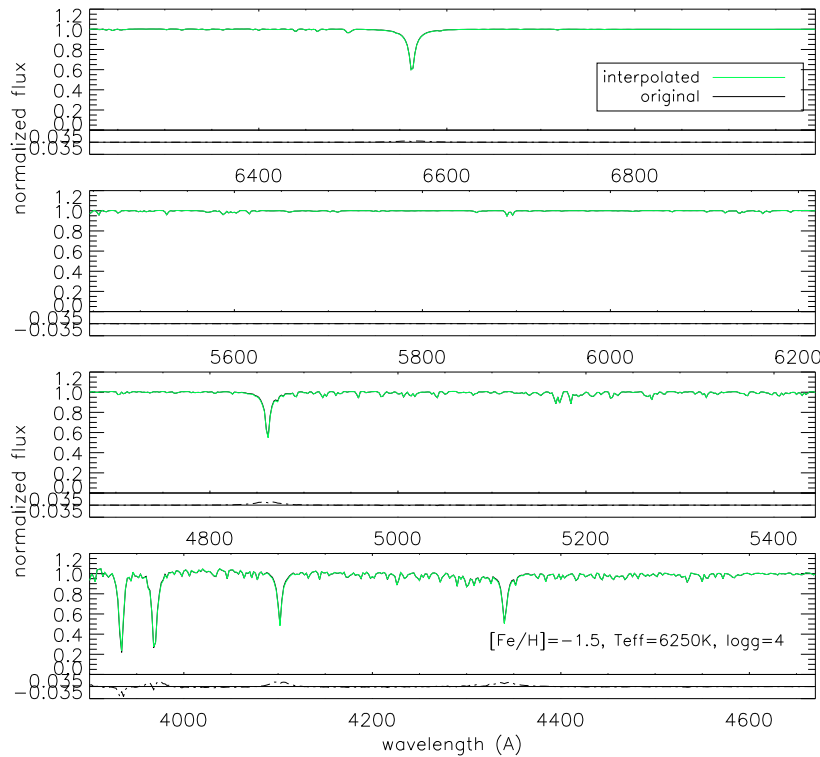
Figure 3.6: Comparison between a synthetic spectrum created directly from the model atmosphere (black line) and that resulting from a linear interpolation between two synthetic spectra (green). Dashed line at the bottom of each panel represents the difference of both spectra along with the zero point.

3.6.2   Choice of grid of models

By the time that the MAχ code was developed and its first application to SDSS was published (Jofré et al. 2010), we acquired experience with modeling atmospheres. The new version of the ATLAS code for modeling atmospheres, (ATLAS12 Kurucz 2005; Castelli 2005; Sbordone 2005) is able to create atmosphere models with different chemical compositions and opacity sampling. The creation of these new atmosphere models helped us to find an important systematic effect in our method. In this section we present it, where we

show the differences obtained in two parameter distributions. The first one was obtained using our old grid of synthetic spectra created from ATLAS9 as described in Sect. 3.3. The second one was obtained from a grid created using ATLAS12 atmosphere models. In both cases, the the parameter recovery was done as explained above.

ATLAS9 grid

At first approximation, at SDSS resolution we can interpolate linearly the flux at a certain wavelength between two synthetic spectra and like this create a finer grid. As an example, we consider a typical metal-poor halo turn-off star as it would be observed with SDSS. Its synthetic spectrum is illustrated in Fig. 3.6. The black line corresponds to an original spectrum with ([Fe/H]=-1.5, T_{eff}= 6250 K, $\log g$= 4). The green spectrum is the result of a linear interpolation between a spectrum with ([Fe/H]=-1.5, T_{eff}= 6000 K, $\log g$= 4) and a spectrum with ([Fe/H]=-1.5, T_{eff}= 6500 K, $\log g$= 4). At the bottom of each panel we can see how the difference between both spectra is very close to zero. A linear interpolation between two spectra with 500 K of difference in temperature results in a spectrum that looks almost identical to an original one, with the total of the square differences, normalized by the number of data points (1550) of $\delta = 5.15 \times 10^{-6}$. We concluded that a linear interpolation around 250 K results in a good approximation of the spectra and we created an interpolated grid with step-sizes of 50 K from the full calculated grid based on the ATLAS9 grid of atmosphere models of Castelli & Kurucz (2003), as explained in Sect. 3.3.

We found that the final parameter distribution can be, however, strongly affected. This is observed in the upper panels of Fig. 3.7 for the metallicity and temperature distributions of a sample of 4,952 randomly selected stars from the *TO poor* SDSS sample (see Table 5.1). In the distributions we can see that there are gaps near to the regions of [Fe/H]= $(-2, -1.5, -1)$ and T_{eff}= $(6000, 6250, 6500)$ K. These regions correspond to the grid points where the original synthetic spectra were created from the ATLAS9 grid of atmosphere models. These spectra were then used for the linear interpolation.

The reason is that in the calculation of the **b**−vectors we are assuming that the parameters change smoothly over the parameter space. A linear interpolation is not smooth at all, is only a first order approximation. This is the reason why the parameters do not show a continuous and smooth distribution. To improve this situation, we could have increased the order of the interpolation, but that would still mean to approximate the real behavior of the parameters. We decided to create a new grid of models avoiding interpolations.

ATLAS12 grid

In order to create an atmosphere model, ATLAS12 needs a starting model, which is used for convergency. The starting models were those of the ATLAS9 grid (Castelli & Kurucz 2003), and for each new model we looked for the closest one in the old grid. We computed then a grid of atmosphere models using the ATLAS12 version as described in Sbordone (2005) and Castelli (2005). The parameter space is of $-3.0 \leq [Fe/H] \leq -0.5$ with $\Delta[Fe/H] = 0.1$ dex, $5000 \leq T_{eff} \leq 7000$ with $\Delta T_{eff} = 50$ K and $3.5 \leq \log g \leq 5$ with $\Delta \log g = 0.5$. We

decided to have larger step sizes in $\log g$ for this grid than for the older one of Sect. 3.3, because we were not able to constrain properly the gravity parameter. Moreover, for the purpose of this work, we can avoid this parameter and still investigate ages for the turn-off halo stars. Based upon this grid of atmosphere models we created the synthetic spectra using SPECTRUM as described in Sect. 3.3.

Although the internal structure between ATLAS9 and ATLAS12 models can be different (Castelli 2005), the final synthesis at this resolution is not significantly affected. Figure 3.8 compares synthetic spectra created with both atmosphere models. In the left panel we have plotted spectra with ([Fe/H]=-1.5, T_{eff}= 6250 K, $\log g$= 4) obtained originally with an ATLAS9 atmosphere model (black line) and one obtained with an ATLAS12 atmosphere model (green line). Both spectra look almost identical, with $\delta = 2.06 \times 10^{-5}$. At the right panels we have plotted spectra with ([Fe/H]=-1.7, T_{eff}= 6350 K, $\log g$= 4). The black line corresponds to the result of a linear interpolations between the spectra with ([Fe/H]=-1.5, T_{eff}= 6250 K, $\log g$= 4), ([Fe/H]=-2.0, T_{eff}= 6250 K, $\log g$= 4), ([Fe/H]=-1.5., T_{eff}= 6500 K, $\log g$= 4) and ([Fe/H]=-2.0, T_{eff}= 6500 K, $\log g$= 4), which were created from the respective ATLAS9 models. The resulting spectrum is displayed in Fig. 3.8 with black and is compared with one constructed directly from an ATLAS12 model, which is plotted with the green line. It is possible to see that these spectra also agree well, with $\delta = 4.35 \times 10^{-6}$. Dashed lines at the bottom of each panel represent the absolute difference of both spectra, which is very close to zero. This implies that the results in the parameter recovery should
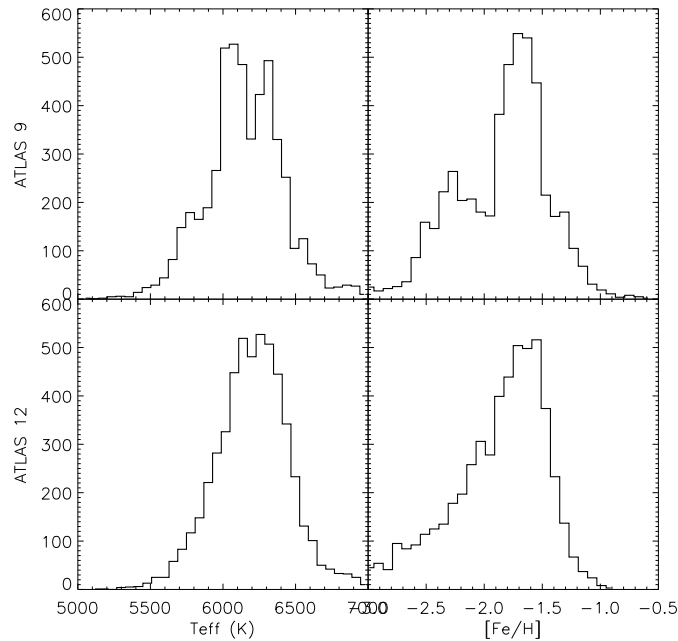
Figure 3.7: Upper panel: Metallicity and temperature distribution from the ATLAS9 interpolated grid. Lower panel: Metallicity and temperature distribution for the new ATLAS12 grid.

not change abruptly when we use a grid of models created with ATLAS9 or ATLAS12 because both synthetic spectra have similar shapes.
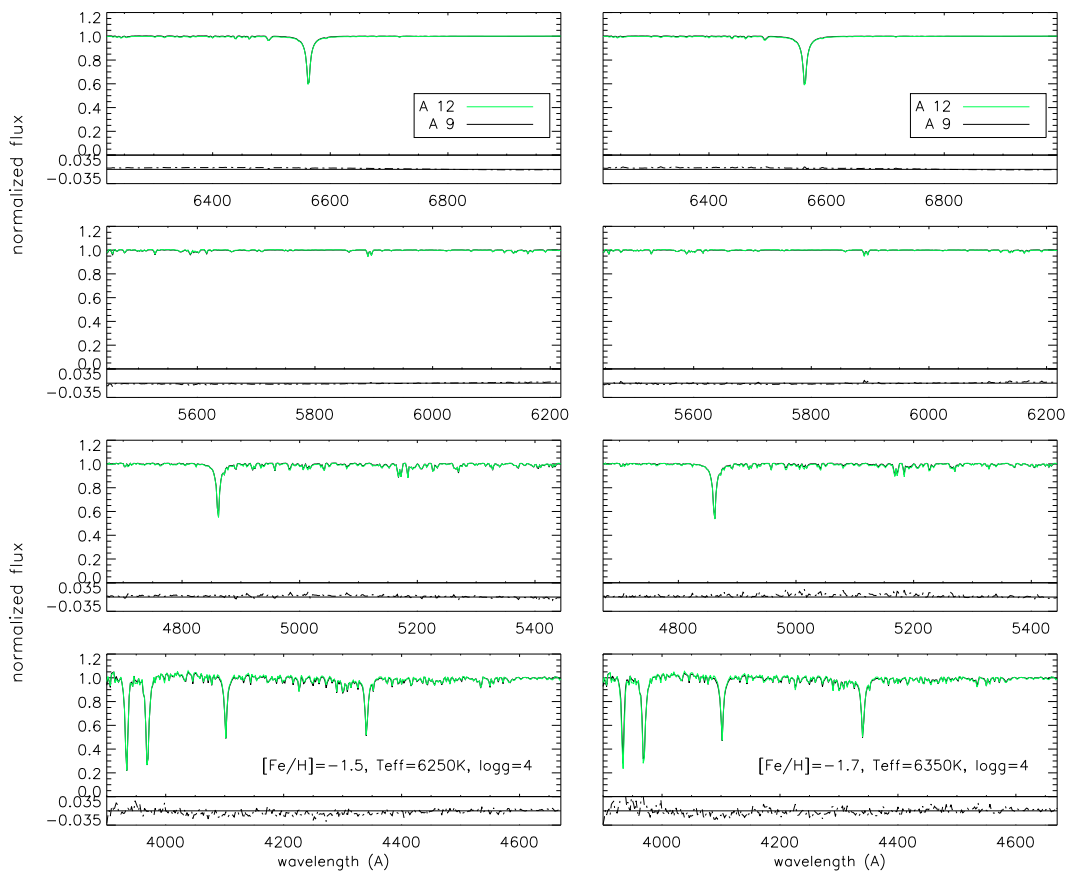
Figure 3.8: Example of synthetic spectra created from ATLAS 9 (black) and ATLAS 12 (green) atmosphere models. Left panels: Comparison between two synthetic spectra created directly from the atmosphere model. Right panels: Comparison between a synthetic spectrum created directly from an ATLAS12 model and one created from linear interpolations between spectra created from ATLAS9 models. Parameters of the spectra are indicated at the bottom. Dashed line at the bottom of each panel represents the difference of both spectra along with the zero point.

Discussion

The comparison of the metallicity and temperature distribution obtained using the new grid of spectra can be found in the lower panel of Fig. 3.7. We can see now how the distributions is now continuous. This is because now it is correct to assume that the parameters have a

smooth behavior over the parameter space, meaning that the **b**−vectors are representing better the dependencies of the parameters without approximations.

Another feature worth notting from Fig. 3.7 is that the temperature and metallicity distributions become continuous with ATLAS12. Note that the peak of the distributions remain at the same value. For the ATLAS9 grid, the metallicity distribution has its peak at [Fe/H]= -1.72 and a scatter of 0.34 dex, while for the ATLAS12 grid we found the peak at [Fe/H]= -1.71 with a scatter of 0.31 dex. For the temperature we observe a similar effect, where the ATLAS9 distribution has its peak located at 6180 K and has a scatter of 240 K while the ATLAS12 distribution has its peak at 6230 K and a scatter of 230 K. Considering the errors obtained in the parameter recovery, these differences are negligible.

We recall to the reader that the tests explained in this Chapter and in Jofré et al. (2010) were done using the old grid of synthetic spectra computed based on ATLAS9 models and interpolating the fluxes. We saw that the distribution of the parameters obtained with this grid is not as continuous as the distribution of the new grid, but we also could demonstrate that the peak of the distributions remain and that the values agree within the errors. This implies that the comparisons respect with the SSPP pipeline will not change with the new grid of models. Since the the new grid of models avoids interpolations and the parameters obtained from it distribute more continuous, we decided to use these parameters for the following part of this work.

3.7 Summary and conclusions

The extremely fast multiple parameter estimate make the MAχ method a powerful tool for the analysis of large samples of stellar spectra. We have applied it to a sample of 17,274 metal-poor dwarf stars with low-resolution spectra from SEGUE, using a grid of synthetic spectra with the parameter range of $[-3.0, -0.5]$ dex in metallicity, $[5000, 8000]$ K in effective temperature and $[3.5, 5]$ dex in surface gravity, covering a wavelength range of $[3850, 5200]$ Å. From the CaII, Balmer and MgIb lines, which are the strongest absorption features identified in SDSS spectra, we estimated the metallicity with averaged accuracies of 0.24 dex, the temperature with 130 K and $\log g$ with 0.5 dex, corresponding to the 1σ errors. Surface gravity is a poorly constrained parameter using these data, mainly due to the lack of sensitive features of this parameter (apart from some degree of sensitivity of the wings of the MgIb triplet) and the considerable noise in the spectra when compared to high-resolution spectra. Additional information to the spectra, such as photometry, would help to constrain the gravity parameter more. MAχ has the option to simultaneously fit different spectral windows. We have compared estimates of the parameters using the whole spectrum and only those data ranges where known lines exist. Both analyses take approximately the same time and agree excellent in recovered parameters. This suggests that for these low-resolution spectra there is no need to carefully and laboriously select the spectral windows to be analyzed with MAχ, the method calculates this automatically as part of its weighting procedure.

We have comprehensively investigated the correlations of our results with those ob-

tained for the SEGUE Stellar Parameter Pipeline (Lee et al. 2008a), which reports results from a number of different methods. The results from MAχ agree well with those of the various pipelines, and any differences are consistent with those between the various accepted approaches. We are aware of the MATISSE (Recio-Blanco et al. 2006) method of parameter estimation, which uses a different combination of weighting data but is closer to the MAχ approach than the standard pipeline methods. We look forward to comparing our results with those of MATISSE when they become available. More specifically, temperature agrees excellently with the averaged temperature of SSPP, with a negligible offset of -61 K and low scatter of 112 K. Our metallicities show a tendency to be -0.32 dex lower than SSPP averages. The small scatter of 0.23 dex suggests that the different spectral features used in the analysis (mainly CaII lines) could shift the zero point of the metallicity. In any case this offset should not be matter of concern, since recently Carollo et al. (2010) has commented on a probable conservative assignment by 0.2- 0.3 dex of [Fe/H] by the SSPP for stars with low metallicities. The most pronounced discrepancy is found in surface gravity, where MAχ reports values 0.51 dex ($\sigma = 0.39$) higher than the averaged value of the pipeline. We saw that this is consistent with the discrepancies seen between other methods.

With the assumption that the spectra behave similarly under changes of the parameters, the choice of the fiducial model for the compression is free. We have created eight compressed grids using different fiducial models for the $\mathbf{b}-$vector calculation and obtain agreement between the recovered parameters. Given the low signal-to-noise of our data, it turned out to be better to use a more metal-poor fiducial model. Like that the dependence on the parameters will be focussed on the strong lines. We also discussed the systematic effects that can be introduced in the parameter estimation when using different synthetic spectral grids. Although we saw how spectra created from linear interpolations could reproduce well an original one, the continuity of the parameter distribution can be very affected. When using a grid of models avoiding interpolations we saw that the parameter distributions were continuous, with the peak and scatter of the distribution remaining equal.

As a general conclusion of this chapter, the MAχ method showed excellent performance in processing low resolution stellar spectra. It is competitive with other methods developed for the automatic analysis of large samples of spectra, making it a potential powerful tool for the future. In addition to that, we have acquired knowledge concerning massive spectroscopy, which is a new ongoing field in Galactic astronomy thanks to the current era of large surveys.

Chapter 4

MAχ for high-resolution spectra

We tested the MAχ method on a smaller sample of 28 high-resolution spectra taken from UVES/VLT. For consistency with the low-resolution implementation, metal-poor dwarf stars were selected.

The result of this test is that we demonstrated our ability to estimate the basic stellar atmosphere parameters quickly and accurately enough for a substantial sample of high-resolution spectra. While individually severe outliers appeared, the method turned out to be accurate overall for an entire population of stars. This test has been recently published in the introductory paper of MAχ (Jofré et al. 2010)

4.1   Motivation

At the time MAχ was yielding its first results on the low-resolution spectra from SDSS, the SEGUE Stellar Parameter Pipeline (SSPP, Lee et al. 2008a) was not yet available. To test MAχ, we determined the atmosphere parameters for stars that had well known parameters from the literature. The ESO archives[1] contain large amount of stars with high signal-to-noise and high-resolution. Many of them are metal-poor F-G dwarfs with an extensive literature, so we decided to use them for this purpose[2].

This application turned out to be a challenge because the parameter estimation of high-resolution spectra is very different compared to low-resolution spectra, as will be seen in this chapter. We had to dedicate careful attention to choose the best spectral range, atomic data and method to compare our results. This test shows that MAχ is also able to assess other kind of spectra apart from SDSS. This is very important when considering the new era of spectroscopy of massive surveys.

In Sect. 4.2 we present the data while in Sect. 4.3 we present the models. The fitting procedure and an example are discussed in Sect. 4.4 and our results from the different approaches to estimate the parameters is explained in Sect. 4.5. Finally, summary and conclusions are found in Sect. 4.6

4.2   Data

The spectra were obtained with UVES, the Ultraviolet Echelle Spectrograph (Dekker et al. 2000) at the ESO VLT $8\,m$ Kueyen telescope in Chile. The resolving power R is $\sim 43,000$ and the signal-to-noise is typically above 300 in our spectra. Because MAχ is an automatic fitting tool for synthetic spectra, we first had to be sure that the observed spectra could be fitted by our grid of synthetic spectra. This means that we had to have easily distinguishable unblended spectral lines and a clear continuum. For these reasons we selected a part of the red setting of the UVES spectra, which covers the wavelength range 580 nm - 680 nm, where there are many unblended lines. The sample of stars is listed in Table B.2, with the atmosphere parameters obtained by each of the techniques explained below.

4.3   Grid of high-resolution models

Modeling high resolution spectra can be very tricky. In contrast with low resolution spectra, most of the complications that spectroscopists face today, such as 3D modeling (Collet et al. 2005), Local Thermodynamical Equilibrium (LTE Asplund 2005), atomic

---

[1]http://archive.eso.org/eso/eso_archive_main.html

[2]This test was the result of a study done in close collaboration with, C. J. Hansen and J. Sobeck. Their experience with data reduction and analysis of UVES spectra were important contribution to this work. While we were applying the MAχ method to these high-resolution spectra, C. J. Hansen was obtaining the parameters through another approach in order compare consistently the stellar parameters obtained with MAχ. Finally, J. Sobeck was very helpful in the interpretations of our results.

data (Barklem & Aspelund-Johansson 2005), can be neglected when looking at the shape of a low-resolution spectrum. The shape of absorption lines at high-resolution, however, can be very affected by these complicated details and therefore the results obtained for parameter estimation. When modeling spectra in high-resolution, the following considerations have to be made:

- The microturbulence v_t is a parameter that comes from the 1D model atmospheres becomes important and must be set. The shape of some lines sensitively depends on the value chosen for v_t. This is not the case in low-resolution, hence there is no need to fine-tune this parameter. In high-resolution the set of basic stellar atmosphere parameters is ($[Fe/H], T_{eff}, \log g, v_t$). To do a proper parameter estimation we would need to create a four-dimensional grid of synthetic spectra, varying all the parameters indicated above. This goes further than the purpose of this chapter, where we aim to check the applicability of our method. Therefore we fixed the microturbulence parameter to a typical value, guided by the results of a standard "classical" spectral analysis (see below).

- To compute synthetic spectra, a list of lines with their wavelength and atomic data must be included. The atomic data consist of oscillator strength $\log gf$ and excitation potentials, which are an important source of differences in the final shape of a given line. Final results on the parameters are therefore dependent on the line list used.

- Because our models are only an approximation of reality, we are not able to reproduce properly a broad wavelength range as in the low-resolution case. The assumption of LTE and 1D plane-parallel atmosphere layers and the uncertainties of the atomic data introduce errors. In addition to that, high-resolution spectra have an immense amount of absorption lines. Only because of these reasons, global fit becomes difficult, when not impossible. This are general problems in stellar spectroscopy. We decided to selected windows of a limited spectral range with limited chemical elements that would give us the information of the parameters, and fitted the observed spectra only in these.

We determined the three parameters temperature, metallicity and gravity using this time only neutral and ionized iron lines. Neutral lines are sensitive to temperature and single ionized ones to gravity (Fuhrmann 1998). The metallicity was effectively obtained from both FeI and II, for a given temperature and gravity. In the wavelength range of 580nm - 680nm, we have six FeII lines and 20 FeI ones that are unblended and strong enough to be present in most metal-poor stars of our sample. The lines are indicated in Table B.1, where wavelength and $\log gf$ values are listed. The $\log gf$ values and excitation potentials are taken from Nissen et al. (2002) and the VALD database (Kupka et al. 2000).

Our grid of high-resolution models covers a range in metallicity of $-2.5 \leq [Fe/H] \leq -0.5$, in effective temperature of $5500 \leq T_{eff} \leq 6600$, in surface gravity of $3.5 \leq \log g \leq 5$ and in scaling factor for normalization from 0.85 to 1.15. The grid steps are the same as in Sect. 3.3. The models have $[\alpha/Fe] = +0.4$ and $v_t = 1.2$ km/s, according to the values obtained for our stars with the "classical" method (see below).
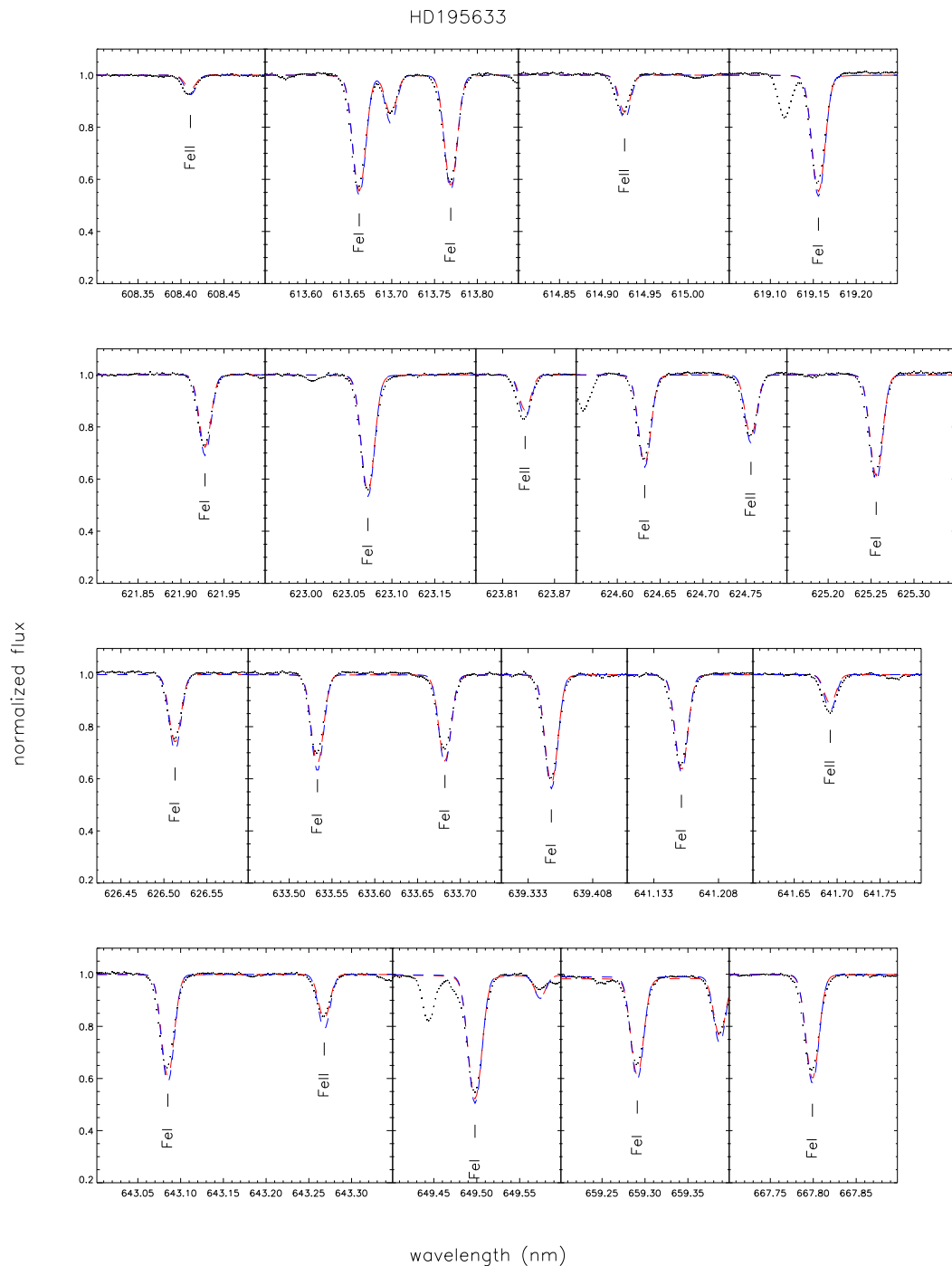
Figure 4.1: Fit of the spectrum of the star HD195633 (points) with the best model (red dashed line). The parameters of the synthetic spectrum are [Fe/H] = -0.5, T_{eff} = 6318 K and $\log g$ = 4.61, with χ^2 = 6.31. The blue line corresponds to the model with [Fe/H] = -0.6, T_{eff} = 6005 K and $\log g$ = 3.86 (χ^2 = 7.31), obtained with the "classical" approach. Each panel represents a spectral window where the lines from Table B.1 are labeled at the bottom.

4.4   Fitting high-resolution spectra

The preparation of the data was carried out as explained in Sect. 2.4. For the automatic fitting we decided to work with normalized spectra for this test. At this resolution, neither the polynomial-fitting approach by Allende Prieto et al. (2006) nor IRAF[3] were able to automatically find a good pseudo-continuum. Hence, the observed spectra were normalized interactively using Midas (Crane & Banse 1982) by C. J. Hansen, while the synthetic spectra were computed with normalized flux. We are aware that this can drive to systematic errors. The compression procedure and parameter recovery are following the steps explained in Sect. 2.4. Compressing the grid of high-resolution spectra takes more time than for the low-resolution one, but this has to be carried out only once to obtain a new grid of $y-$numbers.

4.5   Results of the high-resolution analysis using MAχ

Figure 4.1 shows an example fit of HD195633 (points) with the best MAχ model (red line) and the model with parameters found with the "classical" method (explained below) with the blue line. Each panel represents a sequence of spectral windows with the lines of Table B.1 used for the parameter estimation. All three parameters were determined simultaneously and the best fit corresponds to the model with parameters of [Fe/H] = -0.5, T_{eff} = 6318 K and $\log g$ = 4.61. The final parameters of all stars in this sample are given in Table B.2. The first column of the table indicates the name of the star and the six next ones are the parameters found with two different MAχ analyses. The first set ("free") corresponds to the standard approach of determining all parameters simultaneously from the spectrum only. The parameters are also plotted in the upper panel of Fig. 4.2. In the second variant ("restricted") the gravity is determined independently using Eq. (14), which will be introduced below, where the parameters are plotted in the lower panel of Fig. 4.2. The last four columns are the parameters obtained from the "classical" approach (below), which are used to compare with the "free" and "restricted" results.

4.5.1   Results of a "classical" analysis

In order to compare our MAχ results, we analyzed the spectra with a classical procedure, determining the stellar parameters through an iterative process. The method is similar to that of Nissen et al. (2002):

For the effective temperature it relies on the infrared flux method, which provides the coefficients to convert $(V - K)$ colors to effective temperatures. We applied the color calibration of Alonso et al. (1996), after converting the K 2MASS filter (Skrutskie et al. 1997) to the Johnson filter (Bessell 2005) and de-reddening the color. The extinction was

---

[3]IRAF is distributed by the National Optical Observatory, which is operated by the Association of Universities of Research in Astronomy, Inc., under contract with the National Science Foundation.

taken from Schlegel's dust maps (Schlegel et al. 1998) in the few cases where we could not find the values in Nissen et al. (2002, 2004).

Surface gravities were determined using the basic parallax relation

$$\log g \;=\; \log \frac{M}{M_\odot} + \log \frac{T}{T_\odot} + 0.4\,(V_o + BC) + 2\log \pi + 0.12 + \log g_\odot, \qquad (4.1)$$

where V_o is the V magnitude corrected for interstellar absorption, BC the bolometric correction and π the parallax in arcsec. We adopted a different mass value for each star based on those of Nissen et al. (2002), which are between 0.7 and 1.1 M$_\odot$. The bolometric correction BC was calculated with the solar calibration of $BC_\odot = -0.12$ as in Nissen et al. (1997).

The equivalent widths of neutral and ionized iron lines were used to determine the metallicity [Fe/H]. It was obtained using `Fitline` (François et al. 2007), which fits Gaussians to the line profiles. The equivalent widths computed from these Gaussians fits were converted to abundances by running MOOG (Sneden 1973, Sobeck priv. comm. 2008) with the plane-parallel LTE MARCS model atmospheres of (Gustafsson et al. 2008), which differ from those used for MAχ. The line list contains the lines of Table B.1 and more lines taken from bluer wavelengths in the range 300 - 580 nm (Hansen, priv. comm. 2009).

Finally, the value for the microturbulence was found by requiring that all the equivalent widths of neutral lines should give the same Fe abundance.

In order to obtain the four parameters in this way, we started with an initial guess for each of the interdependent parameters. After determining them with the above steps all values will change due to the interdependence, hence we had to iteratively determine the parameters until their values showed a negligible change. We are aware that our metallicity based on FeI lines is ignoring any non-LTE effects (Asplund 2005; Collet et al. 2005). But since neither the classically nor the MAχ analysis are taking this into account, the results obtained by both methods can still be compared.

The upper panels of Fig. 4.2 show the results of metallicity (left), temperature (middle) and gravity (right) for the entire sample of stars. The $x-$axis shows the results of the automatic fitting MAχ and the $y-$axis the "classical" parameter estimation (EW). The one-to-one line is overplotted in each figure and the legend indicates the mean of the differences (MAχ - EW) and its standard deviation, denoted as offset and scatter, respectively. Each point corresponds to a star of Table B.2 with parameters obtained by the "free" method.

Gravity shows a scatter of $\sigma = 0.46$ dex and a negligible offset. The determination of the gravity from FeII lines has always been a problematic task: Fuhrmann (1998) in an extensive study of parameters of nearby stars showed that surface gravities of F-type stars located at the turn-off point can easily differ by up to ~ 0.4 dex if derived from either LTE iron ionization equilibrium or parallaxes. The amount of ionized lines (gravity dependent) present in the spectra is usually smaller than that of neutral ones (temperature dependent). By performing an automatic fitting of weighted spectra that contain only six FeII lines compared to 20 FeI lines, a scatter of 0.46 dex is reasonable.
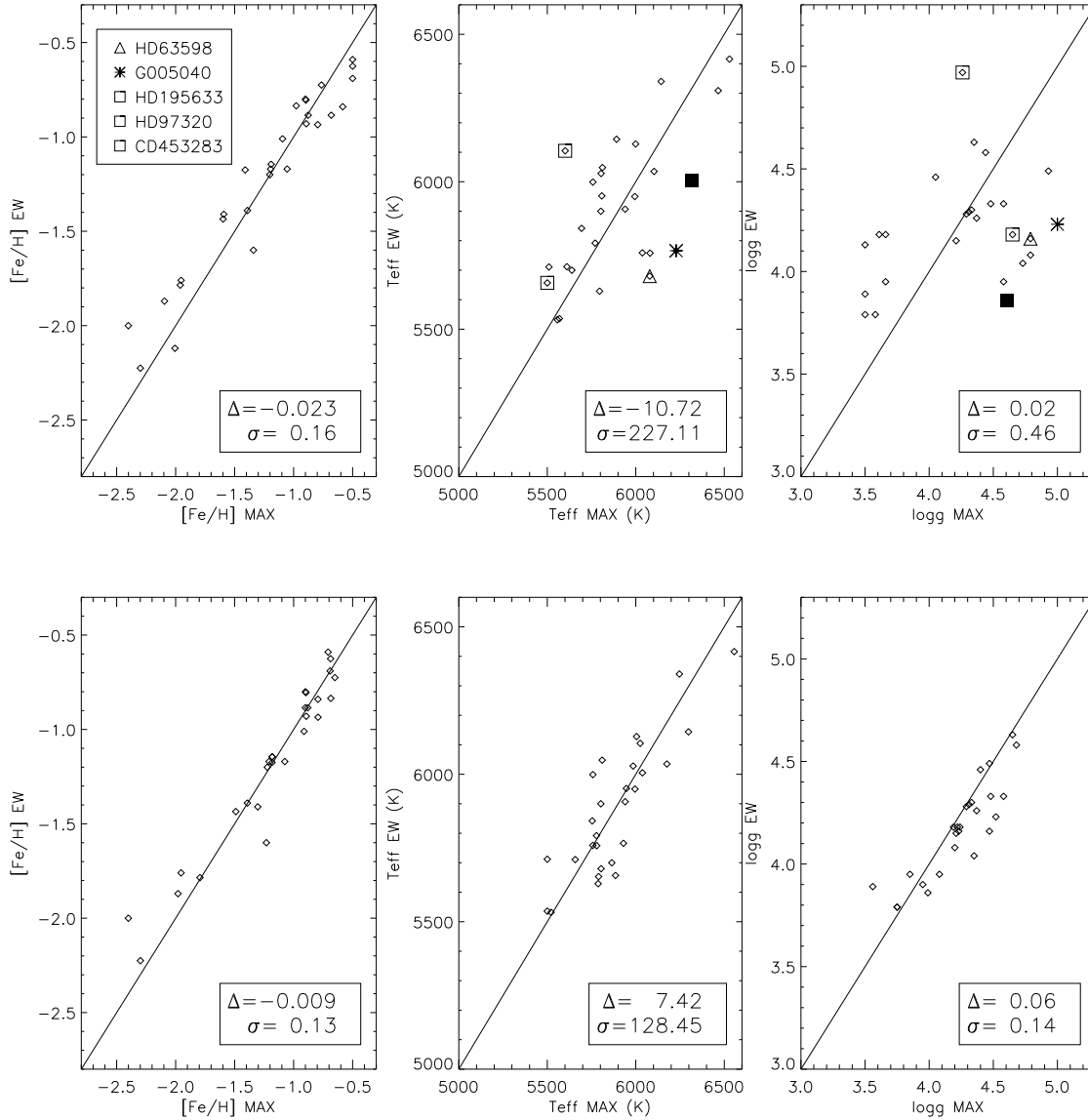
Figure 4.2: Upper panels: Correlations between the results obtained with the automatic fitting (MAX) and the classical method (EW) for metallicity (left), temperature (middle) and gravity (right). In each panel, the one-to-one line is overplotted and a legend containing the mean difference (in the sense "EW-MAχ") and its standard deviation. Here the three parameters were determined simultaneously and directly from the spectra by our method. The stars with special symbols are indicated in the legend and correspond to special cases where the offset between the two methods is particularly large (discussed in text). Lower panels: As upper panels, but MAχ results were obtained forcing the method to find the best-fitting model close to the gravities computed from the parallax formula, Eq. (14). Individual data can be found in Table B.2 (columns "MAχ, free" for the upper case and "MAχ, restr." for the lower one).

The result for the effective temperature shows a very small offset of only -10 K, but a quite large scatter of $\sigma = 227$ K. Given that two different methods were employed to determine it, this still appears to be acceptable. The scatter may also be affected by our fixed value for the microturbulence, which was taken from the average of the values found with the EW approach (see Table B.2), but which in individual cases it can differ severely.

One can decrease the scatter in the temperature difference by removing the three most discrepant objects from the sample. The star HD63598 (triangle) has an offset of 398 K. The Schlegel maps give a de-reddening for this star that is unrealistically large, so instead we set it to zero. This led to a temperature that was too low. Jonsell et al. (2005) have found a temperature of 5845 K for this star, reducing the difference to 233 K with respect to our result. The star G005-040 (asterisk) is the second case, where the offset is 462 K. For this star, the continuum subtraction was not perfect in every spectral window, resulting in a fit where the parameters were quite unreliable. Finally, the weak lines of the observed spectrum of HD19445 pushed MAχ to the border of the grid. The parameters in this case were undetermined. By removing these three stars from our sample, the scatter for temperature is reduced to 197 K.

Metallicity, on the other hand, shows a very good agreement, with a negligible offset of 0.02 dex and a scatter of 0.16 dex (upper left panel of Fig. 4.2). The lines used for the automatic fitting (MAχ) and for the classical analysis (EW) are in most cases identical, except for the lowest metallicities, where some of them are hardly visible. In these cases the classical method also resorted to other lines outside the MAχ wavelength range. The atomic data are identical, but the value for microturbulence are not, as mentioned before. In view of all this, the very good correlation of metallicity is encouraging.

4.5.2 "Restricted" parameter recovery

An example for the individual fit of the best MAχ model to the observed spectra was shown in Fig. 4.1 for HD195633, which is shown as a filled symbol in Fig. 4.2 and is one of the objects with the most pronounced discrepancies (see also Table B.2). Nevertheless, the two synthetic spectra appear to fit equally well the observations ($\chi^2 = 6.31$ for the MAχ model and $\chi^2 = 7.31$ for that obtained from the classical analysis). We could not decide from the χ^2 values which method leads to a more accurate parameter determination for this star. One would need independent information of the spectrum about this star to reach conclusions about its parameters.

It is also interesting to notice from the upper panels of Fig. 4.2 that stars with large discrepancies in gravity (for example those with special symbols) also give large discrepancies in temperature. They show a quite unsatisfying fit for the FeII lines. Motivated by this, we did an additional test by restricting MAχ to the determination of the parameters with input values for $\log g$ obtained from the EW method, i.e. we found a local maximum point of the likelihood in a restricted area. To do this we chose the three closest gravity values from our grid of synthetic spectra to the classical one found with Eq. (4.1) – see Col 9 of Table B.2 – and we searched for the maximum point within this range. For some cases we did not find a local maximum in the $\log g$ space, and the final estimation went to

the border of the grid, as the case of CD-3018140, where $\log g = 3.5$. The general tendency is a local maximum close to the input EW-value.

Now the agreement with the classical method for the effective temperatures became excellent, with a negligible offset of only 7.42 K and a scatter of 128 K, as seen in the lower panels of Fig. 4.2. Gravity was also better constrained, with a small scatter of 0.14 dex and a negligible offset. Note that we did not necessarily obtain identical values, because the MAχ gravity is obtained by using the value from Eq. (4.1) only as input, and we were looking for a final solution close to this value. The behavior of the metallicity does not change with respect to the "free" case, demonstrating the robustness of the determination of this parameter. The results obtained when using parallaxes for the initial guess for $\log g$ are summarized in Table B.2 in the columns under the heading "MAχ, restr.".

It is instructive to discuss the implication of this comparison. For the "classical" EW method we determined the parameters making use of the best information available and of the freedom to adopt the method to each star individually. The iterative process allowed us to decide where to stop the iteration, or, if no satisfying convergence could be reached, to draw on the options to move to another spectral window, to use other lines, or disregard problematic lines. Moreover, the continuum could be separately subtracted for each line, thus creating locally perfect normalized flux levels. For the effective temperature, the more reliable infrared flux method employing photometric data could be used instead of only relying on spectra. The advantage of determining $\log g$ independently was already demonstrated. On the other hand we were attempting an estimate of the parameters only from the spectral information without fine-tuning the models or fit procedure for each star for our automatic MAχ method. Given this, the comparison with the full interactive method is surprisingly good. We demonstrated that by using additional information for one parameter (here $\log g$) it becomes even better for the remaining two quantities. Table B.2 shows our final parameter estimate for our stars, when we make use of the parallaxes as additional information. In particular, [Fe/H] is rather robust (see Fig. 4.2) and this is the most important parameter for us.

4.6 Summary and conclusions

We have applied the MAχ method on a sample of 28 high-resolution spectra from VLT-UVES, where no offset in metallicity was seen. In this case we have carefully chosen the models and spectral range for comparing our parameter estimation against a "classical" approach: temperature from photometry, surface gravity from parallaxes and metallicity from equivalent widths of neutral and ionized iron lines. We have calculated the parameters ourselves to avoid additional systematic offsets that various different methods would introduce in stellar parameter scales. These results were compared with the automatic fitting of 20 FeI and 6 FeII lines (that coincide in most cases with the equivalent widths calculations) made by MAχ. We obtained large scatter in gravity and temperature (0.44 dex and 220 K, respectively), but no systematic offset. The normalization of the continuum in some cases was not perfectly done, making it difficult to fit every line properly:

especially for the FeII lines. They produce a scatter in gravity, which drives a scatter in temperature. We have seen in our fits that our best model does not differ very much from the model with parameters found by the "classical" approach. Motivated by this we decreased the scatter in gravity by using additional information than the spectrum, i.e. using the gravities determined from parallaxes as input value. This forced our method to find a local maximum point of the likelihood close to this input gravity value. Fixing the gravity gave an improved agreement in temperature, now with a scatter of 128 K. Metallicity does not change when forcing gravities, thus illustrating the robustness of determination for this parameter.

The main result of this test is that we have shown our ability to estimate [Fe/H], T_{eff}, and $\log g$ quickly and accurate enough for a significant number of stars. Although some cases were severely off in comparison with the referent "classical" parameters, the method showed to have potential when dealing with the analysis of large number of stars. For this purpose "classical" methods would be much too slow and tedious. The MAχ method may also serve as a quick and rough estimate for a more detailed follow-up analysis.

MAχ is a rapid fitting technique and is independent of model and data used. It will work for any star for which an appropriate grid of synthetic spectra can be calculated. Although the grid calculation is time consuming, it only needs to be performed once allowing an extremely rapid processing of individual stars.

Chapter 5

Main-Sequence Turn-Off

The luminosity and temperature (color) of main-sequence turn-off stars are commonly used to study properties of globular clusters because both are very sensitive to the age and metallicity of their stars. At this point the star has its highest effective temperature during its main evolution. The turn-off of the youngest Milky Way halo population is given by the hottest stars of a field population with a certain metallicity. We present in this chapter two different methods to detect the turn-off by finding these stars in a sample of field halo stars from SDSS. In addition, we show that our results for the turn-off are unbiased by selection effects.

5.1   The turn-off temperature

To determine ages of individual field stars, their chemical composition, mass and distance should be known accurately. For halo stars this is usually not the case, but an alternative way is to use the turn-off (TO) temperature of stellar populations.

During the main-sequence, a low-mass star $(0.3 < M < 1.5M_\odot)$ energy source is provided by fusion of hydrogen in its core. While the star is burning hydrogen, a helium-core starts to grow from the center through pp-chain nuclear reactions. These reactions are slow, e.g. the timescale is $\tau_n = 6 \times 10^9$ years (Hansen & Kawaler 1994) for low-mass stars, meaning that those stars at late main-sequence phases are old. During the main-sequence, the temperature and luminosity increase due to core hydrogen-burning. Once all hydrogen in the core is used up, hydrogen-burning takes place in a shell around the helium-core and the star leaves the main-sequence.

The fusion in the hydrogen-containing layer directly above the helium-core causes the outer layers away from the core, where the effective temperature decreases, which makes the star be redder than when it was on the main sequence. The star becomes a red giant.
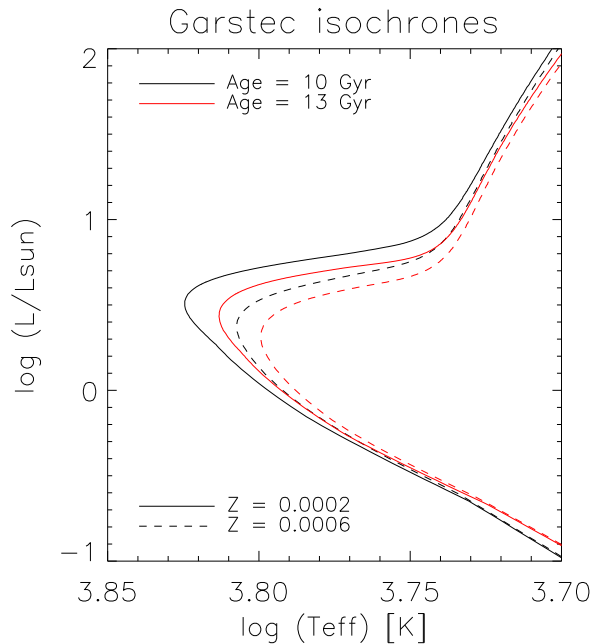
Figure 5.1: The luminosity and temperature of the turn-off are dependent on age and metallicity of the stars. Isochrones from stellar tracks computed with the program GARSTEC (Weiss & Schlattl 2008) of 11 and 13 Gyr represented with black and red lines, respectively. Solid lines are for those with $Z = 2 \times 10^{-4}$ and dashed line for those with $Z = 6 \times 10^{-4}$.

The evolutionary point where the star leaves the main sequence is called *turn-off*, and its luminosity and temperature in the Hertzsprung-Russell (HR) diagram depend on the age, the chemical composition and the mass of the star. As an example, Fig. 5.1 displays

different isochrones (GARSTEC; Meissner & Weiss 2006) along the HR diagram, which are curves of stars with the same age and metallicity, but different masses. From the figure we can see that the higher the age, the less luminous and colder is the TO. An analogous effect is seen for chemical composition, where the TO of a metal-rich isochrone is colder and less luminous than a metal-poor one. This information has been largely used to determine the ages of globular clusters (Chaboyer et al. 1996; VandenBerg et al. 2000; Meissner & Weiss 2006, and references therein). Descriptions of the turn-off point can be found in the introductory books of Carroll & Ostlie (2006), Kippenhahn & Weigert (1990) and Hansen & Kawaler (1994). Futher details about the evolution of low-mass stars are beyond the purpose of this chapter, where we only want to emphatize the behavior of the temperature near the Main-Sequence Turn-Off (MSTO). The key idea here is that, for a sample of stars in evolutionary stages before the red giant branch, the *turn-off corresponds to the stars with highest temperatures.*

Theoretical isochrones can provide more precise age-dating technique for stars at the TO when the absolute magnitude and the mass of the star is not known. Gilmore et al. (1989) state that if independent abundance estimates are available, then any measure of the temperature of the *hottest* turn-off stars measures the age of the *youngest* stars in a tracer population. An example of what is mentioned above is illustrated in Fig. 5.2. The upper panel is an HR diagram where the curve corresponds to a theoretical GARSTEC isochrone of 11 Gyr and metal fraction of $Z = 2 \times 10^{-4}$ (which corresponds to a metallicity of $[Fe/H] = -1.70$, see Chap. 6). The MSTO point is indicated with the red vertical line. The lower panel shows the temperature distribution of field dwarfs and sub-giants taken from the SDSS/SEGUE survey at a metallicity of $[Fe/H] = -1.70 \pm 0.15$. Atmosphere parameters were estimated from their spectra using the MAχ method (Jofré et al. 2010) explained in Chap. 2 and the application to SDSS/SEGUE spectra described in Chap. 3. The red vertical line is the MSTO of the 11Gyr isochrone from the upper panel, which agrees with the hottest stars of the field population. This suggests that the field population may have at least an age of 11 Gyr. Note there are a significant number of stars hotter than the value given by the red vertical line. These stars are blue horizontal branch stars and blue metal-poor stars. The latter is subject of critical discussions in the last decades, where it is believed that they are blue stragglers or a younger population coming from other galaxies and later on accreted on to the Milky Way (Preston et al. 1994; Preston & Sneden 2000)

Note that an older population, which would have a redder turn-off color, as seen in Fig. 5.1, may well be hidden in this sample. Without the information of distance and mass, we are not able to distinguish only from the temperature distribution if this star is a giant or a dwarf of 11 Gyr. Moreover, this star could also belong to the turn-off of an older population. In any case, for the analysis of stellar populations, the temperature (color) of the main-sequence turn-off point is a crucial quantity. This chapter is dedicated to an extensive study of the TO-determination in metal-poor halo field populations from the SDSS/SEGUE catalog. We first explain two methods to identify the turn-off in Sect. 5.2. Then we introduce the metallicity-temperature diagram in Sect. 5.3 to explore of the MSTO for the Galactic halo in Sect. 5.4. Finally, a summary and conclusions are given in Sect. 5.5.

5.2   Turn-Off detection methods

When determining the age of a star from the main-sequence turn-off temperature, it is very important to assure that this evolutionary point is found correctly. Stars with a given metallicity value can have different temperatures distributed as seen in lower panel of Fig.5.2. While at low temperatures the number of stars increases smoothly, at high temperatures there is an abrupt decrease in the number of stars. If we have a dominating stellar population present, we can interpret this drop as its MSTO point, and techniques to quantify it are explained below. By comparing the results obtained from different techniques we are able to constrain the final value of the MSTO. We first describe two techniques, Cubic Fit and Sobel Kernel, in Sect. 5.2.1 and Sect. 5.2.2 respectively. We then estimate the errors of the turn-off in Sect. 5.2.3 and finally we compare both methods in Sect. 5.2.4.
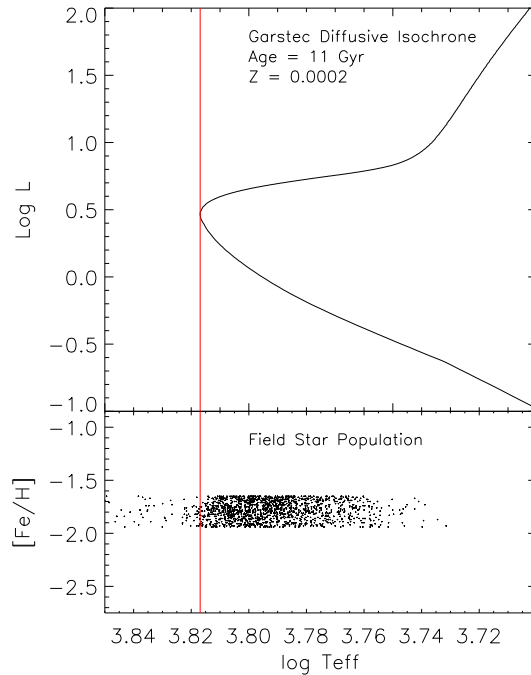
Figure 5.2: Lower panel: Effective temperature of a SEGUE field star population with metallicities in the range of [Fe/H] = -1.70 ± 0.15. Upper panel: 11 Gyr GARSTEC isochrone with metal fraction Z = 2×10^{-4}, which corresponds to the metallicity of the field population. The turn-off point of the isochrone is represented by the vertical red line, which agrees with the TO of the field population. This agreement suggests an age of about 11 Gyr for the field stars at the turn-off.

5.2.1 Cubic Fit

A naive idea to find the TO is to perform a polynomial fit to the drop of the temperature distribution. A simple approach is to use a cubic fit, which is shown in Fig. 5.3A and B for a stellar sample of $[Fe/H] = -1.95 \pm 0.15$. For the polynomial fit we took the values of the histogram at the drop as a function of the temperature and we fit a third order polynome, which is illustrated by the blue dotted line of panel B. The TO-temperature corresponds to the inflection point of the polynome, because it represents the extreme of the derivative, i.e. the major rate of decrease in the temperature distribution. This point is found by performing second derivatives to the cubic function and looking for the zero point. The TO-temperature is shown with a red vertical line in the left panels of Fig. 5.3. The error obtained for the detection, which is plotted with vertical dashed lines, was calculated as will be explained in Sect. 5.2.3.
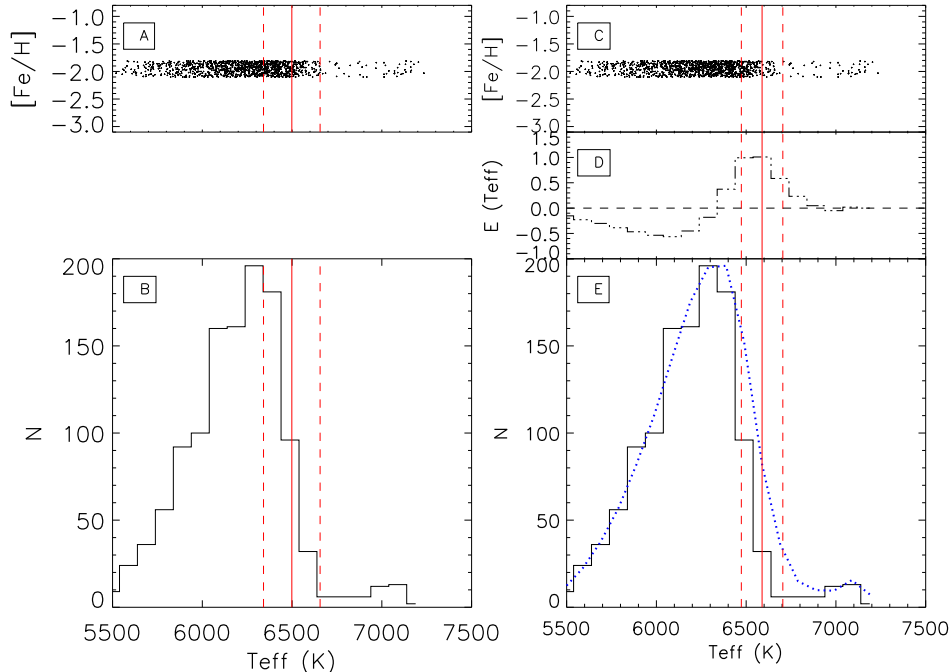
Figure 5.3: Example of Cubic Fit (left panels) and Sobel Kernel (right panels) technique used to detect the turn-off. The TO is indicated by the red vertical lines, with the dashed lines corresponding to their errors. Panel A: Temperature distribution the field stars with $[Fe/H] = -1.95 \pm 0.15$. Panel B: Histogram of a temperature distribution and the cubic fit with the blue dotted line. Panel C: Same as panel A. Panel D: Sobel Kernel filter response given by Eq. (5.2). Panel E: Histogram of temperature and the probability function of Eq. (5.1) with the blue dotted line.

This technique has the disadvantage of being very sensitive to the binning used for the temperature distribution. In addition, for smaller star samples – where the temperature distribution shows a less clear drop at the turn-off point – the performance of an automatic cubic fit becomes very difficult and therefore the TO-detection is unreliable. However, this

technique is very simple to understand so we keep it to compare with our second method explained below.

5.2.2   Sobel Kernel edge-detection

For low-mass metal-poor stars, the bolometric luminosity of the Tip of Red Giant Branch (TRGB) is almost constant. Lee et al. (1993), Madore & Freedman (1995), Sakai et al. (1996) and Tabur et al. (2009) have used this knowledge to estimate distances of galaxies. Through histograms of the luminosity function they determine the position of the TRGB by finding the luminosity where the count discontinuity is the greatest. They adopt a standard image-processing edge-detection technique to measure the magnitude of the Tip, which is called Sobel Kernel. The main ingredient is a first derivative operator that computes the rate of change across an edge, where the largest change corresponds to the edge, e.g the Tip.

Like the Tip of the Red Giant Branch shows an edge in the luminosity function of galaxies, the main-sequence turn-off shows an edge in the temperature distribution function of stellar populations, and the Sobel Kernel can also be applied to this case. In the following the edge-detection method is explained briefly only, but for further details see Lee et al. (1993), Sakai et al. (1996), Tabur et al. (2009), and references therein.

Consider a continuous probability distribution function to model the histograms. This produces that the dependencies of binning in the temperature are avoided and the errors of the measurements are also included. The probability distribution is defined by

$$\Phi(T_{\text{eff}}) = \sum_{i=0}^{N} \frac{1}{\sqrt{2\pi}\sigma_i} \exp\left[-\frac{(T_{\text{eff}} - T_{\text{eff,i}})^2}{2\sigma_i^2}\right], \tag{5.1}$$

where $T_{\text{eff,i}}$ and σ_i are the temperatures and their uncertainties, respectively, and N the total number of stars in the sample.

The edge-detector filter applied to this temperature function is

$$E(T_{\text{eff}}) = \Phi(T_{\text{eff}} - \Delta T_{\text{eff}}) - \Phi(T_{\text{eff}} + \Delta T_{\text{eff}}), \tag{5.2}$$

where $E(T_{\text{eff}})$ is the filter response at the temperature T_{eff} and ΔT_{eff} is the bin size. Note that Eq. (5.2) has the signs opposite when compared with Eq. (A2) of Sakai et al. (1996). This is because the luminosity function is dependent on magnitudes, which have a decreasing scale.

The right panels of Fig. 5.3 illustrate this technique. Panel C is a repetition of panel A. To visualize better the Sobel Kernel technique we have plotted in panel C again the temperatures of a stellar population with [Fe/H] $= -1.95 \pm 0.15$. Panel E has the temperature distributions with a histogram and the probability distribution with the blue dotted line. The Sobel Kernel response given by Eq. (5.2) is in panel D, where the maximum response

is indicated with a red vertical line. The temperature value of the maximum is interpreted as the MSTO. Dashed lines correspond to errors in the detection (explained below).

5.2.3 Uncertainties in the turn-off detection

Méndez et al. (2002) and Tabur et al. (2009) use the bootstrap method (Babu & Feigelson 1996) to estimate uncertainties in the magnitude of the Red Giant Branch Tip, because it is robust and widely documented. Since our task is similar to the TRGB detection, we decided to use the same method to study the errors.

A bootstrap resampling simulates the act of making the same observation multiple times. This allows realistic estimates of the standard deviation in the mean. Consider a stellar population with temperature function Φ. From this function we determine the turn-off $T_{\mathrm{eff,TO}}(\Phi)$ with one of the methods described above. We then randomly resample, with replacement – i.e. a star may appear more than once or not at all –, all the stars of the stellar population and we consider only a randomly selected sample containing the 80% of the resample. We repeat the procedure to detect the TO, this time using the temperature function from the latter subsample Φ^*, and we obtain $T_{\mathrm{eff,TO}}^*(\Phi^*)$.

By bootstrap resampling 500 times we take the standard deviation of the distribution $T_{\mathrm{eff,TO}}^*(\Phi^*)$ as the 1σ error in the measurement of $T_{\mathrm{eff,TO}}(\Phi)$. We consider the uncertainty in our detection as 3σ, which corresponds to 99% of probability for the star being at the turn-off. The uncertainties for our sample with [Fe/H] = -1.95 are plotted in Fig. 5.3 with red dashed lines. Comparing the values obtained for errors of both methods, we can see that the TO-detection obtained with the Sobel Kernel filter is more accurate than that obtained with the Cubic Fit.

Effect of errors in metallicity measurements

The effect of the metallicity measurement accuracies of about 0.25 dex in the final TO-detection were analyzed with Monte Carlo simulations. For a star with metallicity value $[\mathrm{Fe/H}]_0$ and error $\sigma_{[\mathrm{Fe/H}]_0}$ we gave a random value distributed as a Gaussian in the range of $[[\mathrm{Fe/H}]_0 - \sigma_{[\mathrm{Fe/H}]_0}, [\mathrm{Fe/H}]_0 + \sigma_{[\mathrm{Fe/H}]_0}]$. This was done for each star and then we looked for the turn-off in this new sample. As in the previous case, we repeated this process 500 times and calculated the standard deviation of the TO-determination.

Monte Carlo simulation moves the stars in a perpendicular direction to that of where the TO is detected. Therefore it is expected that an error in the metallicity determination does not affect the temperature distribution (and the determination of the TO) significantly. We found, however, a significant effect on the TO-detection errors due to the metallicity bin size used for the temperature distribution. This happens if the metallicity bin size is smaller than the averaged $2\sigma_{[\mathrm{Fe/H}]_0}$, because a star can move from one bin to the other, which makes the temperature distribution change. For example, a star located on the second metallicity bin can well be located on the third bin during the next resample. In the same way, a star that was in the first sample at the third bin, can be during the next resample at the second one. These two stars have different temperature values

and therefore the temperature distributions will be different in both resamples. Like this an effect in the TO-detection is produced, which is similar to the bootstrapping method explained above. In this case we exclude stars from each metallicity bin due to movements of the Monte Carlo simulations and in the previous case we excluded them by considering randomly 80% of the stars from the resample, meaning that this effect becomes important for smaller stellar samples. In the left panel of Fig. 5.4 we have plotted the error due to temperature bootstrapping ("Boot") with the dashed line and the error due to Monte Carlo simulations of metallicity measurements with the solid line. The binning in the metallicity for the temperature distribution was 0.2 dex, which is smaller than the $2\sigma_{[Fe/H]_0}$ accuracies of the metallicity measurements of 0.25 dex. We can see how both curves behave similarly, where the error in the TO-detection becomes larger at the metal-rich side. This happens because at high metallicities there are less stars (discussed in detail below), meaning that a resampling of them will affect more the shape of the temperature distribution.
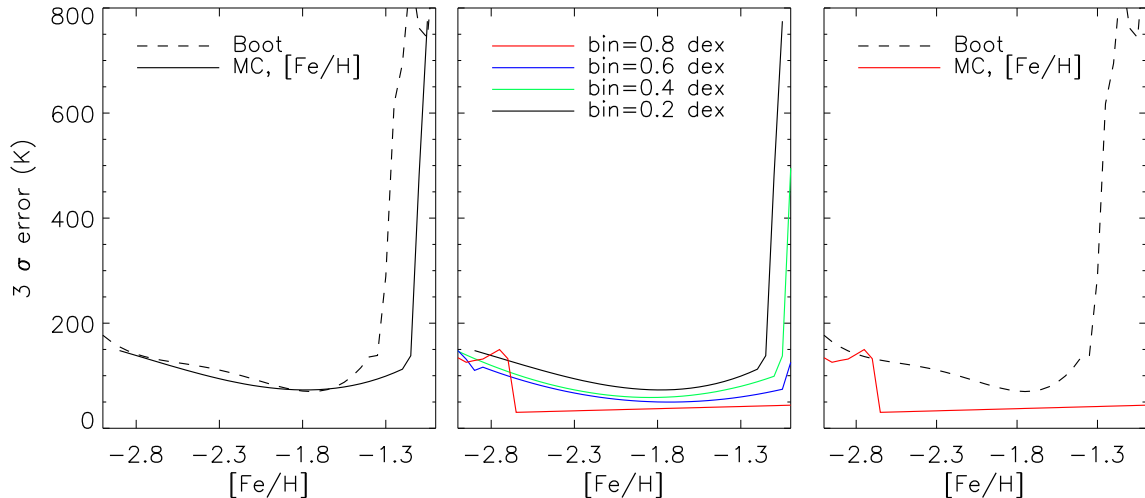
Figure 5.4: Left panel: errors in the TO-determination due to bootstrapping method in temperature (Boot, dashed line) and due to Monte Carlo simulations of metallicity measurement (MC, [Fe/H], solid line) considering a metallicity bin size of 0.2 dex. Middle panel: errors in the TO-determination with Monte Carlo simulations using different metallicity bin size. Right panel: as left panel, but considering the bin size of 0.8 dex for MC.

In case that the binning is much larger than the averaged $2\sigma_{[Fe/H]_0}$ errors of the metallicity measurements, there is less probability that a star is moved from one bin to the other one. The temperature distribution of the stars at each metallicity bin in the different Monte Carlo simulations remains equal and the TO-detection variates less. This is shown in the middle panel of Fig. 5.4, where different curves represent the standard deviation of the TO-determination using different sizes in the metallicity binning. We can see how the errors become smaller with larger binning size, even at high metallicities, where we do not have so many stars. When the binning gets too large, the TO-detection becomes less accurate at the metal-poor border. For a last comparison we have plotted at the right panel of Fig. 5.4 again with the dashed line the error due to temperature bootstrapping

("Boot") and with the solid line the error due to Monte Carlo simulations of metallicity measurements. In this case the binning in the metallicity for the temperature distribution was of 0.8 dex, which is much larger than the $2\sigma_{[Fe/H]_0}$ errors of the metallicity measurements. It can be seen how the errors due to metallicity measurements become negligible when compared with the bootstrapping ones.

We must take into account that the cut-off at the turn-off becomes noisy if the metallicity bin is too large. We need to find an agreement for the optimal size of the binning so that the errors due to metallicity are small but without loosing accuracy in the bootstrapping method. A in intermediate binning size of ~ 0.4 dex would still give an accurate turn-off determination, where the errors due to metallicity measurements would still smaller than those obtained with bootstrapping.

Note that the "Boot" curve has its minimum at $[Fe/H] = -1.7$, which is related with the maximum amount of stars in the sample, as will be seen in Sect. 5.2.3. Allende Prieto et al. (2006) studied the metallicity distribution of F and G SDSS stars. As discussed in detail in Chap. 3, their atmosphere parameters have an offset of ~ 0.3 dex with respect to ours. The peak in their metallicity distribution for halo stars is at $[Fe/H]$= -1.4, which is exactly 0.3 dex higher than our peak in the metallicity distribution at $[Fe/H]$= -1.7. In addition, Carollo et al. (2007) have found a peak in the metallicity distribution for the inner halo at $[Fe/H]$= -1.6.

5.2.4 Sobel Kernel v/s Cubic Fit

To see that the turn-off value is independent from the method used to detect the edge, we have compared the results obtained with the Sobel Kernel and Cubic Fit techniques. This is displayed in Fig. 5.5, where in panel A we have directly compared the temperatures for different metallicities, including the 3σ bootstrapping errors described in Sect. 5.2.3. The TO-temperatures as a function of metallicity are displayed in panel B, with blue diamonds representing Sobel Kernel and red triangles the Cubic Fit technique. To visualize better the trend, we performed a quadratic polynomial fit on the values obtained for each method, it is illustrated with solid lines of the respective colors. Finally, the difference of both quadratic fits as a function of metallicity is shown in panel C, with $\Delta = Sobel - Cubic$, where the dashed line illustrates a linear fit of the difference.

There is an excellent agreement of both techniques when including the errors, which can be seen in panel A, where the turn-off temperature decreases with increasing metallicity, as is seen in panel B. Similar trends were found by Gratton et al. (1997) and Salaris & Weiss (1998), who calculated correlations between the $(B - V)$ colors and metallicities of unevolved main-sequence stars ($M_V = +6$) in globular clusters and field stars with accurate *Hipparcos* distances (ESA 1997).

Note that there are two TO-values that are off the general Cubic Fit trend at high metallicity, which are encircled in panel B. They have colder TO-temperatures than those obtained with the Sobel Kernel, so that at high metallicities there is a large discrepancy between both methods. The TO-detection at these two metallicity values have also larger errors, which we can see in Panel A. As commented before, at high metallicities our stellar

sample has less stars than at lower metallicities and the Cubic Fit technique yields an unrealistic turn-off temperature.

In general terms, the mean difference between both methods of 57.7 K is reasonably small compared with the errors obtained for the turn-off itself or for the temperature determination from the spectrum, which are of about 100 K. The smallest difference at the metal-poor end is 16.28 K while the largest difference is 99.2 K at the metal-rich end. The latter value could be decreased if we exclude the values obtained for the two high metallicities, as discussed above. Motivated by the negligible difference between both methods employed to detect the turn-off we chose to use the Sobel Kernel filter, because of its smaller uncertainties and broader documentation, together with its robustness and binning independency.
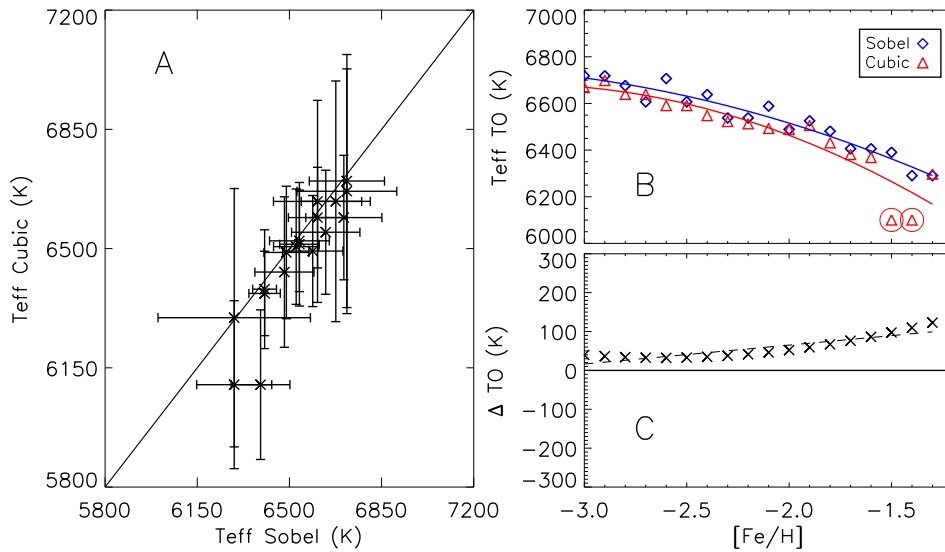
Figure 5.5: Panel A: comparison of the TO-temperature obtained by using the Sobel Kernel and the Cubic Fit technique along the one-to-one line with their respective errors. Panel B: TO-temperature as a function of metallicity. Blue diamonds are the values obtained with the Sobel Kernel technique and red triangles are those obtained with the Cubic Fit one. A quadratic polynomial fit is represented by the solid line of the respective colors. Circles distinguish the TO values that are off the general trend (see text). Panel C: Difference (Δ = Sobel-Cubic) of the quadratic fits, with the dashed line illustrating a linear fit.

5.3   Metallicity - Temperature diagram

We are not only interested in the value of the turn-off as a function of metallicity, but also in the distribution of stars in the parameter space of temperature and metallicity. This distribution helps to understand possible biases due to selections effects, as will be discussed in the next sections.
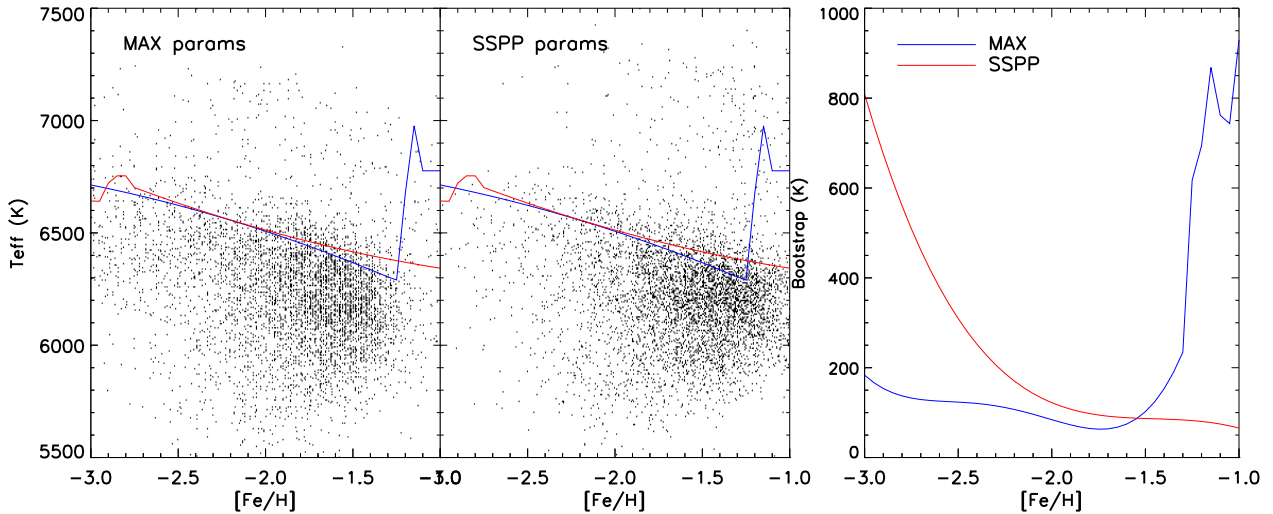
Figure 5.6: Left panel: Temperatures and metallicities of the *TO poor* stellar sample (see Table 5.1) for the atmosphere parameters estimated with MAχ. Middle panel: As left panel, but with the adopted SSPP (Lee et al. 2008a) atmosphere parameters. Blue line corresponds to MSTO temperature for the MAχ parameters and red line to that of SSPP ones. Right panel: Errors in the TO detection as a function of metallicity.

We introduce here the Metallicity - Temperature ([Fe/H] - T_{eff}) diagram, which relates the metallicity of a sample of field stars to their temperatures (or colors, see Chap. 7). As an example, we have plotted the metallicity and temperature of the *TO poor* sample (see Table 5.1) in the left and middle panels of Fig. 5.6. The stars were selected to be metal-poor turn-off stars from a color-color diagram. For this stellar selection the atmosphere parameters determined with MAχ (Chap. 2 and 3) are plotted with black dots in the left panel of Fig. 5.6. As a comparison we have also plotted the same stars but with the adopted SSPP atmosphere parameters (Lee et al. 2008a, see below). In the [Fe/H] - T_{eff} diagrams, the turn-off stars define an upper envelope, which trace the youngest population at any given metallicity. The blue line indicates the MSTO as a function of metallicity obtained using the Sobel Kernel technique discussed above for the MAχ parameters and the red line for the SSPP parameters. Similar diagrams can be found in Allende Prieto et al. (2006), Schuster et al. (2006), Unavane et al. (1996) and references therein. They use photometric colors and based the MSTO on the bluest point, while here we based the MSTO on the direct spectroscopic temperatures. The advantage of using the spectroscopic temperatures is that we avoid color transformation when using theoretical isochrones to determine ages (see Chap. 6 for more details).

As a first application of the [Fe/H] - T_{eff} diagram, we have compared the distributions of the parameters obtained by using MAχ and those obtained by the SEGUE Stellar Parameter Pipeline (SSPP, Lee et al. 2008a,b; Allende Prieto et al. 2008b). The extensive discussion between the MAχ and SSPP parameters is found in Chap. 3 and Jofré et al.

(2010), where in Table 3.1 and Fig. 3.4, we saw that there is a negligible general offset in effective temperature of 61 K, but a considerable one of more than ~ 0.3 dex in metallicity. We looked for the turn-off using the atmosphere parameters of MAχ and SSPP, which can be seen in Fig. 5.6. The MSTO as a function of metallicity for both samples are plotted in the left and the middle panels. The differences in metallicity can seen in the right and middle panel of Fig. 5.6 in the stellar distribution along the [Fe/H] - T_{eff} diagrams. At the metal-rich regime we see a considerable amount of stars for the SSPP parameters, while for the MAχ parameters we do not. In a similar way, the metal-poor regime is more populated for the MAχ parameters than for the SSPP ones. It is worthy to remark that the offset of ~ 0.3 dex in metallicity does not mean that every star is shifted by this value in metallicity. We can see in Fig. 5.6 how the peak of the distribution is shifted, but the shape of the distribution is slightly different for MAχ and SSPP parameters. This is especially seen at low metallicities, where the [Fe/H] values between MAχ and SSPP parameters deviate the most. We recall the recent comment made by Carollo et al. (2010) about the low [Fe/H] estimates of SSPP, which are 0.2 - 0.3 dex higher than those values recovered by high-resolution analyses.

In general, the different distributions do not yield significantly different values of the turn-off temperature for [Fe/H] < -1.2. The lack of MAχ metal-rich stars does not allow to detect an edge for [Fe/H] > -1.2. In a similar way, the lack of SSPP metal-poor stars affects the determination of the TO at [Fe/H] < -2.7. The bootstrap errors, which are plotted in the right panel of Fig. 5.6 with the respective colors, become larger at low metallicities for the SSPP parameters and at high metallicities for the MAχ parameters. This is because the different amounts of stars seen in the metal-poor and metal-rich regime for SSPP and MAχ parameters, as discussed above. More stars yield a more accurate edge-detection (see Sect. 5.2.3).

The errors of the TO-detection for the SSPP parameters decrease smoothly with increasing metallicity, which agrees with the shape of the parameter distribution in the [Fe/H] - T_{eff} diagram of the middle panel in Fig. 5.6. It is possible to see how the number of stars increases gradually towards higher metallicities. The errors of the TO-detection for the MAχ parameters, however, are relatively small for metallicities below -1.4, point at which the errors increase abruptly towards higher [Fe/H]. This can be seen in the left panel of Fig. 5.6, where we can see how the stars disappear abruptly at high metallicities. This does not introduce significant effects when determining the ages, as will be discussed in Chap. 6.

5.4   The Turn-Off for different stellar samples

To assure that the upper envelope seen in Fig. 5.6 corresponds to the main-sequence turn-off stars of the youngest halo population, we must show that the finding of the envelope is not biased by selection effects of the stellar sample. For this purpose, we explored different stellar samples selected from the SDSS-DR7 survey (Abazajian et al. 2009). The stars contained in SDSS-DR7 have a large contiguous area of the Northern Galactic Cap (Legacy

survey) and also the specific spectroscopic plates from the SEGUE survey (Yanny et al. 2009b). We selected the stars considering different color criteria, positions and data quality. This section is a comparison of the MSTO determined for the different stellar selections to show that the turn-off is robust and reliable. In addition, this section discusses how the errors of the TO-determination are mainly sensitive to the quantity of stars.

5.4.1   SDSS/SEGUE Target selections

The targets of SDSS and SEGUE were selected primarly from photometry in the *ugriz* filter system (Fukugita et al. 1996). There are many works that have studied the properties of the *ugriz* filters as indicators of stellar type (e.g. Lenz et al. 1998; Morrison et al. 2000; Helmi et al. 2003; Jurić et al. 2008; Ivezić et al. 2008). The SEGUE primary target selection algorithms were designed considering these works in order to focus on special stars and achieve more efficient the SEGUE science goals. The main scientific goals were characterizing large-scale stellar structures in the Galaxy, such as the thick disk, the halo and its streams.

One basic stellar evolution principle used to study stellar populations of the Milky Way is that of "the longer an evolutionary phase of an individual star, the larger the number of stars is observed in that particular phase" (Prialnik 2000). Late main-sequence F- and G-type dwarfs are then abundant and good tracers of large-scale stellar structures; also because they are more luminous than stars at early main-sequence phases, making them easier to observe at large distances. There are therefore many target algorithms based on finding F-G dwarf stars near the turn-off. Additional aims of finding rare but scientifically interesting samples of objects of unusually low metallicity, odd spectral type or extreme kinematics were also considered for the target selection designs. Details of selection criteria can be found in the SEGUE paper of Yanny et al. (2009b) and references therein. We used the samples "F subdwarfs" (F), "Low Metal" (LM), "Low Latitude Blue" (LL) and "F/G" from Yanny et al. (2009b), because they were built to detect especially dwarfs or metal-poor stars in the halo. The color constraints of the samples are indicated in Table 5.1 but for further details see Table 5 of Yanny et al. (2009b).

A color-color diagram is helpful to understand the distribution of the stars and the target selections criteria. We have placed a radomly selected sample of 8,000 SEGUE stars in Fig. 5.7, where the color boxes are the constraints of the SEGUE target selections, indicated in the upper part of Table 5.1. They are represented in red (LM), green (F), pink (FG) and blue (LL) for better visualization. In addition, the Blue Horizontal Branch (BHB) stars are bounded by a cyan box in Fig. 5.7. This group is indicated below the horizontal line of Table 5.1 because the color selection was not made for targeting F-G dwarfs. We do not use it to detect the MSTO, but it is important to keep these stars in mind, since those BHB stars with a redder $g - r$ color overlaps with the bluest $g - r$ color of the dwarfs. Therefore we expect a contamination with BHB stars in the [Fe/H] - T_{eff} diagrams and the MSTO detections.

Apart from these five samples, Table 5.1 includes the samples *TO poor* and *G blue*. We have not plotted their constraints in Fig. 5.7 because they are not part of the primary

Sample	photometric constraints
F	$g < 20.3, 0.4 < u - g < 1.4$
	$0.2 < g - r < 0.7, \ -0.7 < \mathrm{P1}(s) < -0.25$
LM	$r < 19, -0.5, g - r < 0.75$
	$0.6 < u - g < 3.0, \ l > 0.135$
LL	$g - r < 0.25$
F/G	$0.2 < g - r < 0.48$
BHB	$0.8 \leq u - g \leq 1.5$
	$-0.5 \leq g - r \leq 0.2$
TO poor	$0.7 \leq u - g \leq 1.0$
	$0.1 \leq g - r \leq 0.5$
G blue	$0.1 \leq u - g \leq 0.48$

Table 5.1: Target selection of different samples of SEGUE using *ugriz* color constrains with $\mathrm{P1}(s) = 0.91(u - g) + 0.415(g - r) - 1.28$ (Helmi et al. 2003) and $l = -0.436u + 1.129g - 0.119r - 0.574i + 0.1984$ (Lenz et al. 1998). The first column corresponds to the name of the sample and the second one to the color constrain.

SEGUE target selections. The *TO poor* sample was our first sample, which contains especially metal-poor dwarfs close to the turn-off. We used it as a first sample to calibrate the MAχ method and we have kept it here because it serves for comparison. The *G blue* sample is an optimal combination between the target-selection samples indicated in the upper part of Table 5.1, as will be explained below.

In addition to the color selections, we see in Fig. 5.7 how the majority of the stars detected by SDSS are on the main sequence (according to over 98% Finlator et al. 2000; de Jong et al. 2010). They follow a well defined sequence and are usually referred to as a "stellar locus" in color-color diagrams (Lenz et al. 1998; Smolčić et al. 2004). The bluer part of the stellar locus at $[u - g, g - r] \sim [1.0, 0.2]$ corresponds to F-G dwarfs and subgiants (Smolčić et al. 2004; Jurić et al. 2008). The red part of the stellar locus at $[u - g, g - r] \sim [2.5, 1.5]$ corresponds to M - K giants (Morrison et al. 2000; Helmi et al. 2003; Yanny et al. 2009a), while the locus at $[u - g, g - r] \sim [0.5, -0.2]$ indicates white dwarfs and quasars (Smolčić et al. 2004; Ivezić et al. 2008; Jurić et al. 2008). Finally, that locus at $[u - g, g - r] \sim [0.2, 1.2]$ correspond to blue horizontal branch stars (Lenz et al. 1998; Sirko et al. 2004; Jurić et al. 2008).

We dedicated a large efford exploring the different target selections and properties of the SDSS stars in the color-color diagram in order to find the best stellar sample for the final turn-off value. For an extensive study of the color constraints in the final MSTO-detection we used the atmosphere parameters provided by the SEGUE database. It is clear that the proper analysis of this test should be done by considering our own results for the atmosphere parameters, but the decision to show here the results obtained by using the SSPP parameters was done because of the following reasons: Firstly, the SSPP and MAχ parameters lead to the same value for the turn-off temperature as a function of metallicity. Secondly, to carry this test, we investigated deeply the shape of the color-
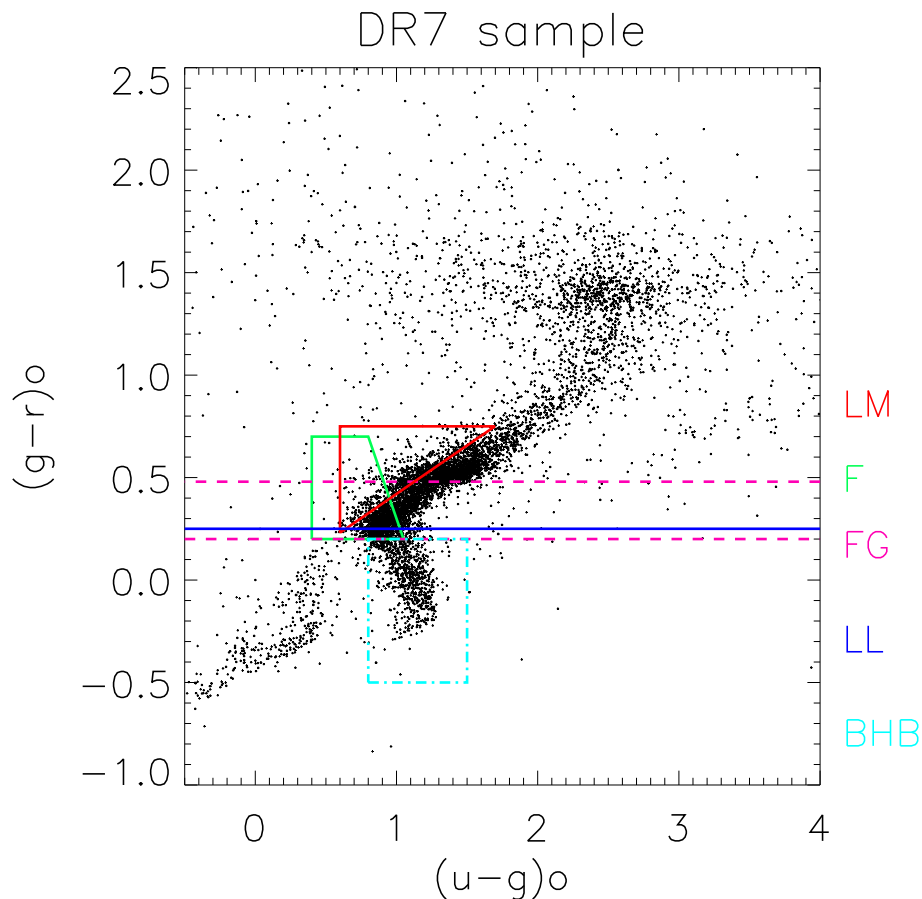
Figure 5.7: Color-color diagram of the de-reddened *ugr* magnitudes. The colored boxes illustrate the constraints of the SEGUE target selections (see Table 5.1), with LM red, F green, LL blue and FG pink. In addition, the color selection of Blue Horizontal Branch is indicated with the cyan dotted line.

color and [Fe/H] - T_{eff} diagrams when considering different color target selections. To understand these selection criteria and dependencies in the final turn-off detection, we tried more than twenty different samples. The purpose of this section is to understand the SDSS database in respect of biases of the turn-off detection under different color criteria, and *not* to give a final value of the turn-off temperature as a function of metallicity. We will use our own parameters at the end of this chapter to give absolute values for the MSTO. For a proper analysis using MAχ, we would approximately three times as much as the time required to perform this test performed here. The reason is the implementation of technical details to the MAχ core; such as a parallelization in order to analyze simultaneously different stellar samples. An algorithm is required to select from SDSS the stars in a way

such that MAχ does not analyze them repeated times[1]. Additionally, the time needed to assess 50,000 stars for each of the samples must be considered, in particular when considering the errors in the estimations. Since part of the achievement of a PhD thesis in constrained timescales consists in looking for solutions to develop the project as complete as possible, we decided to keep aside the MAχ code for this particular test. In this section we show the MSTO of four relevant stellar samples that we found during the performance of this test: *TO poor*, *Halo* $= F \bigcup LM \bigcup LL$, *FG* and *Gblue*.

1. *TO poor* sample

   The [Fe/H] - T_{eff} diagram was already illustrated in the middle panel of Fig. 5.6. The blue line indicates the turn-off temperature as a function of metallicity for SSPP parameters and the red line for the MAχ parameters, as discussed above. The stars are mainly located close to the turn-off line, as expected from the tight color constraint. The upper envelope does not show a significant presence of hotter stars.

2. *Halo* sample

   The second sample used for the comparison is a union of the samples LL, LM and F indicated in Table 5.1 and we called it *Halo*. The [Fe/H] - T_{eff} diagram for these stars, together with the color-color diagram can be seen in panel A and B of Fig. 5.8, respectively. The MSTO as a function of metallicity is also plotted in panel A with a blue line. The green line corresponds to the MSTO obtained from the *FG* sample (see below). Note the lack of stars at redder regions in the stellar locus of the color-color diagram due to selection effects at panel B. For stars with [Fe/H] > -1.2, the edge detection yields drastically higher temperatures. As an explanation, we have plotted a sample of 1,000 randomly selected stars with $T_{eff} > 6800K$ with cyan color in panel A. They correspond mainly to BHB stars, as can be seen in the color-color diagram of panel B. Note some of them might be related to blue metal-poor stars (BMP; Preston et al. 1994), which have hot temperatures but are located in the stellar locus of the color-color diagram. Discussion of these stars are found in Chap. 6. Although the large number of BHB stars affects the determination of the TO at high metallicities, the majority of halo stars have [Fe/H] < -1.2, where the MSTO is well detected.

3. *FG* sample

   The *FG* sample represents a metallicity unbiased random subsampling of subdwarfs in the color range described in Table 5.1 and Yanny et al. (2009b). To compare

---

[1]This issue was several times discussed during the SDSS collaboration meeting in Paris in September 2010

better, we have plotted the [Fe/H] - T_{eff} diagram at panel C next to that of the *Halo* sample in Fig. 5.8. Panel D is the color-color diagram for these F-G stars. The turn-off as a function of metallicity is indicated with the green line, which was also plotted in panel A for comparison. In addition, the MSTO from the *Halo* sample is plotted in this panel with the blue line.

The [Fe/H] - T_{eff} diagram of this sample, in contrary to that of the *Halo* one, does not show a large contamination of BHB stars. In fact, F-G stars define a clean upper envelope in the [Fe/H] - T_{eff} diagram, which is given by the color cut of the color constraint. The turn-off has a tendency of being colder, especially at low metallicities. This can be explained by looking at the color-color diagram at panel D, where the bluest turn-off stars (those with $g - r < 0.2$) have been excluded of the sample due to the color constraint. A color cut of $g - r = 0.2$ will not include the most metal-poor turn-off halo stars. Note that we still see BMP stars after the drastic exclusion of the blue horizontal branch stars.

4. *G blue* sample

   Motivated by the results obtained above, where we saw how a large contamination of BHB, together with the lack of blue stars from the main stellar locus affects the MSTO edge-detection, we considered a new combined sample, which we call *G blue*. The color constraint is indicated in Table 5.1 and is similar to the *FG* one but includes stars in the color range of $0.2 > g - r > 0.1$. Note that these blue stars will produce a contamination of BHB, but also will add the missing metal-poor MSTO ones seen in panel D of Fig. 5.8.

   The [Fe/H] - T_{eff} diagram of the *G blue* sample is illustrated in the left panel of Fig. 5.9 , and the color-color diagram at the right panel. It can be seen how the main stellar locus is now complete – i.e. the locus has now stars with colors bluer than $g - r = 0.2$ – and also how a significant number of BHB stars is now included. They are present in the [Fe/H] - T_{eff} diagram at high metallicities and temperatures, but are not numerous enough to modify the Sobel Kernel edge-detection.

   The MSTOs of the four samples – *TO poor, Halo*, FG and *G blue* – are plotted in the [Fe/H] - T_{eff} diagram of Fig. 5.9 with different colors, as indicated in the legend. Although there is a considerable contamination of hot stars at the upper envelope given by the turn-off, the MSTO at high metallicities agrees with that obtained for the *TO poor* and FG samples. In addition, the inclusion of bluer stars produces higher temperatures at the metal-poor regime.

To conclude, BHB stars contaminate the edge-detection, in particular at high metallicities, where halo stars become rare. At $0.1 < g-r < 0.2$ there is an important number BHB stars, but also an important number of metal-poor main-sequence turn-off stars. Therefore, it is worthy to do a color constraint with more contamination BHB stars rather than exclude the bluest part of the main stellar locus of Fig. 5.7.
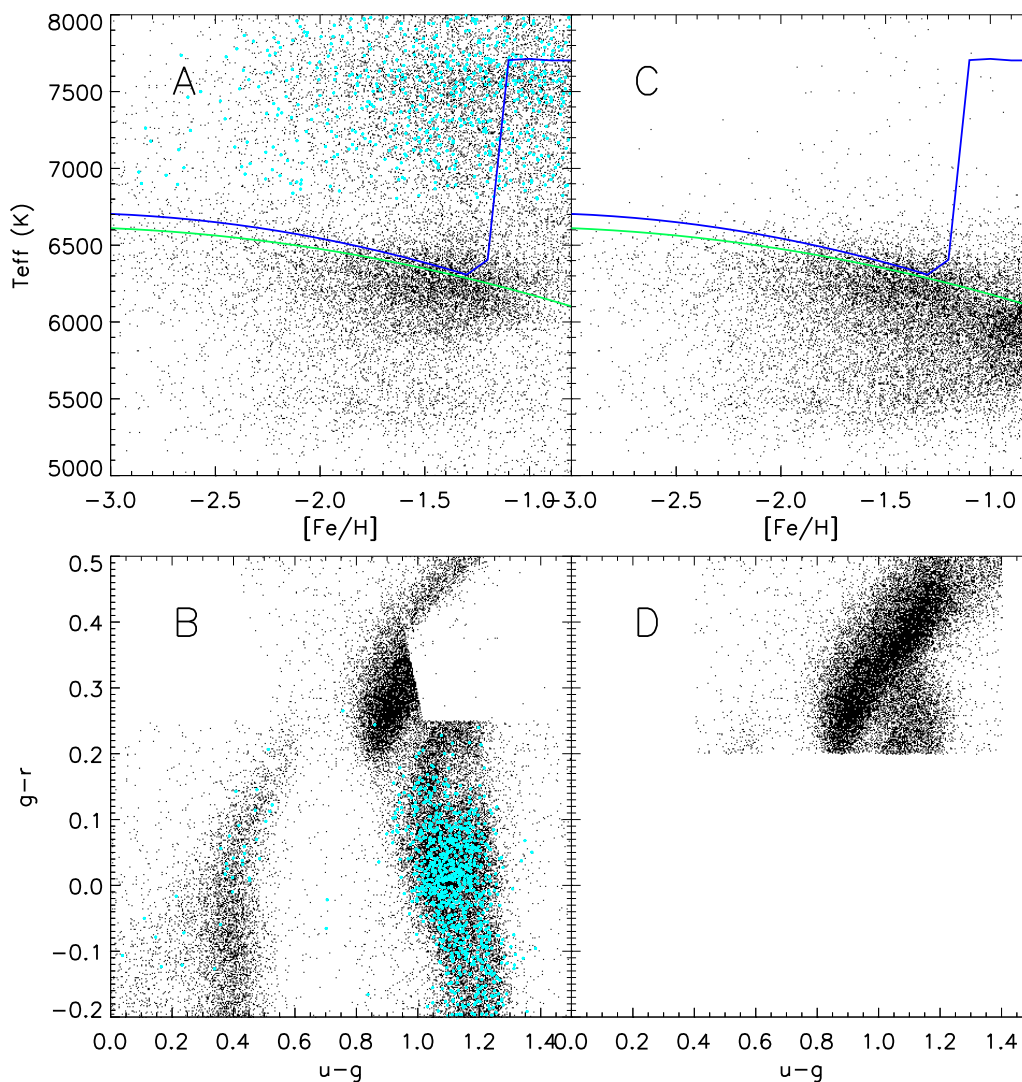
Figure 5.8: Upper panels: [Fe/H] - T$_{\mathrm{eff}}$ diagrams for two different SEGUE stellar samples using SSPP atmosphere parameters, at the left side the *Halo* (see text) and at the right side the *FG* (see Table 5.1) sample. The MSTO for each of them is plotted in both diagrams, with blue color corresponding to *Halo* and green to *FG*. Lower panels: color-color diagrams of the samples, again the left side for *Halo* and right side for *FG*.

5.4.2   Sky Selection

Another way to find biases in the MSTO for the halo is to select different parts of the sky and look for the turn-off for each subsample. For doing this, we use the stars of the *G blue* group described above, whose Galactic positions are plotted in Fig 5.10.
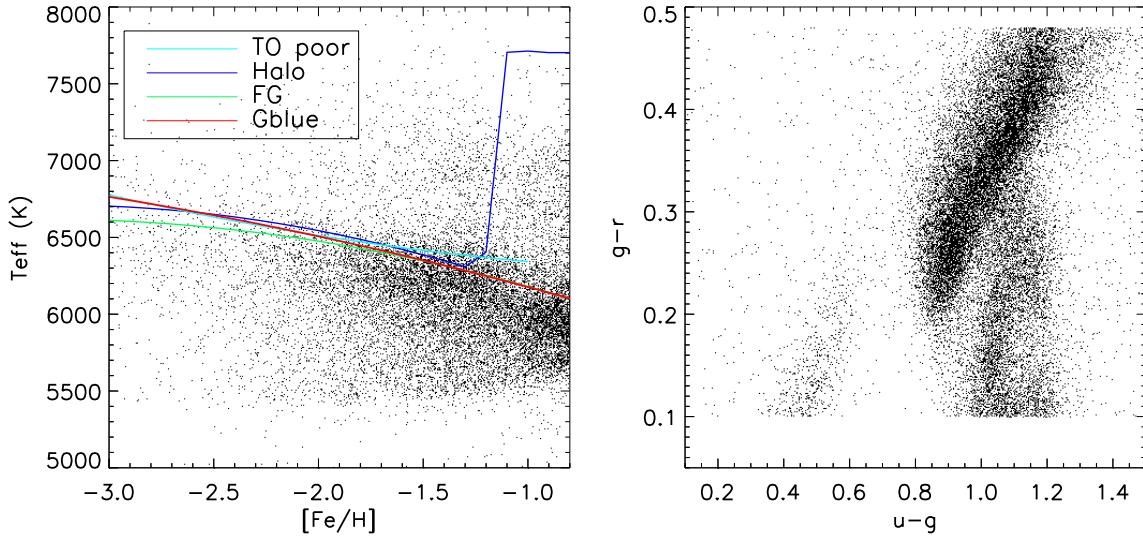
Figure 5.9: Left panel: [Fe/H] - T_{eff} diagram for the *G blue* sample. The turn-off temperatures as a function of metallicity for the samples *TO poor*, *Halo*, *FG* and *G blue* are plotted in the left panel, with the colors of each sample indicated in the legend. Right panel: color-color diagram for the *G blue* sample.

The Galactic longitude is denoted as l and the Galactic latitude as b, both measured in degrees. The circles correspond to the SEGUE special spectroscopic pointings points (Yanny et al. 2009b), which cover all areas of the sky. The background stars are those coming from the spectroscopic plates of the SDSS/DR7 Legacy Survey (Abazajian et al. 2009). Both surveys are used in this study, which is the reason why we call our sample as SDSS/SEGUE. The stars are mostly located above (and below) the Galactic plane at $b = 0°$. We have plotted constant latitudes with dashed lines corresponding to the values $b = (70, 50, 30, 0, -30, -50, -70)°$, which are used to compare the MSTO detection.

We initially took eight subsamples limited by the latitude values indicated with the dashed line in Fig. 5.10. The shape of the [Fe/H] - T_{eff} diagrams for these samples were identical for northern and southern hemisphere, with the only difference of having less stars in the southern hemisphere. The reason for this is simply that the Apache Point Observatory, where SDSS data are taken, is located in the northern hemisphere. The small number of stars was especially problematic in the domain of $-90 \leq b < -70°$, where we could not detect the turn-off. We therefore decided to join the domains of the southern and northern hemispheres for each of the Galactic latitude limits. The [Fe/H] - T_{eff} diagrams for the now four groups are illustrated in Fig. 5.11, where the regions are indicated in each panel. In addition, we have plotted the TO for each of the regions with different colors (see caption of the figure), in order to compare better the results. Note that although the MSTO is indicated only for stars with [Fe/H] < -1.2, we have included
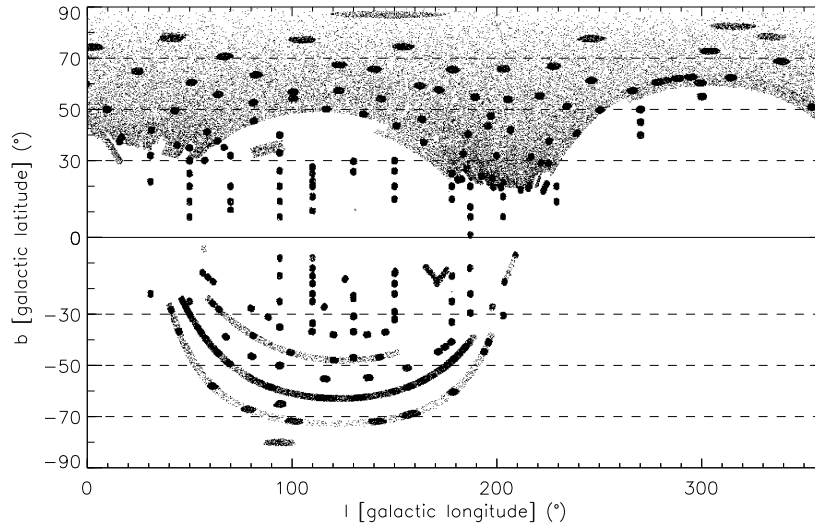
Figure 5.10: Distribution of the *G blue* sample in Galactic coordinates. The spectroscopic plate pointings are distributed across the sky. Dashed lines indicate the latitude values $b = (70, 50, 30, -30, -50, -70)°$, which mark the borders of different regions for comparison in the MSTO detection.

those with higher metallicities in the [Fe/H] - T_{eff} diagram. The reason is that they help to understand better the distribution of stars in the metallicity temperature space as a function of Galactic latitude.

The first interesting result is the shape of the [Fe/H] - T_{eff} diagram as a function of latitude. Let N_+ be the number of stars with [Fe/H]> -1.0 and N_- the number of stars with [Fe/H]< -1.0. Near the Galactic poles ($90 > |b| > 70°$) there is an almost lack of stars with high metallicities, with a ratio of $N_+/N_- = 0.052$. The number of high metallicity stars increases with decreasing Galactic latitude, whereas close to the Galactic equator ($30 > |b| > 0°$) we find more metal-rich than metal-poor stars, with $N_+/N_- = 1.24$. This is in agreement with the assumption that the Galactic pole contains mainly halo stars – e.g. metal-poor stars – and the equator contains mainly disk stars – e.g. metal-rich stars (e.g. de Jong et al. 2010). Allende Prieto et al. (2006) showed using SSPP atmosphere parameters that the thick disk has a peak in the distribution at [Fe/H]= -0.7 while the halo has its peak at -1.4. It can be seen in their metallicity distributions how the intersection between halo and disk distributions are at [Fe/H]= -1.0, which agrees with what we observe in our [Fe/H] - T_{eff} diagrams of Fig. 5.11

The second result from of this test is the agreement of the MSTO for the different regions. For the metal-poor halo stars ([Fe/H]< -1.2), the turn-off is unbiased by position selection.
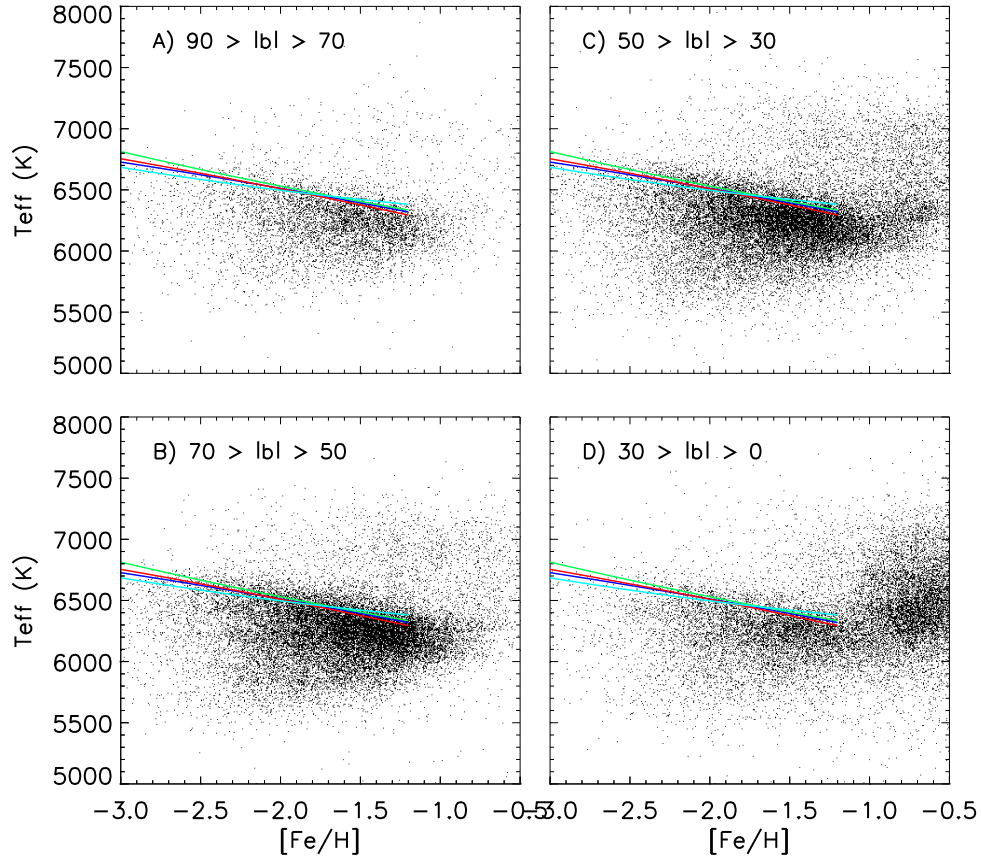
Figure 5.11: [Fe/H] - T_{eff} diagrams for four different Galactic latitudes. Color lines are the TO detection as a function of metallicity, with blue for $90 > |b| > 70°$, green for $70 > |b| > 50°$, red for $50 > |b| > 30°$ and cyan for $30 > |b| > 0°$.

5.4.3   Dependency and errors in the edge-determination

Another important test is to investigate biases due to quality and quantity of the data. For doing this, we selected subsamples with different uncertainties in the atmosphere parameters (T_{eff} and [Fe/H]) and also with different χ^2 values for the fitting in the parameter estimation. We randomly selected a sample of 20,000 stars of each of the subsamples described below. Like this we were unbiased by the size of the stellar sample, which affects the uncertainties, as will be discussed in Sect. 5.2.3. The tests here were done using the MAχ parameters because we can control better the errors and χ^2 of the fitting for our own determinations.
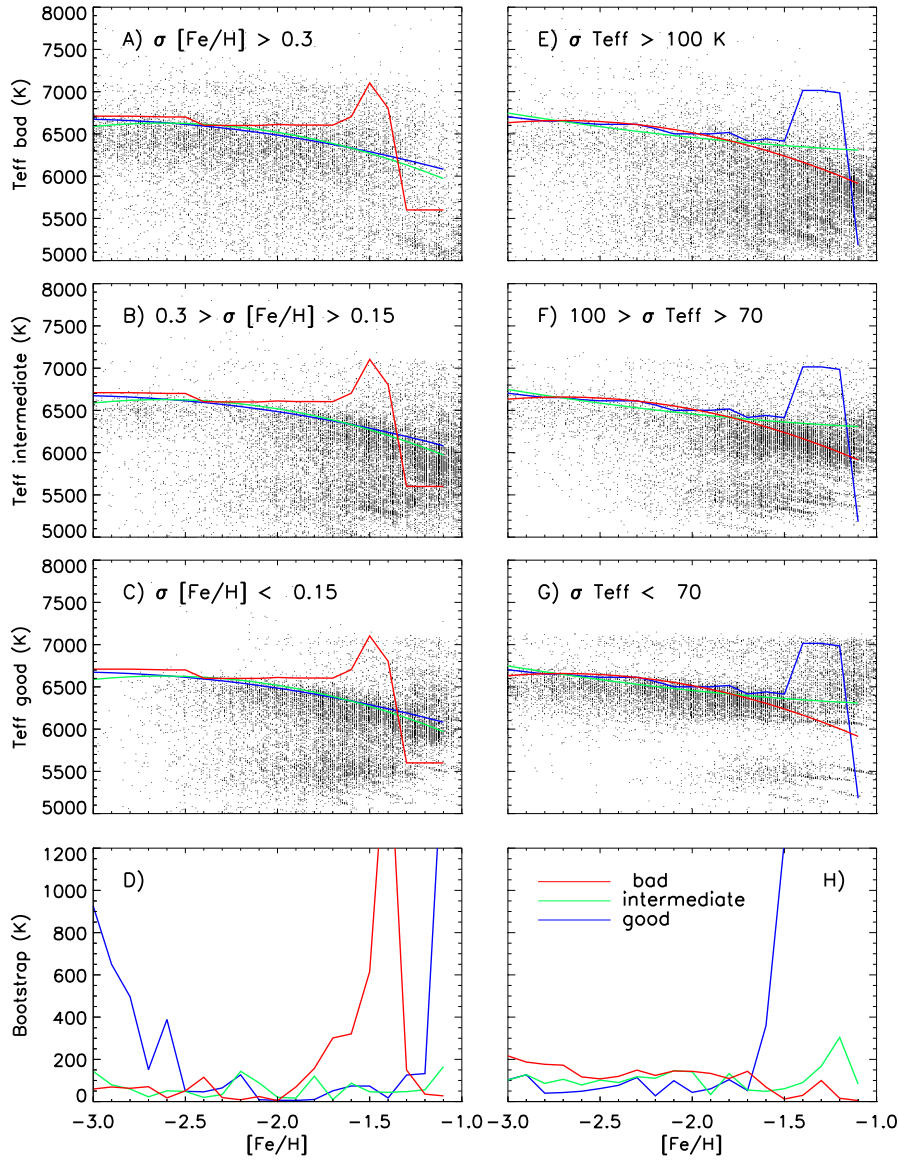
Figure 5.12: [Fe/H] - T$_{\rm eff}$ diagrams for different accuracies in the metallicity (left side) and temperature (right side) determination. Three levels of accuracy are selected to detect the TO: "bad" (red), "intermediate" (green) and "good" (blue). The domains of these levels of accuracy are indicated in each plot. Lower panels: Bootstrap error of the TO determination for each of the subsamples.

Errors in the atmosphere parameters

We have selected three subsamples with the classification of "bad" (σ[Fe/H] > 0.3), "intermediate" ($0.3 < \sigma$[Fe/H] > 0.15 dex) and "good" (σ[Fe/H] < 0.15) measurements of metallicity; as well as "bad" (σT$_{\rm eff}$ > 100K), "intermediate" ($100 > \sigma$T$_{\rm eff}$ > 70K) and

"good" ($\sigma T_{eff} > 70K$) measurements of temperature. The [Fe/H] - T_{eff} diagrams of these subsamples are illustrated in Fig. 5.12, where the left panels correspond the classifications for metallicity and the right panels for temperature. Each [Fe/H] - T_{eff} diagram contains also the MSTO for each of the subsamples, for the "bad" , "intermediate" and "good" measurements in red, green and blue, respectively. The bottom panels are the behavior of the error in the MSTO determination for the different subsamples, with each color line corresponding to the respective classification.

The distribution of stars in the [Fe/H] - T_{eff} diagram with "bad" [Fe/H] determination is scattered over the whole parameter space and does not show a clear envelope for the MSTO, as can be seen in Fig. 5.12A. For [Fe/H] > -2.0, the accuracies in the metallicity estimates become better and therefore we find less stars in panel A, which do not allow to detect a turn-off, as seen with the red line. In any case, for stars with [Fe/H] < -2.0, it is possible to detect an edge which agrees with the "intermediate" and "good" samples. The errors in the MSTO detection are also small for low metallicities, while for [Fe/H] > -2.0 they start to increase significantly, as seen in panel D. A different behavior is found at "intermediate" metallicity accuracies , where a clear envelope is seen at the complete metallicity region in Fig. 5.12B. The MSTO detection for this sample is represented with the green line and shows a smooth behavior in the errors at panel D. For "good" metallicity determinations the distribution of stars is biased towards higher metallicities. Although the MSTO detection (blue line) agrees with those of the samples discussed above, the errors at lower metallicities increase significantly, as seen with the blue line at panel D. The reason is that at low metallicities there are less "good" metallicity estimates, in the same way as at high metallicities there were less "bad" estimates.

Concerning temperature, "bad" determinations are scattered over the entire [Fe/H] - T_{eff} diagram of Fig. 5.12E and become more frequent for metal rich stars. The edge-detection is in any case well determined for a large part of the metallicity domain, with a slight increase of the errors towards low metallicities (see the red line at panel H). As in the metallicity case, for the "intermediate" temperature determinations allow an accurate and smooth MSTO detection, which is represented by the green line. Note that in the [Fe/H] - T_{eff} diagram of panel F there are considerably less stars at low metallicities which does not affect the final MSTO detection significantly. Finally, the distribution of stars with "good" temperature estimations are biased towards metal-poor stars, as we can see at panel G of Fig. 5.12. The MSTO shows a clear envelope for lower metallicities and the errors are small, but increases abruptly at [Fe/H]= -1.8, where the number of stars decreases significantly.

Value of χ^2 in the parameter recovery

As explained in Chap. 2, the atmosphere parameters correspond to those of the synthetic spectrum that fit the best the observed spectrum, meaning that MAχ yields the value of the χ^2 when recovering the parameters. We used this value to classify subsamples with different fitting qualities, selecting the stars again under the criterium of "bad" ($\chi^2 > 5.5$),
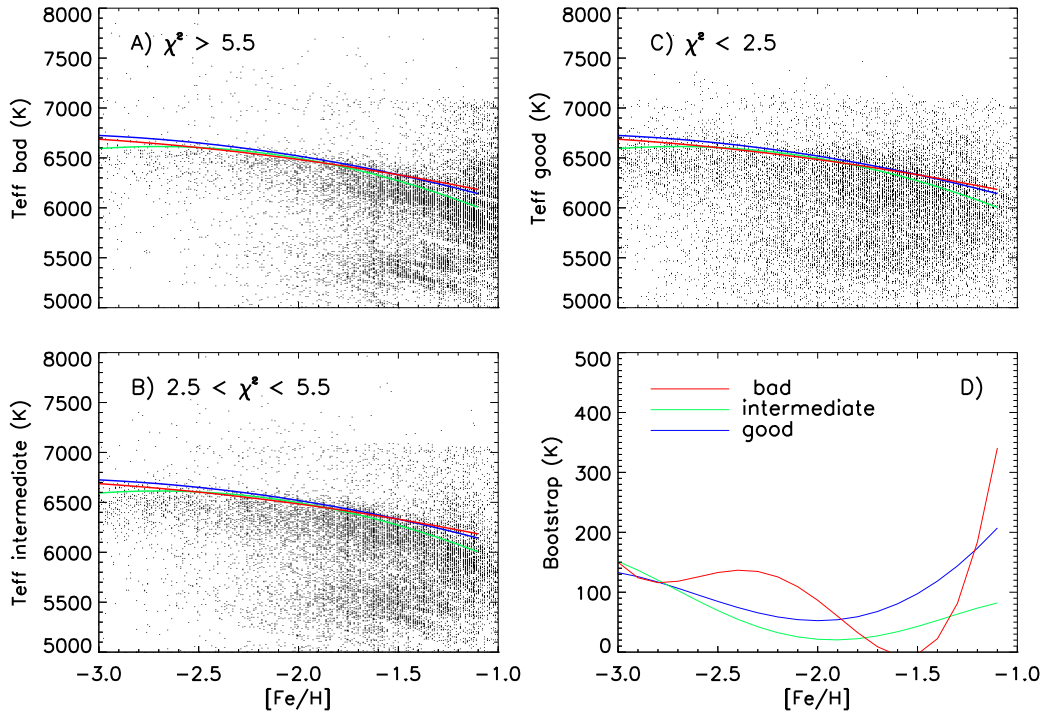
Figure 5.13: [Fe/H] - T_{eff} diagrams for different χ^2 in the fitting for the parameter estima-
tion. Three levels of accuracy are selected to detect the TO: "bad" (red), "intermediate"
(green) and "good" (blue). The domains for the χ^2 value are indicated in each plot. Panel
D: Bootstrap error of the TO-determination for each of the subsamples.

"intermediate" ($2.5 < \chi^2 < 5.5$) and "good" ($2.5 > \chi^2$) fittings. The [Fe/H] - T_{eff} diagrams
for these groups are displayed in Fig. 5.13 at panels A, B and C, respectively. The errors
of the TO-detection for each of the samples are displayed at panel D, with red, green and
blue line corresponding to "bad", "intermediate" and "good", respectively.

The "bad" fittings are biased to more metal-rich stars, where the large concentration of
stars does not show a clear turn-off. The errors in the TO-detection for "bad" fits increases
towards high metallicities, as can be seen with the red line in panel D of Fig. 5.13. It is
not surprising to see this effect, because metal-rich stars have more lines in their spectra,
meaning that there are more data-points that are sensitive to the parameters. With more
lines, a "good" fit is more difficult and the χ^2 value becomes larger. In the same way, metal-
poor stars have less lines, which also have smaller equivalent widths. The calculation of the
χ^2 is mainly concentrated in the continuum, from which it is easier to produce a "good"
fit.

On the other side, "intermediate" χ^2 values show a smooth behavior over the [Fe/H]
- T_{eff} diagram in panel B. The TO is well detected and its errors are small in the cho-
sen metallicity range, which is seen with the green line in panel D. This is because the

parameters show a unbiased sample of stars which have clear cut-off at the turn-off. We could see how "bad" fits are biased toward cold and metal-rich stars. In a similar way, "good" fittings are slightly biased toward more metal-poor and hot stars. In any case, for "good" fits the turn-off can be detected properly for each metallicity and the large scatter introduces a slightly larger error in the TO-detection, as indicated with the blue line in Fig. 5.13D.

This effect in the temperature biased due to χ^2 values was also noted by Allende Prieto et al. (2006), where they found that late-G and early-K stars can be fitted worse than warmer spectral types. They explained this effect by an increased importance of the metal-line opacity, which is affected by poor and missing atomic data.

As a final result of this test, we find an agreement between the different χ^2 classifications in the determination of the MSTO. Although we found biases in the distribution of the parameters when using different fitting quality, the value of the TO as a function of metallicity did not change. We do not need to select by fitting quality our sample for the age determination in Chap. 6.

Quantity dependency

The TO-detection is very dependent on the number of stars of the population. For stars located in the blue side of the main stellar locus of Fig. 5.7, we found that the larger the number of them, the smaller become the errors in the TO-detection. This is shown in Fig. 5.14, where the curves represent different amounts of randomly selected stars from the *G blue* sample. The number of stars varies from approximately 1,000 to 100,000. We have plotted in the upper panel the value of the MSTO as a function of metallicity, while in the lower panel the errors obtained with bootstrapping.

For this sample, the TO-value does not dependent on the amount of stars used in the sample, but there is a dependency in the accuracies obtained. For the smallest sample the errors in the detection have the largest value.

It is important to remark that not necessarily the largest sample is the best one to estimate the turn-off. The value of the TO is more accurate, although the accuracies do not increase sufficiently when the sample is too large. The mean error in the metallicity range of [-3, -1.3] for the 100,000 sample is 46 K while for the 70,000 is 49K. For the 40,000 the mean error increases to an average of 68 K and for the 15,000 one the mean error is 84. All samples yield a lower mean error when considering the accuracies of the spectroscopic temperatures, which are of 130 K (see Chap. 3). However, we will use the 100,000 stellar sample for the age-determination in next chapter, because we want to have a turn-off temperature as accurate as possible.

5.5   Summary and Conclusions

In this chapter we have studied the detection of the turn-off for metal-poor field stars from the SDSS catalog. We used two different techniques to detect the turn-off temperature.
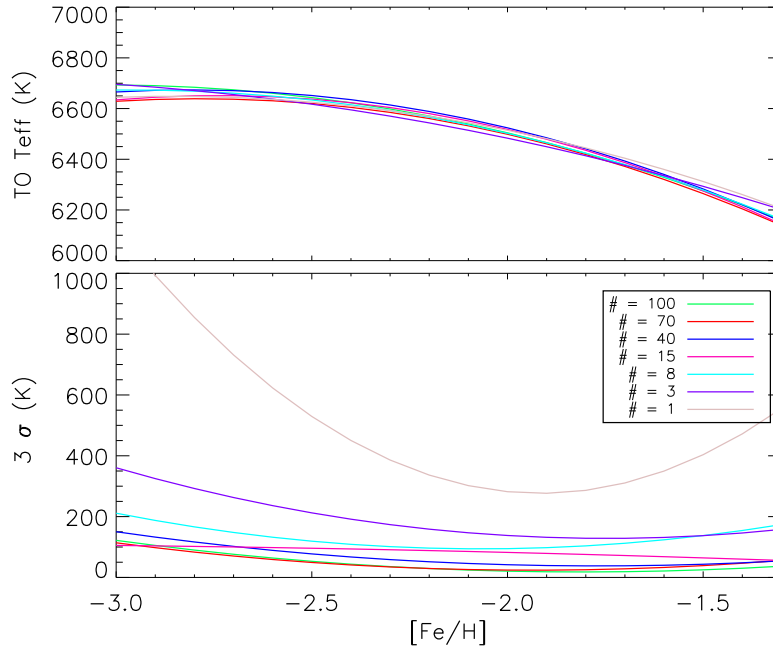
Figure 5.14: Upper panel: TO-detection for samples with different number of stars. Lower panel: the bootstrap error in the TO-detection for each sample. The color lines correspond to different sizes used for the detection, with the number of stars ($\times 1000$) indicated in the legend.

For both of them we selected stars that share a certain metallicity value and created a histogram of the temperature distribution. The first technique consisted in performing a cubic polynomial fit to the edge in the temperature distribution. The second one was to use a standard image-processing edge-detection called Sobel Kernel. We compared the results obtained with both methods and found a good agreement between them.

In order to find the main-sequence turn-off for the Milky Way halo, we performed several tests selecting different samples of the SEGUE catalog. We detected the turn-off using the Sobel Kernel because it turned out to be more robust than the Cubic Fit technique. To study the distributions of the samples in temperature and metallicity, we created [Fe/H] - $T_{\rm eff}$ diagrams of each sample, which helped to understand the behavior of the MSTO detection.

Using four different target selections from color-color diagrams, we saw the importance of considering all stars from the main stellar locus of the color-color diagram, some introducing contamination with blue horizontal branch stars. At different Galactic latitudes we found that for [Fe/H] < -1.2 the TO as a function of metallicity is robust, even when the contamination of metal-rich disk stars is important at lower latitudes. Tests concerning the quality of data were also made. We selected stars with "bad", "intermediate" and "good" metallicity and temperature estimates as well as stars with "bad", "intermediate" and "good" χ^2 fitting values. We also detected the turn-off using samples of different sizes

and we showed that the major dependency of the TO-detection is the quantity of stars rather than the quality.

After performing all these tests we can ensure that our TO-detection is not biased by quality of parameter estimation or target selection. The SDSS/SEGUE field halo stars show thus a robust main-sequence turn-off. The final values of the MSTO temperature as a function of metallicity, including the errors, are listed in Appendix C.

Chapter 6

Age determination

We estimated the age for the halo population by looking at the isochrones that have the same turn-off temperature than this population. We found that the ages can differ up to 4 Gyrs if the stellar evolutionary models take atomic diffusion into account or not. These results are consistent with the literature, where non-diffusive isochrones yield ages of 14-16 Gyr while diffusive ones yield ages of 11-12 Gyr for the Galactic inner halo. Considering the current debate about the efficiency in which atomic diffusion acts in stellar interiors, our results provide a strong argument against canonical isochrones for the age determination of the metal-poor field halo stars.

The age as a function of metallicity was used to show that the halo field has a dominant coeval population connected with the inner halo. We discussed the probable formation scenario, namely that these stars were formed rapidly during the collapse of the Galaxy. In addition, we compared our [Fe/H] - T_{eff} diagram with that of Schuster et al. (2006), which demonstrated the consistency of our results.

6.1   Historic prelude and motivation

The sequence of works called "$uvby - \beta$ photometry of high-velocity and metal-poor stars" of W. Schuster, P. Nissen and collaborators consists of the analysis of a sample of halo field stars (Schuster & Nissen 1988a). They estimate the metallicities of the stars using $uvby - \beta$ photometric calibrations, as explained in Schuster & Nissen (1988b). The third paper of this series (Schuster & Nissen 1989) was the first one to obtain ages for these stars. They placed their metallicities and colors in a $[\text{Fe/H}] - (b-y)$ diagram, where they could identify the turn-off by looking at the bluest stars at different metallicity values. Using the turn-off color and metallicity of isochrones from Vandenberg & Bell (1985), they found that the minimum age for halo stars was about 18 Gyrs. Although these ages were in conflict with the age of the Universe – which was constrained to be 12-14 Gyrs (Rowan-Robinson 1985) – they agreed well with the ages of globular clusters obtained at that time (Vandenberg 1983).

Unavane et al. (1996) used 417 stars from a sample of halo stars of Carney et al. (1994) and placed their metallicities and $(B-V)$ colors in a similar diagram. The sample showed a clear turn-off color as a function of $[\text{Fe/H}]$, which was used to superpose isochrones of Yale (Green et al. 1987). They found that isochrones with more than 15 Gyr represented the turn-off adequately, which defined a dominant population. In their $[\text{Fe/H}]$ - T_{eff} diagram they could also observe a number of halo stars at higher metallicities bluer than the turn-off color. These stars were interpreted as a younger population than the majority of the halo stars, probably the result of accretion of dwarf neighboring galaxies.

Also in 1996, paper VIII of the $uvby - \beta$ photometry series (Schuster et al. 1996) published a new $[\text{Fe/H}] - (b-y)$ diagram, this time including very metal-poor stars taken from the HK survey (Beers et al. 1992), which were also analyzed with $uvby - \beta$ photometry. From the metallicity range of $[\text{Fe/H}] = [-3.8, -1.1]$ it was possible to see a clear cut-off color as a function of metallicity. Using the turn-off color of the Bergbusch & Vandenberg (1992) isochrones they suggested that the youngest halo stars were coeval to within 1-2 Gyrs, being 18 Gyr old. This age was consistent with the previous results of this series (Marquez & Schuster 1994), but not with the mean age of the globular clusters (~ 14 Gyr, Sandage 1993) at that time. Marquez & Schuster (1994) discussed that this inconsistency could be due to the method employed to determine ages, or to the fact that their sample of field stars was indeed older. The field stars participated in the initial, rapid collapse of the Galaxy, while many of the surviving GC's were formed during a later accretion process.

In a study of the Milky Way using SDSS/DR3 data, Allende Prieto et al. (2006) presented a similar $[\text{Fe/H}]$ - T_{eff} diagram. The spectroscopic metallicities of a sample of F-G dwarfs were plotted against the $(g-r)$ colors. The turn-off color as a function of metallicity was used to superpose the TO isochrones of Girardi et al. (2004), who transformed them to Sloan colors. Allende Prieto et al. (2006) found that for $[\text{Fe/H}] < -1$ the star formation in the halo ceased between 10 and 12 Gyr ago. They also argued that some members of the thick disk (for $[\text{Fe/H}] > -1$) are 8 Gyr old.

Finally, in paper IX of the $uvby - \beta$ photometry series, Schuster et al. (2006) studied a new $[\text{Fe/H}] - (b-y)$ diagram. The authors write "... similar to that of Schuster et al. (1996),

but with more stars and better, recent isochrones, those of Bergbusch & VandenBerg (2001)". The new isochrones yield ages of 13 Gyr, which is in agreement with the updated age of the Universe (13.7 Gyr; Bennett et al. 2003). Based on these new resulting ages for the halo they suggested that the formation of the most metal-poor stars of the Galaxy was 2-3 Gyrs after the collapse of the Galaxy. Moreover, they could see in their $[Fe/H] - (b - y)$ diagram bluer stars than the turn-off color at $-1.5 \lesssim [Fe/H] \lesssim -0.9$. As discussed also in Preston et al. (1994), Unavane et al. (1996) and the papers of the $uvby - \beta$ photometry series, these blue metal-poor stars could be related with a younger accreted population.

Why are the absolute ages so different between 1996 and 2006?

Although these studies give quite different absolute ages over the years, they are consistent with each other, in the sense that the halo has a dominant old population. But why are the absolute ages so different? The difference in age leads to an extreme fundamental problem that must be considered: In 1996 the resulting ages were in conflict with the age of the Universe and in 2006 these ages were not in conflict anymore. The authors have been using better data, from where the turn-off can be better identified. Empirical calibrations to obtain metallicities have also been getting more accurate, as well as the observations itself, especially the extinction correction. Nevertheless, that does not explain a decrease more than 4 Gyr of the isochrones representing the halo turn-off stars.

Stellar evolutionary models contribute significantly to this story. They may have the greatest affect in the age-reduction obtained in the studies between 1996 and 2006. None of these studies has dedicated a discussion to the current status of stellar evolutionary models and how they affect the absolute ages of the turn-off halo stars. We will show in this chapter that an important ingredient in the age-reduction obtained in the present [Fe/H] - T_{eff} diagrams is the settling of helium in the interior of stars, which is also called *atomic diffusion*. Salaris & Weiss (2001b) suggested that the absolute ages can be reduced up to 4 Gyr when using the turn-off color for the age determination of field stars. Weiss et al. (2005) then proposed that SDSS survey contains enough halo field stars to quantify this age difference. In the first part of this thesis (Chap. 2 - 4 and Jofré et al. 2010), we analyzed the SDSS stellar spectra in order to obtain metallicities and temperatures of the halo field subdwarfs. In this second part of the thesis, we aim to determine the age provided by the SDSS turn-off stars, being especially careful with the atomic diffusion parameter.

In Sect. 6.2 we explain the effect of atomic diffusion in stellar evolutionary models and we discus the results obtained for the ages using our [Fe/H] - T_{eff} diagrams in Sect. 6.3. We continue with a discussion of the Galaxy evolution in Sect. 6.4 and end this chapter with a summary and conclusions in Sect. 6.5

6.2   Atomic Diffusion

It has long been recognized that atomic diffusion, which causes heavier elements to sink relatively to hydrogen, may occur in the radiative regions of a star (Noerdlinger & Arigo 1980; Proffitt & Vandenberg 1991; Christensen-Dalsgaard et al. 1993; Weiss et al. 2000; Chaboyer et al. 2001). On the main-sequence, low-mass metal-poor stars have radiative cores and thin convective envelopes. Diffusion can lead to large depletions of elements heavier than hydrogen in their surface, producing a change in the effective temperature and abundance. In contrast, the diffusion timescale in the core of stars does not vary widely, resulting in a modest effect of the predicted luminosities.

This gravitational settling leads to a concentration of the heavy elements towards the center of the star. For this process to be efficient, the medium has to be undisturbed, such that large motions do not prevent the settling (Chaboyer et al. 2001). This is why the most suited places to act for diffusion are in radiative regions. Diffusion is very slow, with timescales of the order of 10^9 yrs (Salaris et al. 2000) meaning that the only evolutionary phase where diffusion can be efficient is during the main sequence. This happens in particular for metal-poor stars, because they have thin convective envelopes (Kippenhahn & Weigert 1990; Cassisi et al. 1998).

For the Sun, the insertion of helium and metal diffusion in the models has significantly improved the agreement with the observations (Christensen-Dalsgaard et al. 1993). Only in the region immediately below the convective envelope the theoretical models deviate significantly from the seismic Sun. The reason might be that diffusion does not operate as efficiently as calculated in that region, and some additional physical process partially inhibits it (Brun et al. 1999). Due to helium settling, the helium content in the surface progressively decrease during the main-sequence phase as it sinks below the convective envelope. Hydrogen is thus placed out of the center towards the surface. The less hydrogen to burn in the core, the faster is the evolution of the star in the main-sequence. Hence, the consideration of atomic diffusion in the stellar evolutionary models has consequences in the age determination of metal-poor stars (Chaboyer et al. 1992a,b; Salaris et al. 2000).

There is still no census of how efficiently diffusion occurs in the stellar interiors. Observations of the Spite Li-plateau in metal-poor stars (Spite & Spite 1982), suggest that diffusion is inhibited near the surface of these objects, although Salaris & Weiss (2001a) pointed out that after accounting for the uncertainties and biases in the observations, models with diffusion still agree well with the Spite Li-plateau observations. From the observational point of view, diffusion decreases the surface metallicity such that a star presently observed with a given metallicity has started its evolution with higher metallicity. Gratton et al. (2001) did an abundance analysis at the turn-off and giants in a globular cluster and did not find a difference in [Fe/H], which they claimed as diffusion being completely inhibited by internal mechanisms in these stars. Recently, Korn et al. (2006) and Lind et al. (2008) did a similar analysis of the same cluster and found a difference in chemical abundances in the surface of these stars, which is contradictory with the conclusions of Gratton et al. (2001). The differences were, however, smaller than theoretical predictions with fully efficient diffusion. These results are evidence of some internal

mechanisms in the stars that counteract diffusion. From the theoretical point of view, the effect of heavy-element diffusion in metal-poor stars is controversial, since the theoretical results also depend on the formalism employed to describe it. Moreover, it is not clear which mechanisms counteract diffusion in the surface layers. Some popular theories are mixing induced by rotation (e.g. Pinsonneault et al. 2002) and radiative acceleration (e.g. Morel & Thévenin 2002).

Concerning the absolute ages of globular clusters, there are age indicators that do not depend on diffusion (Chaboyer et al. 1992a; Meissner & Weiss 2006) and therefore when studying the early Galaxy with globular clusters, the debate mentioned above is not so problematic. When considering halo field stars, on the other side, the effect of diffusion on absolute ages remains to be quantified (Korn 2008).

6.2.1   Diffusion with GARSTEC models

Helium diffusion is responsible for the major change in effective temperature at the turn-off. Diffusion of other heavier elements produce a little additional change to that produced by helium (Weiss et al. 2000; Chaboyer 2007). GARSTEC models consider full diffusion of helium and hydrogen using the diffusion coefficients of Thoul et al. (1994), with no consideration of radiative levitation or rotational mixing.

The influence of diffusion on the isochrone shape in the HR diagram is displayed in Fig. 6.1 for the metal mass fraction corresponding to $Z = 0.0002$. The black lines are the 11 Gyr isochrones with and without diffusion, represented with the solid and the dashed line, respectively. In addition, we have plotted the 8.5 Gyr diffusive isochrone with the red solid line. The effect of a lower effective temperature and brightness for diffusive models during the main sequence can be seen in the 11 Gyr isochrones of Fig. 6.1. This has also been noticed by Proffitt & Vandenberg (1991), Cassisi et al. (1998) and Weiss et al. (2000). The reason for this decrease is that the central settling of helium slightly accelerates the rate of central hydrogen-burning, reaching the turn-off earlier and at lower luminosity than if diffusion does not occur. Weiss & Schlattl (2000) presented the effect of helium diffusion in GARSTEC evolutionary tracks and showed how main-sequence lifetimes get shorter due to the helium diffusion. Therefore, the evolution of a star gets faster during the main-sequence.

When comparing our diffusive and canonical isochrones in Fig. 6.1, we see that they become similar at the red giant branch. The reason is that when the star reaches the red giant branch, most of the helium which was settled in the radiative core is now dredged up due to the growth of the convective envelope.

It is important to mention that the TO-temperatures of isochrones do not quantify the effect of the diffusion properly. Since helium settling accelerates the evolution of a main sequence stars, it reaches the TO earlier when affected by helium settling. This means that a star located at the TO of a canonical isochrone has a larger mass than a TO-star in a diffusive one of the same age. To quantify the effect produced in the temperature due to diffusion, one has to consider stars of the same mass. In addition to what was mentioned
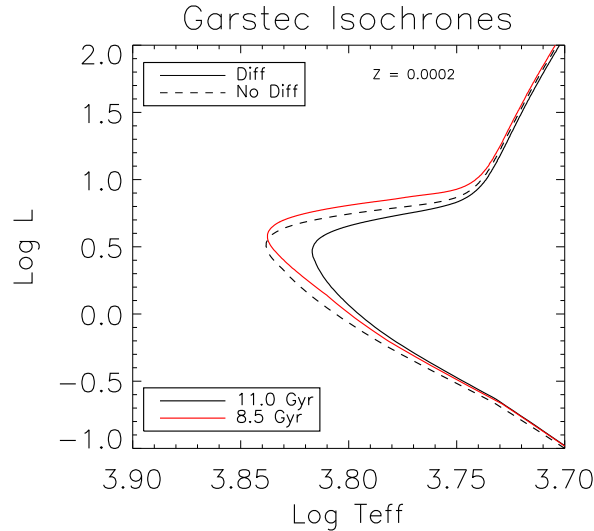
Figure 6.1: Isochrones of 11 Gyr and Z = 0.0002 with and without atomic diffusion represented with continuous and dashed lines, respectively. The turn-off of the non-diffusive isochrone changes significantly. A diffusive isochrone with the same the metal fraction but with an age of 8.5 Gyr is plotted in red, which matches the turn-off of the 11 Gyr standard one.

above, we recall that the size of the convective envelope increases with decreasing mass. A TO-star in a young isochrone will not be affected less by diffusion than an older one at the TO, because the younger TO-star has larger mass than the older TO-one. Using GARSTEC (Weiss & Schlattl 2008) stellar evolutionary tracks we find that a $0.7 M_\odot$ star reaches the turn-off at 18 Gyr when it is affected by diffusion. The same $0.7 M_\odot$ star is still on the main-sequence if diffusion does not occur and their effective temperatures differ by 186 K. A star with a larger mass of $0.83 M_\odot$ reaches the turn-off earlier, i.e. in 10 Gyr, when diffusion occurs. The difference in temperature between this star and one with the same age when it is not affected by helium settling is 266 K. Although for the second example the stars are younger, their larger masses –i.e. thinner convective envelopes– result in a larger settling of helium. In general, older ages for globular clusters imply that the effects of atomic diffusion are smaller (Chaboyer et al. 2001).

Let us concentrate again on the TO-temperature and examine Fig. 6.1. We have plotted a 8.5 Gyr diffusive isochrone, from which we can see that it has the same TO-temperature as the 11 Gyr canonical one. This issue has extremely important consequences in the determination of MSTO ages when the luminosity and mass are not known. Diffusion produces significant differences for ages determined from the main-sequence turn-off temperatures.

6.2.2   Using GARSTEC isochrones

The MPA databases contain GARSTEC isochrones with metallicity Z indicated in Table 6.1. In each metallicity directory, evolutionary tracks with and without diffusion are

Table 6.1: MPA GARSTEC isochrones. Z, Y, X: metal, helium and hydrogen mass fraction, respectively. Final metallicity given by [Fe/H] and [M/H] transformed from Z using Eq. (6.6) for $\alpha-$enhanced stars

Directory	Z	Y	X	[Fe/H]	[M/H]
z00	2×10^{-5}	0.2450	0.7549	-3.26	-2.97
z01	1×10^{-4}	0.2453	0.7546	-2.56	-2.27
z02	2×10^{-4}	0.2455	0.7543	-2.26	-1.97
z03	3×10^{-4}	0.2458	0.7539	-2.08	-1.79
z06	6×10^{-4}	0.2465	0.7529	-1.78	-1.49
z10	1×10^{-3}	0.2475	0.7515	-1.56	-1.27
z20	2×10^{-3}	0.2500	0.7480	-1.25	-0.96
z30	3×10^{-3}	0.2525	0.7445	-1.07	-0.78
z60	6×10^{-3}	0.2600	0.7340	-0.77	-0.48
z10	1×10^{-2}	0.2700	0.7200	-0.54	-0.25

stored. For each model, isochrones of 4-18 Gyr are available. The evolutionary models were created using a mixing-length parameter of $\alpha_{MLT} = 1.71$ and $\alpha-$enhanced metal composition of $[\alpha/\text{Fe}] = +0.3$ dex. For more details about the models see Weiss & Schlattl (2000), Meissner & Weiss (2006) and Weiss & Schlattl (2008). The most metal-poor isochrone ($Z = 2 \times 10^{-5}$) was kindly computed by Z. Magic (priv. comm.) for the purpose of this work. Note in Table 6.1 that there are three different definitions of metal abundance, which are labeled in the second, fifth and sixth column as Z, [Fe/H] and [M/Fe], respectively. The relation of these definitions is found in the following.

Z- [Fe/H] relation

To transform the metal mass fraction used in stellar evolutionary models into metallicity inferred from stellar atmospheres, we consider the definition of metal abundance

$$[\text{M/H}] = \log\left(\frac{\text{N}_\text{M}}{\text{N}_\text{H}}\right) - \log\left(\frac{\text{N}_\text{M}}{\text{N}_\text{H}}\right)_\odot, \tag{6.1}$$

where $\text{N}_\text{M}, \text{N}_\text{H}$ are the number of atoms of metals and hydrogen in the star, respectively. This definition can also be written in terms of mass fraction, i.e. the mass fraction of hydrogen can be expressed as $\text{X}_\text{H} = \frac{\text{N}_\text{H}\rho\text{N}_\text{A}}{\text{A}_\text{j}}$, where ρ is the density mass and N_A the Avogadro number. The same expression is valid for helium and the metals and we obtain the three quantities $\text{X}_\text{M} = Z$, $\text{X}_\text{H} = X$ and $\text{X}_\text{He} = Y$ which satisfy the relation

$$X + Y + Z = 1. \tag{6.2}$$

The vast majority of stars consist mainly of hydrogen with about 10-15% of helium (by number of atoms and ions) and only few atoms of metals. Among the metals, the most abundant are C, N, O and Ne, followed by Fe, Si, Al and Mg (Böhm-Vitense 1989). These

elements are much heavier than hydrogen and therefore contribute with mass fraction Z in Eq. (6.2). To determine the abundance of elements in stellar atmospheres, spectroscopists identify the absorption lines corresponding to each element. Since iron lines are of the most abundant one in a spectrum, [Fe/H] is usually referred to as the metallicity of the star. A consequent definition of metallicity is [Fe/H] = f_α + [M/H], where f_α scales the observed iron abundance to the global metallicity of a star.

The α elements (O, Mg, Si, Ca, S and Ti) are produced during the explosion of massive stars as a Supernova Type II, which occur a few millions years after their formation. Iron-peak elements, on the other side, are mostly produced by Type Ia supernovae. These explosions take place typically in a longer timescale than Type II ones. Today, Type Ia and Type II explosions enrich the interstellar medium such that the iron-peak and α elements scale equally. This mixture of elements is referred to as the solar-mixed composition, where [M/H] = [Fe/H], and therefore $f_\alpha = 0$. The majority of the local halo stars have an over-abundance of α elements in their atmosphere, where typically [α/Fe] $\sim 0.3 - 0.4$ dex (e.g. Helmi 2008, and references therein). Such chemical configuration may be obtained when the interstellar medium was enriched by Supernovae Type II, but not significantly by Type Ia supernovae. These stars are also called population II stars and have [M/H] > [Fe/H]. We consider for this study the value of $f_\alpha = -0.29$ taken from Meissner & Weiss (2006).

In GARSTEC models, the helium mass fraction is related with the metal mass fraction by

$$Y = Y_p + \frac{\Delta Y}{\Delta Z} Z, \tag{6.3}$$

where $Y_p = 0.245$ is the primordial helium mass fraction and $\frac{\Delta Y}{\Delta Z} = 2.5$ (Meissner & Weiss 2006). For the Sun we consider the present value of

$$\left(\frac{Z}{X} \right)_\odot = 0.0245 \tag{6.4}$$

taken from Grevesse & Noels (1993), which has decreased over the solar lifetime from a initial value of $Z/X_\odot = 0.028$ due to diffusion. Eq. (6.1) can be tranformed to

$$\left(\frac{Z}{X} \right) = 0.0245 * 10^{[M/H]} \equiv A. \tag{6.5}$$

For a given metal abundance [M/H] obtained from spectral analysis, using Eq. (6.5), Eq. (6.3) and the numeric values given above for the sun and primordial helium, we know which is the corresponding metal mass fraction by employing the relation:

$$Z = \frac{0.755 \cdot A}{1. + 3.5 \cdot A}. \tag{6.6}$$

When using this relation to work with our field stars and GARSTEC models, it is important to consider the following points:

- Our estimates of metallicities were obtained by the spectral analysis described in Chap. 2 and Chap. 3, which were based on Kurucz stellar atmosphere models (Kurucz 1992). These models adapt the solar scale of Grevesse & Sauval (1998) , i.e. $(Z/X)_\odot = 0.023$. It has a difference of ~ 0.015 dex with the solar abundance adopted by the isochrones.

- A similar effect must be considered due to diffusion. Although GARSTEC stellar evolution models do not consider metal diffusion (i.e. the metal fraction Z is constant), [M/H] changes indirectly. As helium sinks from the surface, hydrogen must increase in the surface layers to maintain the relation of Eq. (6.2). This produces a change in the relative abundance Z/H and therefore in the metallicity. A GARSTEC model with $0.82 M_\odot$ with $Z = 2 \times 10^{-4}$ can have a decrease in the surface [M/H] of 0.09 dex due to helium settling during the main-sequence (Alves-Cruz, priv. comm.).

- Globular cluster metallicities are usually determined from red giants, in which the original surface metallicity has been restored by convection. The metallicity obtained for our field MSTO stars, on the other hand, are determined directly from the spectra, meaning that the [Fe/H] value obtained has decreased with respect to its initial value due to diffusion. Korn et al. (2006) and Lind et al. (2008) observed atomic diffusion in population II stars by comparing metallicities of TO and giants of the globular cluster NGC 6397. They found a difference in metallicity of 0.16 dex produced by this effect.

In general, one should take these effects into account when using GARSTEC isochrones to relate the estimated metallicities. For our work, the errors in the metallicity estimates from SDSS spectra are of the order of 0.25 dex, which means that these effects can be neglected.

6.3 [Fe/H] - T_{eff} diagram for the age determination

We have used a [Fe/H] - T_{eff} diagram to superpose turn-off isochrones with different ages. Our stellar sample corresponds to the *G blue*, with color constraint indicated in Table 5.1. Metallicities and temperatures of the stars were estimated using MAχ (Chap. 2) for SDSS spectra as described in Chap. 3 and Jofré et al. (2010). The final value obtained for the main-sequence turn-off temperature as a function of metallicity was listed in Appendix C, which we consider in this section to the determination of ages for the turn-off field halo stars. In Sect. 6.3.1 we use the cut-off traced by the MSTO to quantify the difference of absolute ages produced by the inclusion of diffusion in the isochrones. In Sect. 6.3.2 we present the age as a function of [Fe/H] for the MSTO given in Appendix C.

6.3.1 Age reduction

Following the method employed by Schuster et al. (2006, and references therein) we found the isochrones that superpose the cut-off traced by the MSTO. We considered isochrones

Figure 6.2: [Fe/H] - T_{eff} diagram of the *Gblue* sample along with turn-off temperature as a function of metallicity of GARSTEC isochrones. Upper panel: canonical isochrones of 11, 14, 16 Gyr correspond to the MSTO of the field stars. Lower panel: diffusive isochrones of 9, 11,12 Gyr correspond to the MSTO of the field

with and without diffusion. The [Fe/H] - T_{eff} diagram and isochrones are illustrated in Fig. 6.2. The black line illustrates the MSTO of Appendix C, with the dashed line corresponding to the errors.

The first result is the need for different isochrones that trace field MSTO when considering diffusion or not. We can see in the upper panel of Fig. 6.2 that for the canonical isochrones, the 14-16 Gyr ones agree well with the line traced by the turn-off. When using diffusive isochrones, as seen in the lower panel of Fig. 6.2, the isochrones which agree with the MSTO are the 11-12 Gyr. Younger ages are found for the metal-rich domain when considering the errors in the MSTO. The mean age reduction only due to diffusion for the field stars is about 4 Gyr. The results obtained for ages from the upper panel of Fig. 6.2 agree better with those of Schuster & Nissen (1989), Schuster et al. (1996) and Unavane et al. (1996), while the results obtained with the isochrones at the lower panel are

in better agreement with those of Schuster et al. (2006) and Allende Prieto et al. (2006). This is a strong argument that the most influencial improvement during the years between 1996 and 2006 is the inclusion of atomic diffusion in stellar evolutionary models. A small age reduction has also been produced by the consideration of $\alpha-$enhanced chemical composition in the isochrones, which have higher temperatures with respect to the solar-scale models (Salasnich et al. 2000; Cassisi et al. 2004)
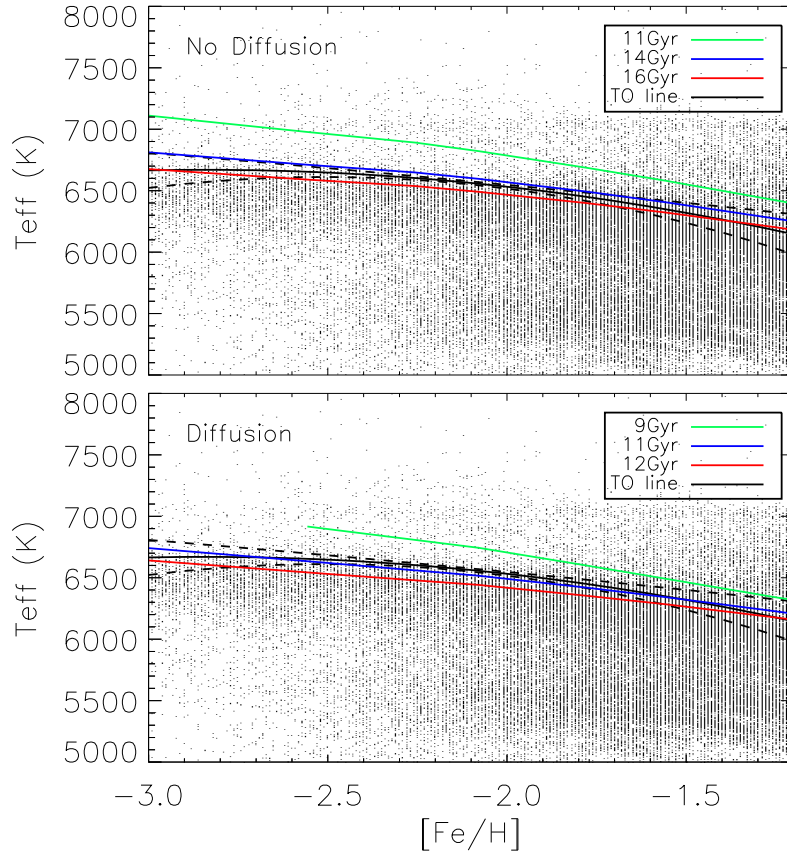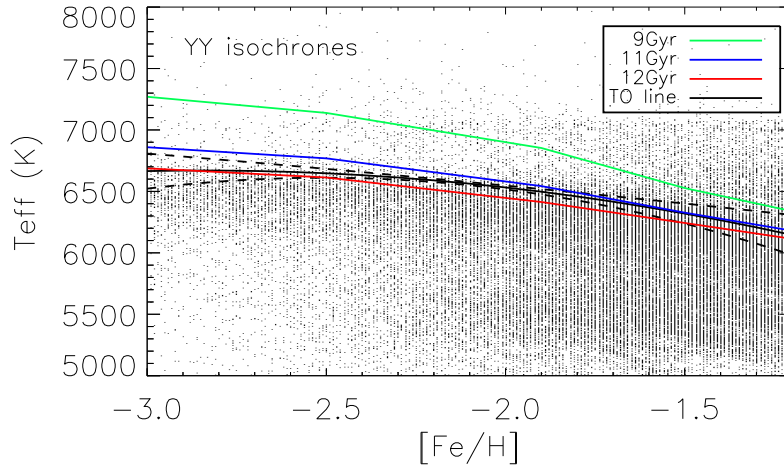

Figure 6.3: [Fe/H] - T_{eff} diagram of the *Gblue* sample along with turn-off temperature as a function of metallicity of Y^2 isochrones. 9, 11,12 Gyr correspond to the MSTO of the field

Comparison with Yale Isochrones

As a comparison with the results obtained with GARSTEC, we plotted the turn-off Y^2 isochrones as a function of metallicity (Yonsei-Yale, Demarque et al. 2004) along our [Fe/H] - T_{eff} diagram . They agree with the MSTO line for the ages of 9-12 Gyr as in the case of diffusive GARSTEC isochrones illustrated in the lower panel of Fig. 6.2. This is because the version used for the creation of the Y^2 considers atomic diffusion, which is treated with the coefficients of Thoul et al. (1994) as GARSTEC does. Note that although the range of isochrones employed here agree with that employed for the lower panel of Fig. 6.2, we observe that their turn-off temperature as a function of metallicity is slightly different. For example, at [Fe/H] $= -2.5$, the GARSTEC isochrone with turn-off of the field MSTO corresponds to 11 Gyr. The 11 Gyr Y^2 isochrone of [Fe/H] $= -2.5$ has a larger TO-temperature than the field. In fact, the Y^2 isochrone that reproduces the field MSTO of the field corresponds 12 Gyr.

We have compared the 11 Gyr isochrones of Y^2 and GARSTEC in the upper panel of Fig. 6.4. The three panels indicate isochrones of different Z, and we can see how the turn-off temperature is different for the very metal-poor isochrones. The dotted lines illustrate diffusive isochrones (red) and canonical ones (black), while the blue dashed line illustrates

Y^2 models. GARSTEC diffusive isochrones yield a turn-off temperature lower than Y^2. Note that Y^2 stellar evolutionary models employ an initial helium mass fraction of $Y = 0.23$, which is 0.015 lower than the GARSTEC one of $Y = 0.245$. Different values of initial helium can significantly affect the evolution of a star in the main-sequence (Salaris et al. 2000; Casagrande et al. 2007). Studies of multiple main-sequences in globular clusters such as ω Centauri suggest that to produce the bluest main-sequence, a larger helium fraction is required (Norris 2004; Lee et al. 2005). It is therefore intriguing that GARSTEC diffusive
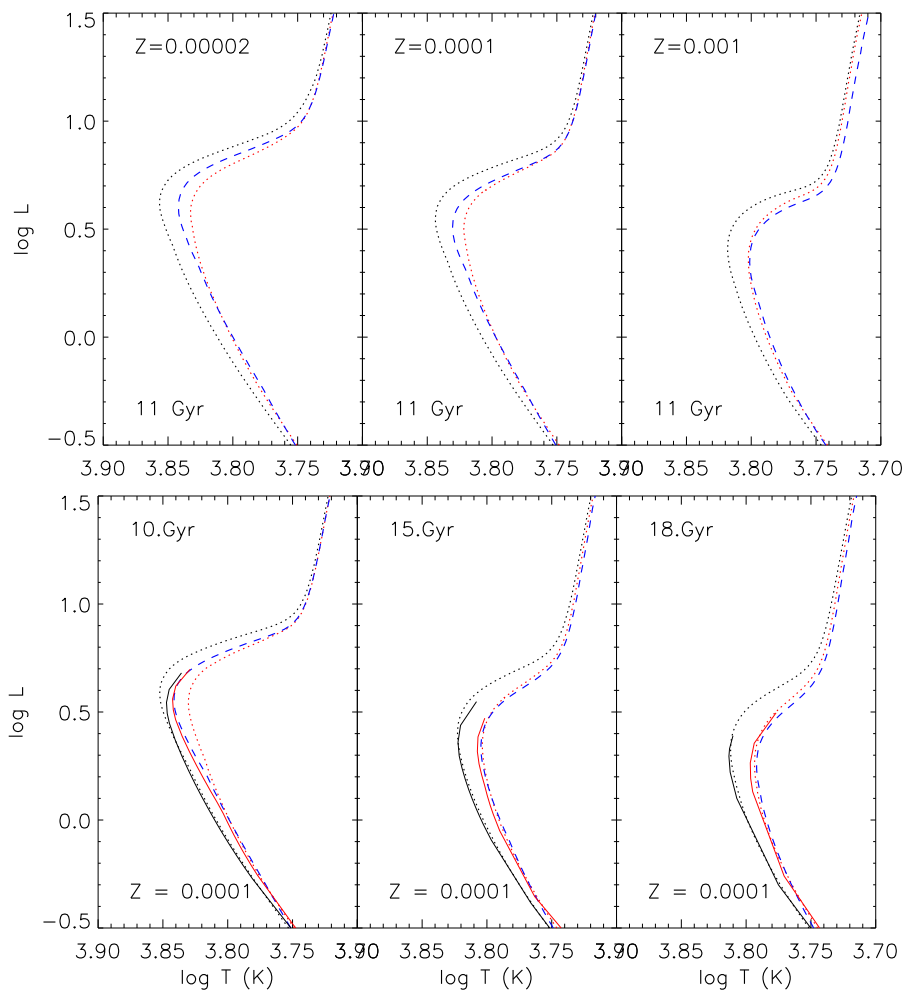
Figure 6.4: Comparison between GARSTEC and Y^2 isochrones. Dotted lines represent GARSTEC isochrones and blue dashed lines the Y^2 isochrones. Solid lines represent the new Y^2 isochrones computed by Kim & Demarque (priv. comm. 2010). Diffusion and canonical models are in red and black, respectively. Upper panel: Comparison of 11 Gyr isochrones for three different metal fraction values. Lower panel: Comparison of 10 (left), 15 (middle) and 18 (right) Gyr isochrones with $Z = 0.0001$.

isochrones, which have larger initial helium abundances, lie on the red side of the Y^2 ones.

In any case, to quantify the absolute age-reduction due to diffusion we need non-diffusive Y^2 isochrones. Y. C. Kim and P. Demarque kindly accepted to compute stellar evolutionary tracks with and without atomic diffusion based on an updated version of the YREC code (Demarque et al. 2008). This new version introduces only small differences to the Y^2 isochrones. We obtained the mass, effective temperature and luminosity of stars at 10, 15 and 18 Gyrs of Z = 0.0001 (Kim & Demarque, priv. comm. 2010), which we used to build the isochrones. These isochrones (hereafter Y^2_{new}) are illustrated in the lower panels of Fig. 6.4 with solid lines. Again red corresponds to the diffusive and black to canonical models. In addition, we plotted the old Y^2 ones with the blue dashed line. We can see that the old Y^2 and the diffusive Y^2_{new} agree. Dotted lines are GARSTEC isochrones as in the upper panel.

In each lower panel of Fig. 6.4 we observe how the diffusive Y^2_{new} isochrones have a colder turn-off temperature than the canonical ones, which is also seen for the GARSTEC ones. However, the absolute difference in the TO-temperature between diffusive and canonical isochrones is clearly different for both models. Y^2_{new} models have for the 10 Gyr isochrones a small absolute difference in TO-temperature of 75 K while GARSTEC have one of 353 K. For the 18 Gyr isochrone the Y^2_{new} models have a TO-temperature difference of 242 K while GARSTEC ones of 270 K. Chaboyer et al. (2001) has discussed that the effect of diffusion in older globular clusters is smaller than in younger ones due to a difference in stellar mass. GARSTEC isochrones are in agreement with this statement while Y^2_{new} are not. Note also that Y^2_{new} canonical 10 Gyr isochrone has a luminosity at the TO of $\log(L/L_\odot) = 0.54$ while the diffusive one of $\log(L/L_\odot) = 0.56$. We saw in Fig. 6.1 how the TO-luminosity decreases when helium settling is considered, which also has been largely accepted in the literature (Proffitt & Vandenberg 1991; Chaboyer et al. 1992a; Cassisi et al. 1998; Weiss et al. 2000).

As a conclusion, each stellar evolutionary model is different, driving thus different TO-temperatures for the isochrones. This means that we can neither give an absolute age for the MSTO of the halo, nor quantify the absolute age-reduction in these stars, because both quantities are very dependent on the models employed. In particular, we note that GARSTEC isochrones show a consistent behavior (in terms of atomic diffusion) with the literature, and therefore we accept an age-reduction in metal-poor turn-off halo field stars of ~ 4 Gyr as a trustworthy value. This result is also consistent with the age difference found between the works of Schuster et al. (1996) and Unavane et al. (1996) – who used canonical stellar evolutionary models – and the works of Allende Prieto et al. (2006) and Schuster et al. (2006) – who used diffusive stellar evolutionary models.

6.3.2 The age as a function of metallicity

To determine the ages of the field stars, we have looked for the isochrone in the MPA databases with metallicity and TO-temperature corresponding to the TO-value listed in Appendix C. We did this for the diffusive and the canonical isochrones, where the ages of the TO-stars as a function of metallicity are illustrated in the upper panel of Fig. 6.5. The errors considered here are only those connected with the errors obtained for the TO-

detection in Chap. 5, which are indicated in Appendix C as σ_{TO}. In addition to the age determined for the values of the TO-temperature listed in Appendix C as $T_{\text{eff,TO}}$, we determined the ages for the values with $T_{\text{eff,TO}} + \sigma_{\text{TO}}$ and $T_{\text{eff,TO}} - \sigma_{\text{TO}}$.
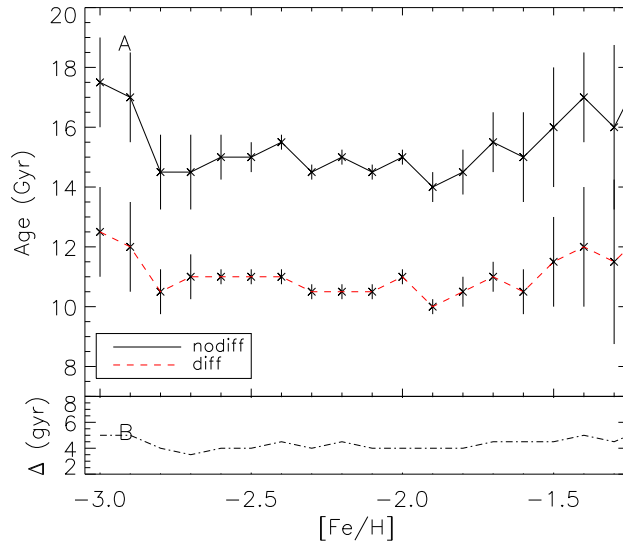
Figure 6.5: Upper panel: The age as a function of metallicity. The red line corresponds to the ages obtained using diffusive GARSTEC isochrones and the black line to the canonical ones. Lower panel: absolute difference between both ages.

In the entire metallicity domain, the ages obtained with canonical models are larger than those obtained with diffusion, which was also observed in Fig. 6.2. The age-reduction due to diffusion also happens for ages of globular clusters, especially those age-indicators that depend strongly on the turn-off color (Chaboyer et al. 1992a). The difference between ages obtained with and without diffusion as a function of metallicity is displayed in the lower panel of Fig. 6.2, where the mean difference is of about 4 Gyrs. We are aware that this value can vary if we use other stellar evolutionary models, as we saw in the comparison with the Y^2_{new} isochrones. In addition, the upper panel of Fig. 6.5 shows that when considering the errors, no real trend is found for age as a function of metallicity. The largest ages are found at the metal-poor and metal-rich borders of our sample, while the youngest ages are seen for the metallicity values in between. The errors become also larger for the borders, which is also related with the larger errors in the detection of the MSTO. Table D in the Appendix lists the age as a function of metallicity obtained using diffusive and canonical isochrones, including the errors. We mention here that other sources of systematic errors should be taken into account. The internal uncertainties in the evolution models, as well as the metallicity uncertainties in the determination of the turn-off increase the error bars in Fig. 6.5. We do not find a trend (or gradient) of age and metallicity.

This implies that there is a dominant halo population traced by the MSTO cut-off, which is coeval and has a small scatter in age of 1-2 Gyr. A similar result was found by Schuster et al. (2006), who also saw that ages of field stars do not have a significant age-

metallicity relation. In addition, they could see how for [Fe/H] > -1.3 the age-metallicity relation breaks down towards higher ages and error bars grow considerably. They attribute this effect to the lower number of evolved halo stars and perhaps higher contamination with stars of the Galactic thick-disk. We see that our age-metallicity relation changes its mean trend at [Fe/H] ~ -1.6, but the ages are still in the 1-2 Gyr range for the entire metallicity domain.
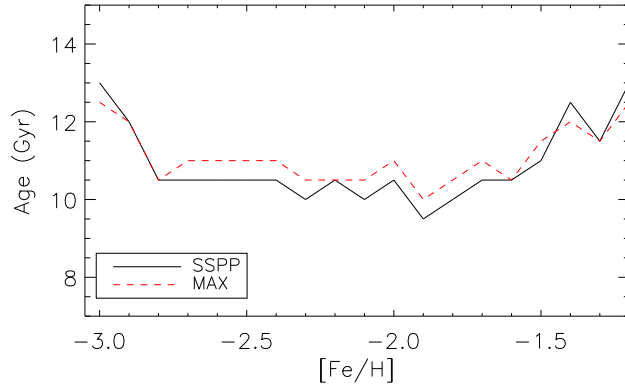
Figure 6.6: Ages for the MSTO temperature as a function of metallicity. Black line indicates the MSTO traced by the stellar sample with SSPP parameters (Lee et al. 2008a) and red line the for the MAχ parameters (Chap. 2). The offset of 0.3 dex between SSPP and MAχ metallicities results in negligible effects in the final age determination.

We saw in Chap. 5 and Fig. 5.6 how the offset of ~ 0.3 dex in metallicity produced between the SSPP and MAχ does not affect the value of the MSTO temperature. As a consistency check, we determined also the ages for the *G blue* sample with the atmosphere parameters of SSPP. The comparison of the results obtained with the diffusive isochrones for SSPP and MAχ is shown in Fig. 6.6, where the black line corresponds to the ages as a function of [Fe/H] for the MSTO determined in the SSPP sample, while the red line is the result for the MAχ sample. Both results agree very well, showing no trend of age as a function of [Fe/H] and small differences of 0.5 Gyrs. This result shows the robustness of the MSTO temperature provided by the dominant halo field population from the SDSS, and the offset found in the breakdown of our age-[Fe/H] relation and the one in Schuster et al. (2006) is not due to the metallicity scale which is adopted.

The question of whether or not an age-metallicity relation exists in the Galactic halo is a longstanding problem. Much more effort has been dedicated to find an age-metallicity relation for the globular clusters than for the field, mainly because the properties of clusters are known with better confidence than for the field stars. The general believe today from globular clusters is that the outer halo of the Galaxy was formed slowly, rather chaotically, with the Galaxy accreting material over several Gyr, as proposed by Searle & Zinn (1978). The inner halo was formed rapidly via a gravitational collapse as proposed by Eggen et al. (1962). An age-metallicity relation for this scenario is expected to have a narrow age spread at low metallicities (representing the rapid collapse of the inner halo) and a broad spread at high metallicities (representing the merging of younger extragalactic systems).

This has been observed for globular clusters (Salaris & Weiss 2002; De Angeli et al. 2005; Dotter et al. 2010), although the limit between narrow and broad spread in ages is at different metallicities. De Angeli et al. (2005) for example, found that clusters [Fe/H] < −1.7 are old and coeval while Salaris & Weiss (2002) found that clusters with [Fe/H] < −1.2 are the old and coeval ones.

It is instructive to discuss the inner and outer halo found for the field stars by Carollo et al. (2007) using SDSS data. They claim that the outer halo is more metal-poor than the inner halo, with the peaks of the metallicity distribution being of -2.2 and -1.6, respectively. The outer halo of Carollo et al. (2007) is additionally related to stars of larger distances, implying an metallicity gradient along Galactic radius. This might seems contradictory with the inner and outer halo of the clusters, where no separation in distance is seen between both components. We remark that the outer halo of Carollo et al. (2007) is in a metallicity regime where no clusters are found, which makes it dangerous to compare both components directly. We can still think of the inner halo as the product of a gravitational collapse and the outer halo as the product of mergers. But when and by how much did contribute the merged small systems to the Galactic halo remains to be quantified and goes beyond the purpose of this thesis, which is to study the stars of the inner halo.

As a final discussion we recall that halo stars are population II stars, meaning that their chemical compositions are $\alpha-$enhanced. As mentioned above, $\alpha-$enhanced stars were formed in an environment where Supernova Type II dominated the interstellar medium enrichment. This implies that the formation timescale for these stars was very short (less than 1 Gyr; Helmi 2008). The age difference for the population II stars of our sample of 1-2 Gyr is in agreement with this short formation timescale scenario. As discussed in Gilmore et al. (1989), studies of the correlations between stellar kinematics and metallicities show that the stars which formed during the dissipational collapse are those with [Fe/H] $\lesssim -1.5$, and their age range is set by the $\alpha-$enhanced chemical composition. Our results are telling us that we are observing mainly inner halo stars, which were formed rapidly in a short timescale during the collapse, supporting the Searle & Zinn (1978) scenario. To confirm these results it would be interesting to continue to study the kinematic properties of our stars. We could then see if the breakdown in our age-metallicity relation at [Fe/H] ~ -1.6 has a physical reason.

It is worth to discuss here that we cannot rely only on the TO temperature for the determination of absolute ages. We could see how only atomic diffusion –for which no conclusion about its efficiency has been achieved– gives 4 Gyr of difference in the absolute values. In addition, we could see that different stellar evolutionary models also yield different TO-temperatures, driving to different absolute ages. Interestingly enough, we can see that if we neglect diffusion completely, these ages become in a serious conflict with the age of the Universe (13.7 Gyr; Bennett et al. 2003). This argument implies a strong constraint against settling of heavy elements being fully inhibited in the interior of old metal-poor stars. Our isochrones show a well behavior in terms of diffusion (Salaris et al. 2000), which allow us to claim that the field stars of Galactic halo have an absolute age of 11-12 Gyr.

6.4 [Fe/H] - $\mathrm{T_{eff}}$ for Galaxy evolution

The [Fe/H] - $\mathrm{T_{eff}}$ diagram is a powerful tool to study the history of the Milky Way halo. In this section we show three applications of this diagram. We discuss firstly the presence of a dominant population in the halo in Sect. 6.4.1. Then we discuss a connection of this old population with the disk of the Milky Way in Sect. 6.4.2 and finally we discuss possible signatures of stars originated in other galaxies.

6.4.1 One dominating halo population

With the [Fe/H]-$(b-y)$ diagram, Schuster et al. (2006) suggested that the stellar halo is dominated by a coeval and old population, where the turn-off shows a clear blue cut-off as a function of metallicity. In our [Fe/H] - $\mathrm{T_{eff}}$ diagrams and our age-determinations we agree with this picture. To be consistent and probe that these conclusions are independent of the data set used for the halo field stars, we combined both studies.

One approach is to plot the $uvby - \beta$ photometric sample of Schuster et al. (2006, and references therein) together with our SDSS stars. From now on we will refer to the stellar sample of Schuster et al. (2006) as $uvby - \beta$ sample. Our stars have spectroscopic temperatures (or $ugriz$ colors) and the $uvby - \beta$ sample has only Strömgren photometry. To join these samples we need to transform colors in order to have all stars in the same reference system. Empirical color transformations are different for giants and for dwarfs (Alonso et al. 1996; Ramírez & Meléndez 2005), and we do not have this information for the stars of our sample. Therefore we considered only our MSTO temperatures indicated in Appendix C and transformed them to $(b-y)$ colors using the scale of Ramírez & Meléndez (2005) for dwarfs. Because our temperature values are very similar over the entire metallicity range, we use the fine version of the tables of I. Ramírez (priv. comm.), where the steps in temperature have a size of 50 K.

Our resulting MSTO $(b-y)$ color as a function of metallicity is plotted with the red line in Fig. 6.7, where we have also placed the colors and metallicities of the $uvby - \beta$ sample (Salaris, priv. comm.). The turn-off detected with spectroscopic temperatures in the SDSS survey has an excellent agreement with the blue cut-off of the $uvby - \beta$ sample, implying that we find the same coeval dominating halo population as Schuster et al. (2006).

It is important here to remark the advantages of using the SDSS: our sample of halo stars is huge, which means that the MSTO as a function of [Fe/H] is very accurate. As a test, we applied the Sobel Kernel edge-detector (see Sect. 5.2.2) to find the $(b-y)$ color cut-off traced by the turn-off in the $uvby - \beta$ sample. The values obtained as a function of metallicity are illustrated with the blue dashed line in Fig. 6.7, which shows how important is to have a large sample of stars. The $uvby - \beta$ sample sample contains for some [Fe/H] values (especially those at low metallicities) very few stars and the turn-off cannot be detected by the Sobel Kernel properly. For that same [Fe/H] value, however, the SDSS data provide a clear cut-off and the Sobel Kernel yields realistic TO values.
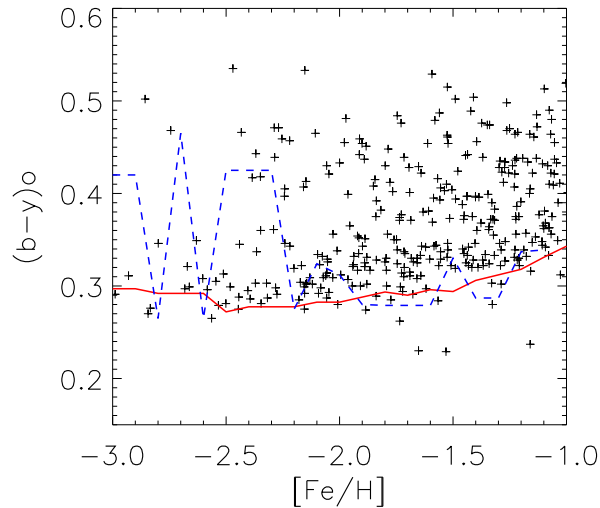
Figure 6.7: $(b-y) - $ [Fe/H] diagram of the photometric sample of Schuster et al. (Salaris, priv. comm.). The red line corresponds to the MSTO determined from the SDSS sample as indicated in Appendix C and transformed to Strömgren photometry using the empirical relations of Ramírez & Meléndez (2005). There is a perfect agreement between the cutoff of SDSS and the $uvby - \beta$ samples. The blue dashed line corresponds to the MSTO determined applying the Sobel Kernel edge-detector to the stars of the $uvby - \beta$ sample.

6.4.2   Disk stars

Our age-metallicity relation tells us that the stars of our sample are coeval and old. As discussed in Chap. 5, for [Fe/H] > -1.3 we cannot obtain accurate ages because the turn-off was not well detected. We could see in Fig. 5.11 how disk stars can have bluer colors at high metallicities, but the turn-off does not show a clear envelope as the halo does, and our method to detect the ages is not plausible.

As in the case of the halo, efforts to find an age-metallicity relation for the Galactic disk (namely thick and thin disks) have still not reached a consistent answer as to why our solar neighborhood is as we observe it today. There are much more accurate data for field stars in the solar neighborhood than for the halo, meaning that there have been many attempts to find an age-metallicity relation using individual field stars. Although important works on the subject reveal that there is no relation between age and metallicity in the solar neighborhood (Nordström et al. 2004), there are studies that conclude the opposite. Pont & Eyer (2004), using bayesian methods to determine ages, and found that the age-[Fe/H] relation of Nordström et al. (2004) could have been biased by the age determination method. They re-analyzed their data set and found a definitive monotonic relationship between age and metallicity.

It goes beyond the purpose of this thesis to review the history of the age-metallicity relation for the solar neighborhood. What we want to remark here is that despite the debates

mentioned above, there is an agreement in the sense that the most metal-poor stars of the solar neighborhood are old (10-12 Gyr); and that no significant scatter in age is seen for them (Nordström et al. 2004; Pont & Eyer 2004; Bensby et al. 2007; Schönrich & Binney 2009). These stars could be connected with halo stars, which would put our result in a consistent picture respect to these results of age-metallicity relations for the Milky Way.

6.4.3 Blue metal-poor stars

There are some stars in Fig. 6.7 at high metallicities that are bluer than the MSTO traced with the red line. These stars are also seen in our [Fe/H] - T_{eff} diagrams from SDSS. In the special case of the *G blue* sample, where we have a large contamination with blue horizontal branch stars due to selection effects, we see a considerable number of stars at hotter temperatures than the MSTO (see e.g. Fig. 6.2). We discussed in Chap. 5 how blue horizontal branch stars contaminate the hotter part of the [Fe/H] - T_{eff} diagram and how some of the color target selections can exclude them. The *FG* sample (Table 5.1) had a very clear envelope traced by the MSTO, but it was biased at low metallicities due to the lack of metal-poor turn-off stars. Concerning the metal-rich side, the [Fe/H] - T_{eff} diagram of the *FG* sample (see the right panels of Fig. 5.8) contains hotter stars, even after the drastic exclusion of blue horizontal branch stars.

These stars have also been discussed by Schuster et al. (2006) and Unavane et al. (1996) in their [Fe/H] - T_{eff} diagrams. They have been interpreted as blue stragglers (Preston & Sneden 2000; Carney et al. 2005). Another explanation for them is that they are younger, probably formed in an external galaxy and then accreted on to the Milky Way halo (Preston et al. 1994; Unavane et al. 1996). This explanation fits well with the hierarchical formation of the Milky Way, which has gained popularity over the years thanks to the large amount of observational evidence (Ibata et al. 1994; Belokurov et al. 2006; Helmi 2008). Further studies on the kinematical properties of these stars in the dominating halo population would contribute to this picture. If these blue metal-poor stars belong to younger populations that come from mergers, they then must have different kinematics to the Galactic halo formed from the collapse. This has been already observed by Preston et al. (1994) and it would be interesting to analyze the SDSS data with respect to this scenario. Another possible way to reveal the origin of these stars is by detailed chemical abundance analyses, because the chemical abundance patterns of the local dwarf galaxies is different to that of the Milky Way (Tolstoy et al. 2003; Helmi 2008). Again we stress here the comment made by Schuster et al. (2006): it would be interesting to perform a follow-up high resolution spectroscopic analysis on these blue metal-poor stars.

6.5 Discussion and conclusion

The ages of metal-poor stars contribute to current debates concerning stellar evolution theory. In addition, they contribute to the understanding of the structure and formation of the Galactic halo. In this chapter we have discussed some of these topics by determining

the age of a sample halo field stars. Using the main-sequence turn-off of a halo sample from SEGUE/SDSS, we looked for the isochrones according to this turn-off temperature. This approach to find ages has been employed by other authors (Schuster & Nissen 1989; Schuster et al. 1996; Unavane et al. 1996; Schuster et al. 2006; Allende Prieto et al. 2006), where the values of the absolute ages have droped more than 4 Gyr between the studies in 1996 and in 2006.

In the first part of this Chapter, we focused on this difference of absolute ages given by the literature. For that we introduced the process of gravitational settling of heavy elements, especially helium, in the interior of stars. We explained the effect that this process has on the age determination of metal-poor low-mass stars. Stellar evolutionary models including diffusion have a tendency of predicting lower turn-off temperatures and luminosities. The determination of ages of halo field stars with this method is strongly dependent on the temperature of the turn-off, therefore on atomic diffusion. As a first result we found a difference of 4 Gyr in the absolute ages obtained by using isochrones with and without diffusion, when GARSTEC stellar evolutionary models were used. Although we were aware that this value can change when using other stellar evolutionary codes, our results have shown to be consistent with the literature. Concerning the current debate about the efficiency with which atomic diffusion acts in stellar interiors, our results are a strong argument in favor of using diffusive isochrones for the age determination of field population II stars, because canonical isochrones yield ages larger than the age of the Universe. Based on our diffusive isochrones, we determined an age of 11-12 Gyr for the Galactic halo dominating population.

The MSTO traced by the hotter envelope of the [Fe/H] - T_{eff} diagram was used also to discuss our relative ages as a function of metallicity. The absence of a trend was interpreted as a rapid stellar formation scenario during the collapse of the inner halo. This theory was firstly suggested by Eggen et al. (1962) and has been followed by many works on globular clusters (e.g. Salaris & Weiss 2002; De Angeli et al. 2005) and field stars (e.g. Schuster et al. 2006; Carollo et al. 2007), which is combined with the theory of Searle & Zinn (1978) to explain the evidence of accreted material into the halo. We commented on the presence of stars that are hotter than the turn-off of the dominant halo population, which were also noted by Unavane et al. (1996) and Schuster et al. (2006) from their [Fe/H] - T_{eff} diagrams. An interesting interpretation of these stars is that they are a young population originated in small galaxies and were later on accreted by the Milky Way. Further studies of kinematics and detailed chemical abundances are necessary to consolidate these suggestions.

We combined our sample with that of Schuster et al. (2006, and references therein). For that we transformed our MSTO temperatures to Strömgren colors and superposed this new MSTO-color to the photometric sample. We could reproduce perfectly the blue envelope of the Schuster et al. sample, which implies that the signatures of a dominating coeval inner halo field population is independent of the data set used. A final remark concerning this result is that we have analyzed not only a completely independent data set, we also have developed a novel method to analyze the data. It is encouraging to see the consistency of our results with respect to those of Schuster et al. (2006), given the originality of our

methodology.

Chapter 7

Globular Clusters

In the Galactic halo, globular clusters are stellar systems that are relatively well studied because they constitute mainly on stars of the same age, metallicity and distance. They are laboratories of stellar evolution and reveal key information about the structure and formation of the Milky Way. In this chapter we used a sample of 11 globular clusters observed by SDSS to consolidate our results obtained in Chap. 6. We discuss the color distributions as a function of metallicity for field and cluster stars as observational evidence of a common nature between clusters and field stars. Finally we compared the results for the ages with those of the clusters obtained using different methods in the literature, where we could find an agreement.

7.1 Motivation

Approximately 150 globular clusters (GC's) and about 20 satellite galaxies are found connected to the Milky Way (Harris 1996; Helmi 2008). GC's constitute an homogeneous sample of stars with the same age, metallicity and distance[1]. They have been largely used as tracers of the Galactic halo because they span a wide range of distances, ages and metallicities and their properties can be estimated with better accuracy than for individual field stars. Searle & Zinn (1978) used globular clusters to suggest Galactic halo underwent a long formation period, in which it accreted external galaxies. This theory is combined with that of Eggen et al. (1962), which suggests that the halo was formed via gravitational collapse. It is now believed that the inner halo formed through the collapse while the outer halo through accretion. Current age-metallicity relations of halo globular clusters agree with this scenario, although the spread and trend of the relations is still under debate (Sarajedini et al. 1997; Salaris & Weiss 2002; De Angeli et al. 2005). In any case, there is an agreement that most of them are old, with ages of 10-14 Gyrs (Salaris & Weiss 2002; Dotter et al. 2010). The kinematics of disrupted tidal features of the clusters may also play an important role in revealing that the Galactic halo may have been formed from the accretion of dwarf galaxies (Martínez Delgado et al. 2004; Law & Majewski 2010). In addition to the clusters, stellar streams have recently been observed with large-scale surveys of field stars. The SDSS, for instance, has shown several complex substructures of the Galactic halo (Belokurov et al. 2006; Newberg et al. 2007; Yanny et al. 2009a). Thus, the ongoing dissolution of globular clusters implies that some fraction of halo stars were initially formed in GC's (Odenkirchen & Grebel 2004; Jordi & Grebel 2010; Chun et al. 2010).

These evidence makes us to believe that the stars of the Milky Way halo have a common history, where field and globular cluster stars are of the same nature. But there are still some pieces missing in this puzzle that do not allow to confirm this scenario. For example, there is already a significant number of extremely metal-poor field stars in the Galactic halo (Beers et al. 1992; Christlieb et al. 2002), but there are no globular clusters with $[Fe/H] \lesssim -2.4$. In addition to that, the discovery of different chemical patterns in stars of the same globular clusters suggest that they have at least a first and second population (Gratton et al. 2004). Carretta et al. (2010) propose that the primordial population of GC's might be the main building block of the halo. A study of halo field stars coming from first and second generation of GC is performed by analyzing the chemical patterns. These observations do not lead to a census of how much the clusters have contributed to the field

---

[1]We mention the several interesting works over the last years discussing the different chemical patterns observed in many globular clusters as indicators of multiple populations (Gratton et al. 2004; Baumgardt et al. 2008; Carretta et al. 2010, and references therein). We are totally in agreement that today it has become inaccurate to affirm that a GC has stars of same age and chemical composition. The age difference between the two main generations is usually of the order of the errors obtained for the age estimates (~ 1 Gyr, Salaris & Weiss 2002). In our particular work, we are dealing also with metallicities that have errors of 0.25 dex, meaning that for the purpose of this work we can still approximate a globular cluster as a population of stars with same age and metallicity.

stars population (Martell & Grebel 2010; Carretta et al. 2010). It is therefore necessary to keep studying the distributions as well as the internal properties of GC's in the context of Galaxy history. In particular, it is worthwhile to compare their stellar populations with the halo field stars.

In Chap. 3 we have determined metallicities and temperatures for field halo stars using the spectra from the SDSS survey. We placed them in [Fe/H] - T_{eff} diagrams in Chap. 5 and show that the hottest stars trace an envelope which is connected to the main-sequence turn-off. Without the information of distance and mass of these stars, we could still determine the age of the youngest halo population (Chap. 6). This was done by looking at the turn-off temperatures and comparing it with theoretical isochrones. The ages determined by this method were very dependent on the atomic diffusion considered in the isochrones, leading to the conclusion that using only the MSTO temperature is not enough to give an absolute age for the turn-off stars from the halo. We gave to the field stars from the Galactic inner halo an age of 11-12 Gyr using diffusive isochrones, because the resulting ages obtained from the canonical models were larger than the age of the Universe.

In this chapter we attempt to consolidate our results for the ages by considering GC's. Therefore we related cluster and field stars by studying the colors of the stars. For this purpose we use a sample of the clusters observed with the SDSS telescope. The cluster sample is described in Sect. 7.2. We discuss observational evidence of a common origin between cluster and field stars relating their color distributions in Sect. 7.3. Based on this evidence we use the cluster ages taken from the literature to constrain the ages of the turn-off halo stars in Sect. 7.4. Summary and conclusion of this chapter are given in Sect. 7.5

7.2 Globular clusters sample

The SEGUE survey (Yanny et al. 2009b) used special plates to target clusters, which were used to calibrate the SSPP atmospheric parameters (Lee et al. 2008b). An et al. (2008, hereafter An08) employed the DAOPHOT crowded-field photometry package to derive accurate photometry of the clusters, providing a well-defined cluster sequence from the lower main-sequence to the red giant branch. The *ugriz* photometry of An08 for these clusters is published on the SDSS web pages[2]. The advantage in using these clusters to study the properties of our SDSS field stars is that we avoid color transformations, which can introduce systematic errors (Weiss & Salaris 1999; An et al. 2009).

Given the sample of the 17 An08 clusters, we excluded NGC 2419, Pal 3, Pal 14, Pal 4 and NGC 7006 because they are too faint for SDSS filters to detect stars with magnitudes at the turn-off and main-sequence. This can be seen in the color-magnitude diagrams (CMD) of An08, which contain only stars at the red giant branch. In addition, we excluded the cluster M71 because it is more metal-rich ([Fe/H] = -0.81) than our field halo population. The resulting 11 clusters are summarized in Table 7.1. We considered the metallicities adopted by An08, which we took from their Figures 12-14. The metallicity scale is that of

---

[2]http://www.sdss.org/dr7/products/value_added/anjohnson08_clusterphotometry.html

Kraft & Ivans (2003) for all the clusters except those with an asterisk, which correspond to that of Harris (1996). Table 7.1 contains also in the 4th column the color of the turn-off (explained below) and the reddening value from Schlegel et al. (1998) in the 5th column.

Cluster		[Fe/H]	$(g-r)_{\mathrm{TO}}$	$E(B-V)$
NGC	other			
4147		-1.79	(0.22)	0.03
5024	M53	-1.99*	0.18	0.02
5053		-2.41	0.17	0.02
5272	M3	-1.50	0.23	0.01
5466		-2.22*	0.19	0.02
5904	M5	-1.26	(0.28)	0.04
6205	M13	-1.60	0.25	0.02
6341	M92	-2.38	(0.22)	0.02
7078	M15	-2.42	0.25	0.03
7089	M2	-1.56	0.26	0.04
	Pal 5	-1.41*	(0.34)	0.06

Table 7.1: Globular clusters properties taken from An et al. (2008). Metallicities adopted are those of Kraft & Ivans (2003). The values with an asterisk have metallicity adopted by Harris (1996). The value of the turn-off color calculated using the Sobel Kernel technique is indicated in the forth column. Values in parenthesis are the adopted turn-off color taken from the fiducial sequence of the cluster, as given by An et al. (2008), The reddening from (Schlegel et al. 1998) are indicated in the fifth column.

Reddening correction

The magnitudes of the stars need to be corrected by extinction previously to the analysis. For field stars, the magnitudes of the *G blue* sample are already de-reddened from the $E(B-V)$ coefficients when taken from Schlegel et al. (1998). For the clusters, the values of the extinction coefficient $E(B-V)$ are indicated in Table 7.1 and were taken from An08, who also considered those of Schlegel et al. (1998). Since the clusters have *ugriz* photometry, a filter transformation is needed in order to use the $E(B-V)$ coefficient to correct for extinction.

As example consider an arbitrary magnitude *mag* of a star. The de-reddened magnitude mag_o is given by the formula:

$$mag_o = mag - A(mag), \tag{7.1}$$

where $A(mag)$ is the extinction coefficient, which is dependent on the filter. The ratio of total to selective extinction, designated as R, is defined as the connection of the total
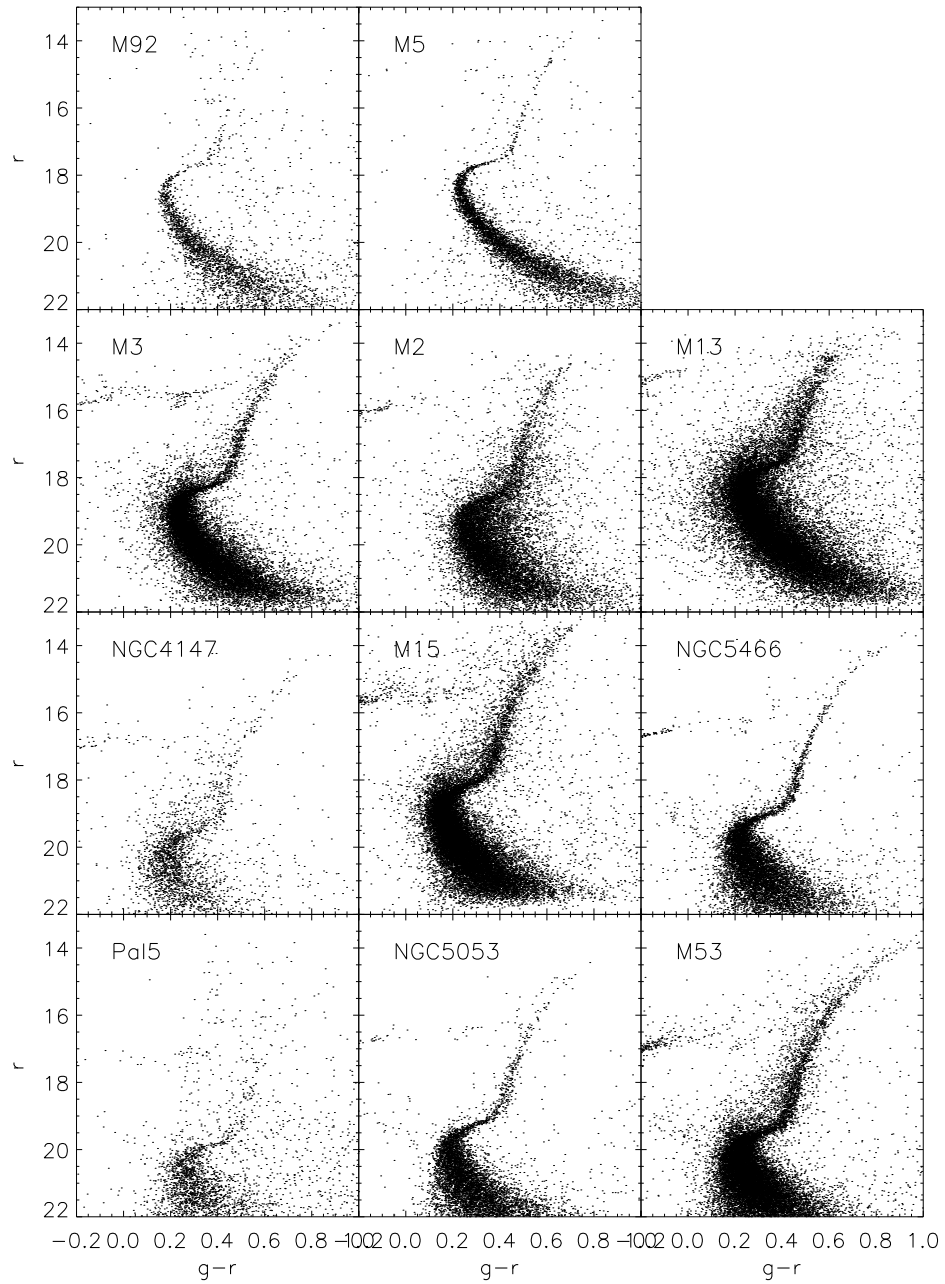
Figure 7.1: De-reddened color magnitude diagrams of the clusters.

extinction in mag and the difference in the extinction between the BV filters $E(B-V) = A(\text{B}) - A(\text{V})$ through

$$R_{mag} = \frac{A(mag)}{E(B-V)}. \tag{7.2}$$

The quantity $E(B-V)$ is referred to as the *reddening* or *color excess*, because it is derived from the difference between the apparent color $B-V$ and the unobscured color $(B-V)_o$. Replacing Eq. 7.2 in Eq. 7.1 the generic relation to correct by reddening is

$$mag_o = mag - R_{mag} \cdot E(B-V). \tag{7.3}$$

For the filters ugr we used the values $R_u = 4.8$, $R_g = 3.775$ and $R_r = 2.58$ respectively, which were taken from Table 1 of McCall (2004). The de-reddened color-magnitude diagrams of the 11 clusters used for this study are displayed in Fig. 7.1.

7.3   Observational evidence

Without previous assumption concerning Galaxy structure and formation or stellar evolution theory, we present in the following two observational evidences that cluster and field stars are somehow similar. We first compare the turn-off color of the cluster with the field stars as a function of metallicity in Sect. 7.3.1. Then we select the field stars with the clusters metallicities and compare this color distribution with that of the cluster in Sect. 7.3.2. We show that the color distributions look similar to field and clusters, where the turn-off as a function of metallicity obeys the same trend. We discuss implications of these results in Sect. 7.3.3.

7.3.1   Turn-off color

In order to determine the turn-off (TO) for clusters and field, we employed the same technique. We adapted the Sobel Kernel technique explained in Sect. 5.2.2 to find the edge in the color distribution. The methodology for the field is the same as described in Chap. 5 but using this time colors instead of temperatures. Clusters stars having the same metallicity and TO color can be simply found from histograms of the color distribution. The value of the turn-off $(g-r)$ color is indicated in the forth column of Table 7.1 (the value listed in the table is not corrected by reddening). The numbers in parenthesis in Table 7.1 represent the turn-off point of the cluster fiducial sequence taken from the Tables 9-28 of An08. A cluster fiducial sequence is defined as the locus of the density peaks in the color-magnitude diagram. We decided to consider the fiducial TO-point[3] for these clusters because we were not able to detect properly the TO with the Sobel Kernel technique.

The rather narrow sequence of M92 and M5 (see top panels of Fig. 7.1) produced an abrupt drop in the color distribution. As an example, we have plotted in Fig. 7.2 the CMD of M5 in the upper panel and its color distribution in the lower panel. The edge-detection filter gave its maximum response in the blue side of the drop, which is illustrated with the blue line in Fig. 7.2. This yielded a TO located in a color region where there were very few stars in the CMD. The TO given by the fiducial sequence, however, is located at the red side of the drop. It is instructive to remark that the turn-off given by the fiducial

---

[3]Whenever we refer to fiducial TO we are referring to the TO of the cluster fiducial sequence.

sequence does not represent the *bluest* point. The mean in the CMD at the region close to the TO will yield redder value than that obtained from the Sobel Kernel filter. For the narrow sequence of M92 and M5 we accept the bluest point of the fiducial sequence as a good approximation of the main sequence turn-off. The sparsely populated clusters NGC4147 and Pal5, on the other hand, did not show a clear TO in the color distribution. It produced unrealistic edge-detection with the Sobel Kernel, driving us to use for these cases the fiducial TO of An08 as well. We are aware that this value is not as good approximation for the bluest point as for the other two cases discussed above, but it is still better to use TO-point given by the fiducial sequence than by the Sobel Kernel filter.

Using the $E(B-V)$ reddening value indicated in Table 7.1 and the de-reddening correction formula of Eq. (7.3), we corrected the turn-off color for each cluster and plotted them against their metallicity, as seen with the red asterisks in Fig. 7.3. The blue line indicates the MSTO color of the field stars, with the dashed line representing the bootstrapping error obtained with the Sobel Kernel technique. In Fig. 7.3 we observe how the MSTO color as a function of metallicity of the field stars agrees well with that of the globular clusters. We see that metal-poor stars have a bluer turn-off color than metal-rich ones at the same evolutionary stage.
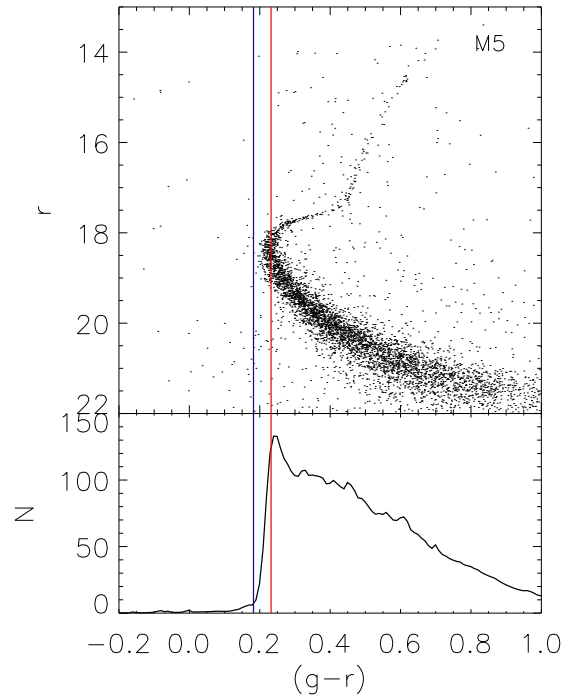
Figure 7.2: Upper panel: M5 color-magnitude diagram. Lower panel: color distribution, smoothed with the probability function given by Eq. 5.1. The red line corresponds to the turn-off from the fiducial sequence while the blue line to that obtained from the Sobel Kernel technique.

The trend of the MSTO color plotted in Fig. 7.3 with the blue line corresponds to the quadratic polynomial

$$(g - r)_{\text{TO,field}} = 0.467 + 0.217 \cdot [\text{Fe/H}] + 0.039 \cdot [\text{Fe/H}]^2. \tag{7.4}$$

It is very similar to the trend of the MSTO color of the globular clusters, plotted with the red dotted line, which is

$$(g - r)_{\text{TO,GC}} = 0.471 + 0.217 \cdot [\text{Fe/H}] + 0.035 \cdot [\text{Fe/H}]^2. \tag{7.5}$$

The coefficients of the parabola are very similar and have an offset of 0.04 mag at the zero-point, which is smaller than the bootstrapping errors obtained for the TO-detection of the field stars. In Fig. 7.3 we can see how the TO-color of the GC lie within the TO-color of the field, with the globulars being slightly bluer than the field stars. In general terms, the TO-color of field and clusters agree, suggesting that the age trend of the MSTO field stars should also agree with that of the clusters. We will come to this point in Sect. 7.4.
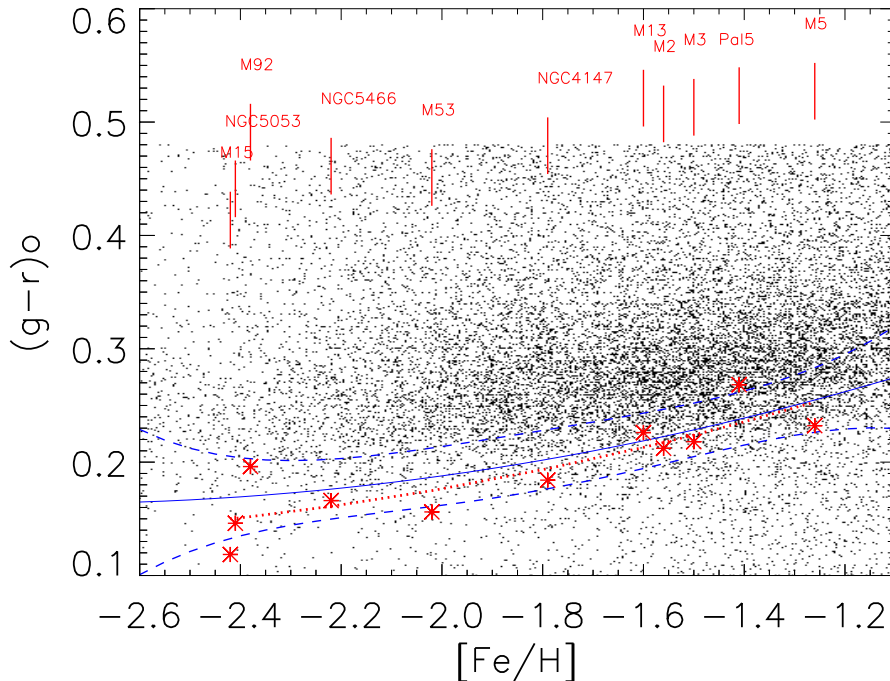
Figure 7.3: De-reddened $(g - r)$ color of 10,000 randomly selected field stars as a function of metallicity. The blue line correspond to the turn-off and the dashed line its error. Red asterisks indicate the turn-off de-reddened $(g - r)$ color and metallicity of 11 clusters of An et al. (2008). Their names are indicated at the top of the diagram.
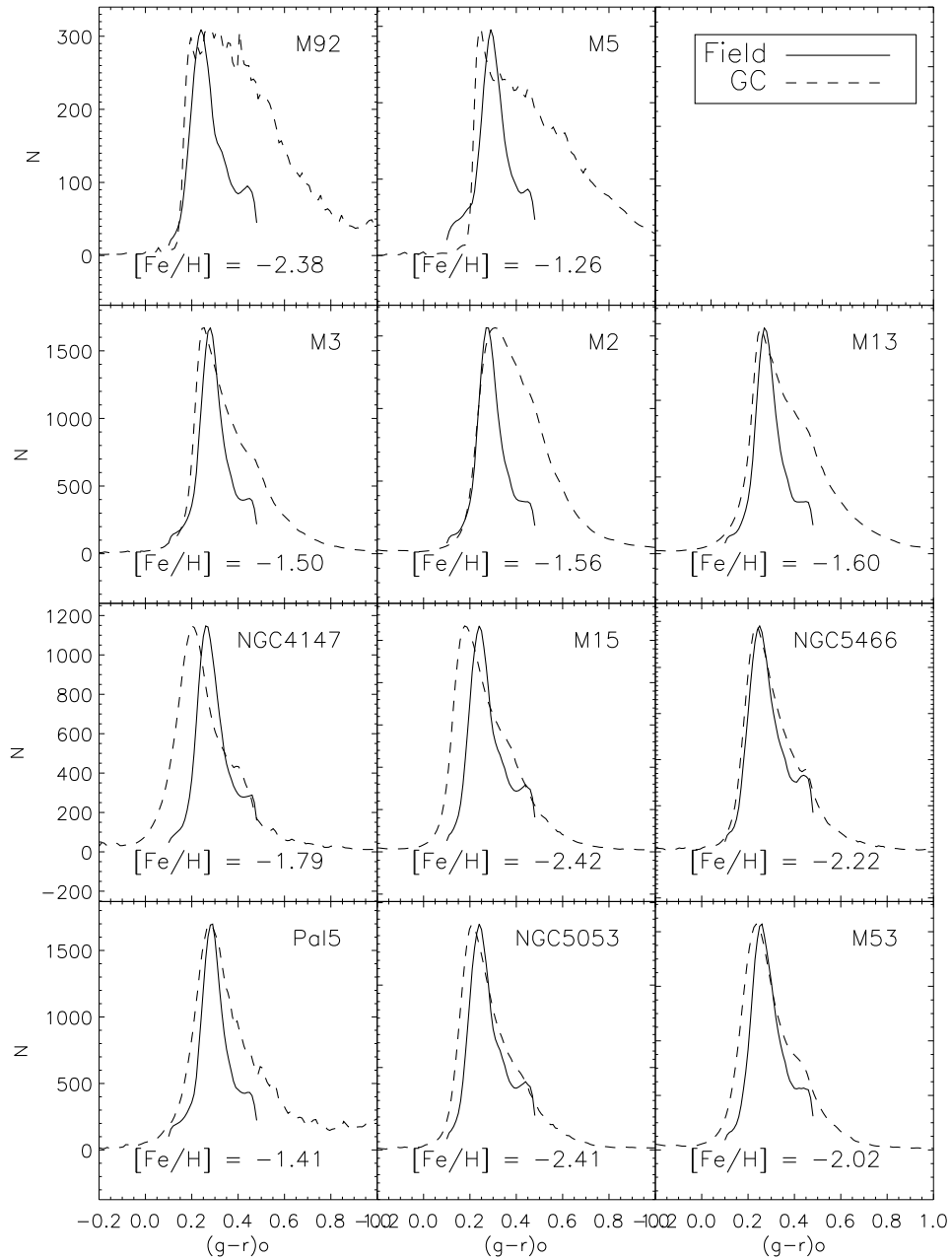
Figure 7.4: Color distribution of the globular clusters of Table 7.1 with dashed line. The distribution for the field stars with the same metallicity as the cluster is plotted with solid line.

7.3.2   Color distribution

The other interesting result obtained by comparing clusters with the field stars is the shape of the color distribution. For each globular cluster with $[Fe/H] = [Fe/H]_{GC}$, we selected the stars with metallicities of $[-0.15, +0.15]$ around the cluster metallicity value and calculated the probability function given by Eq. (5.1) of the color distribution. The same probability function was determined for the color distribution of the cluster. Comparisons for the 11 GC are displayed in Fig. 7.4. The clusters and the field population at the cluster metallicity usually do not have the same number of stars, therefore we scaled the distribution to compare them in a better manner: For N_{GC} being the maximum amount of stars in the cluster and N_{field} the maximum number of the field stars, we scaled the cluster distribution to have the maximum of the the field by multiplying the distribution with N_{field}/N_{GC}. In Fig. 7.4, the metallicity and the name of the clusters are indicated in each panel.

To understand better the color distributions, we have taken the cluster NGC5466 as an example and plotted them separately in Fig. 7.5. The first feature seen in Fig. 7.4 and 7.5 is the similar shape of the distributions. This is especially seen at the turn-off, which is ensquared with the blue dashed box in Fig. 7.5. The color of the maximum number of stars in the GC agrees with the respective field stellar population, as can be observed also in Fig. 7.4. There are exceptions, like NGC4147, where the color distribution of the cluster is bluer than that of the field. We will discuss this case below, here we only want to show that even for NGC4147, the shape of the distribution at the turn-off agrees between cluster and field.

When moving towards the red side of the color distribution, we see that for field and clusters the number of stars decreases. The decreasing slope for the field is larger than for the cluster. This is mainly due to selection effects. The *G blue* sample is concentrated in selecting mainly turn-off stars (see Chap. 5 for details of the stellar sample). Because field stars are far away from us, the dwarfs observed by SDSS have usually magnitudes of $r \sim 19 - 20$ mag (Yanny et al. 2009b). Since SDSS cannot observe stars below $r \sim 22$ mag (Abazajian et al. 2009), the samples from SDSS have few stars at low main-sequence phases. We can see in the cluster CMDs of Fig. 7.1 that those with luminous turn-offs have a well populated region at the red side of the color distribution, which can be seen in Fig. 7.4. This is because SDSS can observe more dwarfs for these brilliant clusters. That is why dwarfs populate the red side of the color distribution. The opposite is observed for clusters with a less luminous TO magnitude. Finally, we observe that some clusters present a large contamination with field stars. M2 and M3, and Pal5, for example, have very noisy CMD as seen in Fig. 7.1 and show a quite populated red region.

The decrease in the number of stars towards the red side is because these stars are, on one hand unevolved main-sequence stars –which are numerous but their very low luminosities make them difficult to be observed with our telescopes– and on the other hand, they are red giants –which are brilliant, but their quick evolution makes them rare in the sky. We expect therefore a decrease in the color distribution towards the red in the globular cluster CMD.
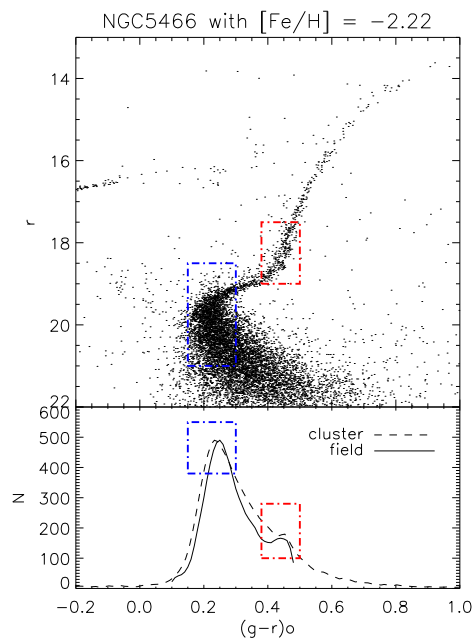
Figure 7.5: Upper panel: NGC5466 color-magnitude diagram. Lower panel: color distribution of the cluster with dashed line and the field of cluster metallicity with solid line, smoothed with the probability function given by Eq. 5.1.

Another interesting feature of the red side of the distribution worthy to discuss is the second peak at $(g - r)_o \sim 0.45$. Figure 7.5 shows the CMD of an example cluster, where these stars are ensquared with the red dashed box. One explanation of this second peak would the presence of an older population with a redder TO color. This is impossible, since the age corresponding to this TO-color is older than the age of the Universe (more than 18 Gyr). These stars must belong to a younger stellar population. We identify them using the CMD and luminosity function, where we use as an example the cluster NGC5466. We then use properties of the color distributions to justify that this peak corresponds to the same stars in the field.

Red giant branch stars in the clusters

The stars at the red peak of the color distribution can be found in the globular clusters quite easily. We can separate the dwarfs from the giants of the cluster by using the fiducial TO-magnitude of An08, which is illustrated in Fig. 7.6 with the blue horizontal line. We calculated separately the color distributions for the dwarfs and giants, as illustrated in the lower panel of Fig. 7.6. The distribution of the dwarfs present a smooth decrease of stars towards red colors, while the distribution of the giants present a notable second peak at $(g - r)_o \sim 0.45$. Only the giants present a peak at red colors, which is indicated with the
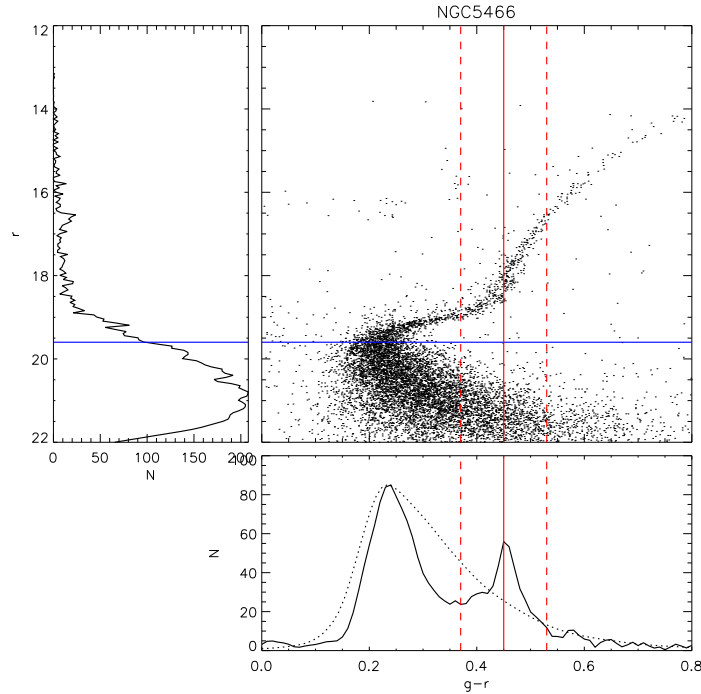
Figure 7.6: CMD of NGC 5466. The turn-off magnitude of the fiducial sequence (An et al. 2008) is represented with the blue horizontal line. Lower panel: color distributions of dwarfs (dotted line) and giants (solid line) of the cluster, separated with the limit of the TO magnitude. The distribution of the giants show a second peak, with its maximum represented with the red vertical line. Dashed lines indicate the width of the peak. Left panel: luminosity function of the cluster.

red vertical lines. When looking at the CMD, we see that this peak is the result of the accumulation of stars at the base of the red giant branch (Iben 1967). Hereafter we refer to this stars as BGB. The large concentration of stars at this color is a pure optical effect, because the BGB is the point where the red giant branch is the steepest and the stars have the same temperature, regardless of their mass and evolutionary stage. Stars that lie at redder colors than the BGB are very massive and evolve quick, observing therefore few of these stars in the cluster. The second agglomeration of stars then decreases again to the red end of the color distribution.

Only the temperature of the BGB is independent of mass, the luminosity is different for stars with different masses. This is the reason why we do not see an accumulation of stars at the BGB of the cluster in the luminosity function plotted at the left side of Fig. 7.6. Note the presence of another peak in the luminosity function at $r \sim 16.7$ mag. This corresponds to the horizontal branch stars in the CMD, which have a constant magnitude producing an accumulation of stars in the luminosity function.

Red giant branch stars in the field

For field stars we cannot separate giants from dwarfs because we do not know the distance or the surface gravity accurately enough. Therefore we used correlations based on properties of the color distributions of clusters to show that the second peak of the field distribution is also connected with BGB stars. First, we used the values of the maxima of both peaks ensquared in Fig. 7.5. For N_{TO} being the value of the color distribution at the maximum of the turn-off stars and N_{BGB} the maximum of the BGB stars, we calculated $\Delta N = N_{\text{TO}} - N_{\text{BGB}}$. We obtained this value for cluster and field distribution of each panel in Fig. 7.4, except for M92, M5 and Pal5, because for them we could not see a clear signature of BGB stars in the distribution of the giants.

The comparison between the values obtained for field and cluster is displayed in panel A of Fig. 7.7. There is a good correlation of 0.89 between the values. For better visualization we performed a linear fit to the points in panel A, which is represented with the green dashed line. Note there are two points off the general trend, which are ensquared with green diamonds. They correspond to the clusters M2 and M13, which have CMD with especially broad main-sequences and red giant branch, together with a large contamination with field stars. For these two clusters we get a smaller value for ΔN producing a larger difference against the field. When excluding these two clusters, we obtain a correlation value of 0.98 and the linear fit is represented with the red line.

We also considered the number of stars that lie in the color domain of the second peak, as indicated with the dashed vertical lines in our example cluster in Fig. 7.5. The ratio of these stars with the total number of the stars $N_{\text{BGB}}/N_{\text{tot}}$ is plotted for clusters and field as a function of metallicity in panel B of Fig. 7.7 with diamonds and triangles, respectively. To visualize better the trend, we performed again linear fits to the values, which are shown with red and blue dashed lines, for the clusters and field, respectively. The clusters have in general more BGB than the field, which is due to the selection effects discussed above. Although the slope of both trends are different, we can see that for both cases there are more giants in relation to the total number of stars at lower metallicities. One reason is that the red giant branch of a metal-poor isochrone is bluer than a metal-rich one (Salaris et al. 2002), meaning that due to our color constraint, we expect a larger contamination with metal-poor red giants than metal-rich ones. In addition to that, the shape of the red giant branch becomes more horizontal for metal-rich stars, meaning that metal-rich red giant stars have a larger range of colors than metal-poor ones. This has a consequence in a less concentrated peak in the color distribution for metal-rich populations than for metal-poor ones.

The third comparison is shown in panel C, where we have plotted the difference in *color*, $\Delta(g - r)$, between the red and the blue peaks. This is indicated for the clusters with diamonds and for the field with triangles. Again, to visualize better the trend, we performed a linear fit to the values, represented with the red and blue dashed lines for cluster and field stars, respectively. The linear curve for the clusters has the form

$$\Delta(g - r)_{\text{GC}} = 0.16 - 0.021 \cdot [\text{Fe/H}], \tag{7.6}$$
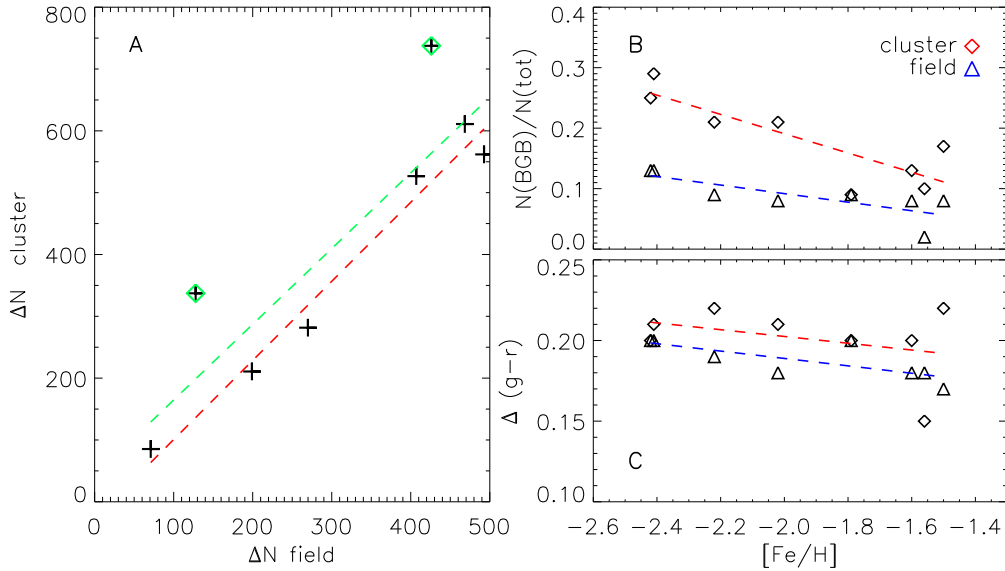
Figure 7.7: Left panel: Correlations of the difference of the maxima of major and second peaks of the color distribution for field and clusters. The green diamonds correspond to points off the general trend (see text). The green line represents the linear fit considering all points while red line excludes the two off-points. Upper right panel: Ratio between the number of stars in the second peak and the total of the population as a function of [Fe/H]. Lower right panel: Difference in color between the major and the second peak of the color distribution as a function of [Fe/H]. For both right panels diamonds indicate the cluster population while triangles the field one. Linear fits have been performed to each correlation as indicated by dashed lines.

while for the field the form is

$$\Delta(g - r)_{\mathrm{F}} = 0.14 - 0.022 \cdot [\mathrm{Fe/H}]. \tag{7.7}$$

The slope of both trends agree, so that the relative difference of them as a function of metallicity is the same for field and clusters. There is a small offset of 0.02 mag, which means that the clusters have a slightly larger color difference between the TO and RGB than the field. Note that this relation implies that like the MSTO has redder color for higher metallicities in cluster and field, the RGB has redder color for higher metallicites as well, which agrees with Salaris et al. (2002).

The results obtained from the comparisons shown in Fig. 7.7 justify that the second peak of the field color distribution at constant metallicity corresponds to red giant branch of the same population, like in globular clusters. Some contamination with BGB is expected in the *G blue* sample, because their colors lie in the color constraint of this sample (see Table 5.1). An example is shown in Fig. 7.8, where the left panel has the color-color diagram of the cluster M13 and the right panel the color-color diagram for the field stars with the cluster metallicity ([Fe/H]= -1.6). The blue line corresponds to the fiducial

sequence of this cluster taken from An08, from where we have indicated in red the base of the red giant branch of the fiducial sequence. An et al. (2009) have calibrated theoretical isochrones to the *ugriz* system and also estimated ages for some of the clusters of our sample, including M13 with the age of 14.3 Gyr. In addition, they have compared the color transformation of their models and those of Girardi et al. (2004) and Dotter et al. (2007). Their isochrones agree in general well with each other, although those of Girardi et al. (2004) do not consider $\alpha-$enhanced abundances, which introduce differences in the red giant branch. They claim that for all models used in their study, the empirical color relations work well for main sequence stars near the turn-off, but there are systematic offsets for colder temperatures. For this reason we decided to plot fiducial sequence of M13 instead of the 14 Gyr isochrone with the cluster metallicity. A number of red giant branch is expected in our color constraint, as seen with the red color of the fiducial sequence in Fig. 7.8.
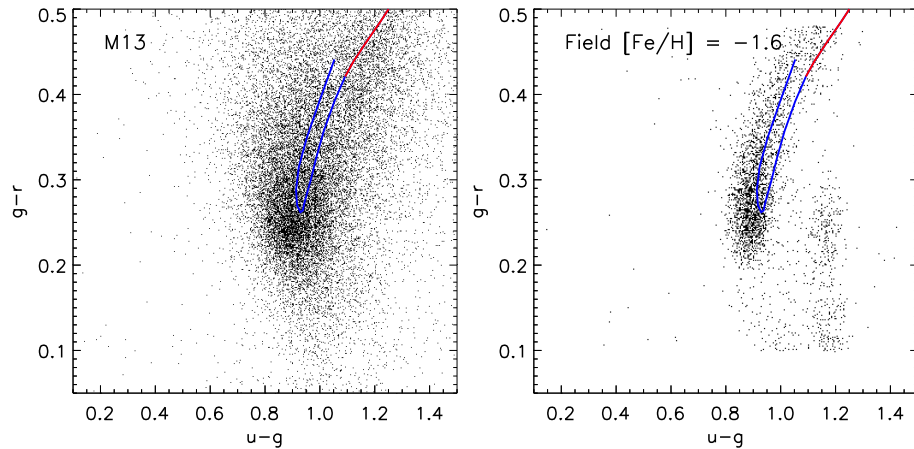
Figure 7.8: Left panel: $(u-g)-(g-r)$ color-color diagram of M13. Right panel: color-color diagram of the field stars with [Fe/H]= -1.6, according to M13 metallicity value. Blue line illustrates the fiducial sequence of the cluster as determined by An et al. (2008). Red color correspond to the stars a the base of the red giant branch. A number of red giant branch is expected in our color constraint.

7.3.3   Implications

The excellent agreement of the turn-off color as a function of metallicity found in this work as seen in the [Fe/H]-color diagram of Fig. 7.3 is an argument that we are finding the main-sequence turn-off for a population in the Galactic halo. This statement is enforced when looking at the color distribution of the field and globular clusters. The majority of the stars is located close to the turn-off for both, field and cluster stellar populations, and the rate of decrease towards red colors is similar. In addition, the minor peak seen at the

red side of the color distribution corresponds to a sample of red giant branch of the same population.

A first consequence of these results is the evidence of a probably common origin between GC and halo field stars, although our color distributions do not reveal the formation scenario. In particular, we can see here that field and clusters indicate that they may have been formed at the same time and in similar chemical environments. This supports the suspicions over the last years that the first star formation episodes were simultaneously (Bromm & Larson 2004).

Another consequence, probably more extreme, is that a significant number of stars in the Galactic halo were formed in GC's. Although simulations of the dynamical evolution of globular clusters is very complicated (D'Ercole et al. 2008; Baumgardt et al. 2008; Carretta et al. 2010), they do seem to reach to a common result: globular clusters lose stars. Observations of extratidal structures of GC's (Martínez Delgado et al. 2004; Law & Majewski 2010; Jordi & Grebel 2010) in the Galactic halo confirm this result. But the question of by how much are the field halo stars coming from disrupted GC is still under debate. Boley et al. (2009) and Baumgardt et al. (2008) for instance, suggested from numerical studies of galaxy formation that the halo could be constructed entirely from disrupted GC. From light-element abundance analyses of halo field stars Martell & Grebel (2010) concluded that up to 25% of the stars in the Galactic halo were formed originally in GC's while Carretta et al. (2010) concluded that a main component of the halo comes from globulars. A different conclusion is reached by Yong et al. (2008), who compared abundances of giants from disrupted globular clusters with the field. They did not find evidence of a large contribution of GC stars to the halo field. Recently, Jordi & Grebel (2010) using the same data set as this study (SDSS clusters and field stars) detected tidal features, which means that this particular sample of clusters is being evaporated into the Galactic halo. We are aware that the extra-tidal stars of these clusters contribute with a small fraction of the entire field halo population. But if the Galactic halo is being populated through tidal stripping of GC stars, then we would expect to see similar color distributions as we see here.

It is worthy to mention the case of NGC 4147. It shows a well defined color distribution as the field for [Fe/H]= -1.8, but shifted to the blue. The results of Dotter et al. (2010) reveal that this cluster has an age of 12.75 Gyr, which puts it in the frame of the normal old halo clusters. We found, however, that Meissner & Weiss (2006) can obtain an age of 9 Gyrs for this cluster.

Finally we want to remark that in Chap. 6 we could see how our sample of field stars is mainly formed from one coeval dominating population. Globular clusters are composed by stars with same age and metallicity, meaning that these observational evidence are consistent with this picture. In addition to that, we will see in the next section that these clusters are coeval within 1-2 Gyr as the field stars.

Cluster NGC	other	An09 [Fe/H]	Age (Gyr)	SW02 [Fe/H]	Age (Gyr)	D10 [Fe/H]	Age (Gyr)
4147	$\cdots$	$\cdots$	$\cdots$	$\cdots$	$\cdots$	-1.7	12.75 ± 0.75
5024	M53	$\cdots$	$\cdots$	$\cdots$	$\cdots$	-2.0	13.25 ± 0.5
5053	$\cdots$	$\cdots$	$\cdots$	-1.98	10.8 ± 0.9	-2.4	13.5 ± 0.75
5272	M3	-1.5	13.3 ± 1.4	-1.33	11.3 ± 0.7	-1.6	12.5 ± 0.5
5466	$\cdots$	$\cdots$	$\cdots$	-2.13	12.2 ± 0.9	-2.1	13.00 ± 0.75
5904	M5	-1.26	12.2 ± 1.3	-1.12	10.9 ± 1.1	-1.3	12.25 ± 0.75
6205	M13	-1.6	14.3 ± 1.1	-1.33	11.9 ± 1.1	-1.6	13.00 ± 0.5
6341	M92	-2.38	14.4 ± 0.9	-2.10	12.3 ± 0.9	-2.4	13.25 ± 1
7078	M15	-2.42	13.9 ± 2.5	-2.02	11.7 ± 0.8	-2.4	13.25 ± 1.0
7089	M2	$\cdots$	$\cdots$	$\cdots$	$\cdots$	-1.6	12.50 ± 0.75
$\cdots$	Pal 5	$\cdots$	$\cdots$	-1.47	10.0 ± 1.4	$\cdots$	$\cdots$

Table 7.2: Ages of our sample of globular clusters determined by three different authors: An et al. (2009, An09), Salaris & Weiss (2002, SW02) and Dotter et al. (2010, D10). For the metallicity and method adopted by the authors see text.

7.4   Globular clusters ages

From the observational evidence and implications discussed above that clusters and field stars may have originated in a similar way, it is logical to expect that the 11 GC studied here have ages according to the dominating halo population. We discussed in Chap. 6 the dependency of the absolute ages obtained only from the main-sequence turn-off. In particular, we saw that only the diffusion parameter can reduce the age by 4 Gyrs, but this result is again dependent on the stellar evolutionary models employed to determine ages. The age of globular clusters is much better constrained and we can use it to consolidate the ages for the MSTO field. Unfortunately, also for the absolute ages of GC there are many uncertainties that affect significantly the final results. On one side, there are still unclear issues in stellar evolution, such as the efficiency of atomic diffusion and the mixing length parameter in convection theory (Weiss 2002). On the other side, the observed quantities in the clusters need to be transformed to the calculated quantities of the models, introducing biases due to empirical color transformations. In addition, there is a scatter in the metallicity scale adopted for the clusters, which is an important quantity for the age-indicators.

Determination of GC ages (relative or absolute) are a challenge because globular clusters are old and reveal information about the early history of our Milky Way. Since they consist in many stars of the same age, metallicity and distance, they can be studied with better confidence than for individual field stars. Three broad used age indicators are *isochrone fitting*, $\Delta V(\text{TO} - \text{HB})$ and $\Delta(V - B)$:

- *Isochrone fitting*: The age given to the cluster is that of the isochrone that best fits the turn-off. Because this method depends on the position of the TO in the color magnitude diagram, the absolute ages can be affected by diffusion. Moreover, it needs an accurate distance of the cluster.

- $\Delta V(\text{TO} - \text{HB})$: This age indicator compares the observed difference in magnitude between the TO and the horizontal branch (HB) to that obtained from theoretical calculations. Although this method depends on reddening, it is the preferred one because the theoretical MSTO luminosity is a relatively well determined quantity in a theoretical point of view and also because it doesn't require an accurate distance estimation. Because the luminosity is less dependent on the properties of the envelope, the ages are not affected by diffusion significantly.

- $\Delta(V - B)$: This method compares the observed difference in color between the TO and the red giant branch to that obtained from theoretical isochrones. This relative difference has the advantage of being independent on distance and reddening, but can be very affected by diffusion.

For a detailed description of age indicators and their sensitiveness in atomic diffusion see Chaboyer et al. (1992a) and Meissner & Weiss (2006). We collected from literature for the ages for the clusters of Table 7.1, which were obtained by using the methods explained above. Those of An et al. (2009, hereafter An09), Salaris & Weiss (2002, hereafter SW02) and Dotter et al. (2010, hereafter D10) are indicated in Table 7.2, including the metallicity scale adopted by the authors. We explain each of them separately in the following, where we compare our results for the MSTO ages with the age as a function of metallicity obtained for each absolute scale.

7.4.1   An09 scale

Table 7.2 lists the metallicities and ages for the clusters of our sample used in An09. In their work they use the metallicity scales of Carretta & Gratton (1997, hereafter CG97) and Kraft & Ivans (2003, hereafter KI03) to determine ages and distances of the clusters. For this study we used only the KI03 ones in order to be consistent with the metallicity scale considered in Sect. 7.3. Their stellar evolutionary models are from the Yale Rotating Evolutionary Code (YREC Sills et al. 2000; Delahaye & Pinsonneault 2006). They derive the cluster ages by fitting isochrones to the CMD for the stars near the turn-off. This approach, like our determination of MSTO ages, is very dependent on atomic diffusion. A comparison of our MSTO age as a function of metallicity against the An09 scale can be seen in the panel A of Fig. 7.9. The red solid line corresponds to the ages for the MSTO of the field estimated with the Garstec isochrones (Weiss & Schlattl 2008) including diffusion, while the blue lines are the ages obtained without diffusion as described in Chap. 6.

There is a good agreement between the ages of the clusters and our field stars for the non-diffusive isochrones. This is expected, because the YREC models employed by An09 do not consider gravitational settling. Although some of the ages are higher than the age

of the Universe (13.7 Gyr, Bennett et al. 2003), they are still consistent with each other within the errors. Finally we see that the most metal-rich cluster is also the youngest one, suggesting a trend of an age-metallcity relation. We remind the reader to the discussion concerning the YREC isochrones in Sect. 6.3.1, where we saw that the Garstec and Yale models can differ severely, especially for young and metal-rich stars. Only five clusters are not enough to conclude if this small difference between the field and the An09 scale is due to the models employed or due to a real different age-metallicity relation.
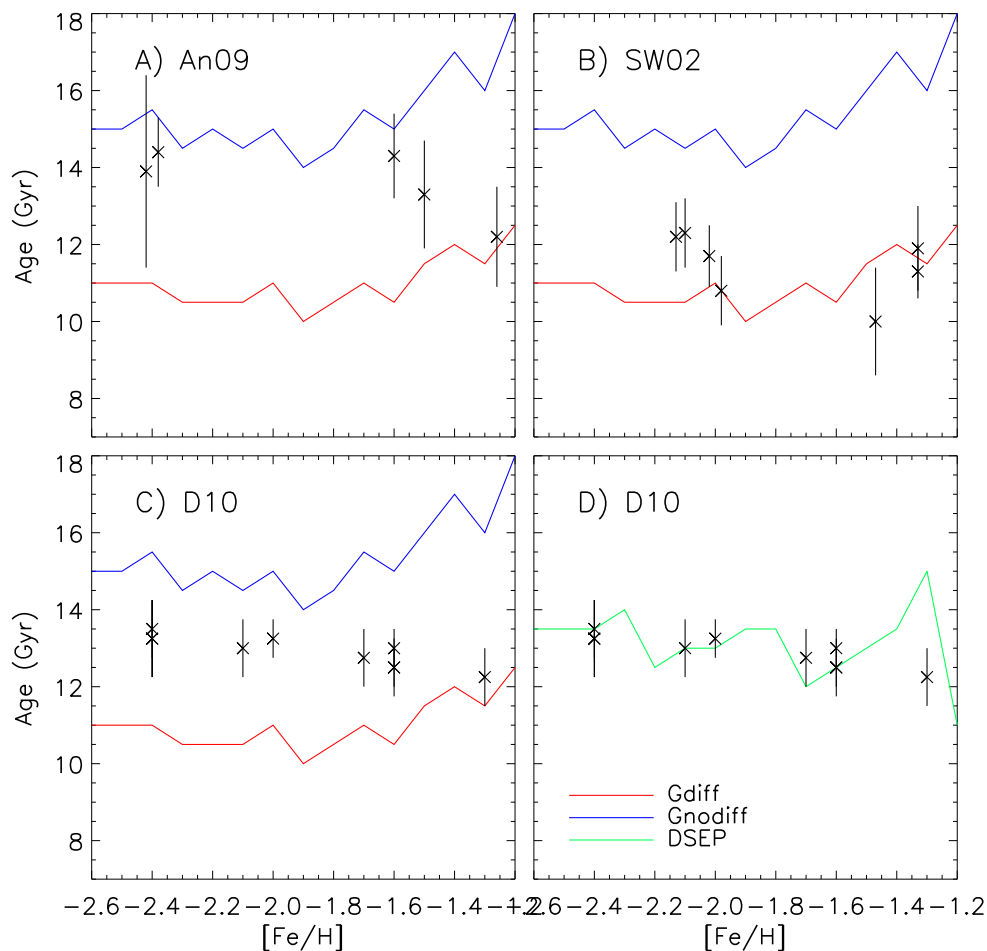
Figure 7.9: Panel A: The age as a function of [Fe/H] for the cluster sample of An et al. (2009) represented with asterisks. The red and black lines are the MSTO ages obtained for the field using isochrones with and without diffusion, respectively (see Chap. 6). Panel B: Same as panel A but with asterisks representing the ages and [Fe/H] of Salaris & Weiss (2002). Panel C: Same as panel A and B, plotting this time with asterisks the ages and [Fe/H] of Dotter et al. (2010). Panel D: Again D10 clusters but being compared with MSTO ages obtained using DSEP isochrones.

7.4.2   SW02 scale

Salaris & Weiss (2002) have determined homogeneously absolute ages for 55 clusters, from which those that overlap with our sample are labeled in Table 7.2 in the 5th and 6th column. The metallicity scale adopted here is that of Carretta & Gratton (1997, hereafter CG97). For Pal5 we considered the metallicity scale of Zinn & West (1984) because the CG97 one was more than 0.2 dex lower than the KI03 one, which is the scale adopted above for our color comparisons. To determine the age of the clusters, SW02 use a combination of the methods $\Delta V(\text{TO} - \text{HB})$ and $\Delta(V - I)$. They firstly divide the clusters in metallicity groups and choose for each group a reference cluster showing a well populated horizontal branch (HB). This allows a reliable determination of the brightness difference between the HB and the TO, and an absolute age can be determined accurately with $\Delta V(\text{TO} - \text{HB})$. Then the age of the other clusters were determined differentially with respect to the reference one by using the $\Delta(V - I)$ method.

They use their own isochrones performed with the Frascati RAphson Newton Evolutionary Code (FRANEC) as described in Salaris et al. (1997), which were transformed to clusters Johnson-Cousins UVI photometry. The isochrones do not include helium diffusion, but since the absolute reference ages were determined with the $\Delta V(\text{TO} - \text{HB})$ method, the results are unaffected by this assumption (see also Meissner & Weiss 2006, for a discussion of this age-dating method).

We have plotted in panel B of Fig. 7.9 the age and metallicity of the SW02 clusters of Table 7.2 with asterisks. The MSTO age is drawn as a function of metallicity for our field stars. For comparison as in panel A, our ages use the Garstec isochrones with and without atomic diffusion, illustrated with the red and blue lines, respectively. The GC ages lie in between our MSTO ones with a similar trend of the age as a function of metallicity. In the work of SW02, 55 clusters are included, and the authors do not find an age gradient at [Fe/H] < -1.2. Interestingly enough, we see how our final age using diffusive isochrones agrees well with the clusters, which are independent of diffusion. This can be interpreted as a further argument in favor of using diffusive isochrones in the age-determination of field population II stars.

7.4.3   D10 scale

The Advanced Camera for Survey's (ACS; Sarajedini et al. 2007) Wield-Field Channel on board of the Hubble Space Telescope targeted 65 clusters observed in the $F606W$ and $F814W$ photometric bands. Paper IX of the series of the ACS survey for globular clusters (Dotter et al. 2010) presents homogeneous absolute ages of these clusters. Those that overlap with our sample are labeled in the 7th and 8th column of Table 7.2, where the metallicity scale corresponds to that adopted by the Harris (1996) catalog, 2003 revision. The ages were determined with the isochrone that best fits the CMD in the region between the TO and the red giant branch. This method is a combination between *isochrone fitting* and $\Delta(V - B)$. The isochrones used are those from the Dartmouth Stellar Evolution Program (Dotter et al. 2007, 2008, DSEP).

Like our method to determine ages, the D10 method is also dependent on the MSTO color, and therefore on atomic diffusion. We expect to obtain agreements in the age-metallicity trend between our ages and those of D10. This can be seen in panel C of Fig. 7.9, were the age as a function of metallicity for the D10 clusters is displayed with asterisks. In panel C we have also plotted the MSTO ages obtained for the field stars, with the red line indicating the Garstec diffusive isochrones and the blue line the canonical ones. The trend is very similar, with the GC ages within our values. The absolute values are different, because the DSEP isochrones have a different treatment of atomic diffusion. They use the diffusion coefficients of Thoul et al. (1994), but inhibit settling in the outer region of the radiative core of $0.01 M_\odot$. In the outermost $0.005 M_\odot$ diffusion is completely stopped and in the $0.005 M_\odot$ below, diffusion has been linearly ramped from zero to the full effect (Dotter et al. 2008). Korn et al. (2006) observed diffusion of heavy elements by abundance analysis of metal-poor turn-off atmospheres and found evidence of internal mixing mechanisms that inhibit diffusion in these stars. There is still debate of which physical mechanisms drive these inhibitions. The method to inhibit diffusion employed by the DSEP evolutionary models has been meant only to satisfy consistently the observations of diffusion of Korn et al. (2006), but there is no physical argument to treat diffusion in this way. In fact, before Korn's observations, the same authors (Dotter et al. 2007) inhibited diffusion in the same way, but in the outer $0.1 M_\odot$, and claimed that like this they could satisfy the *lack* of observational evidence for diffusion in metal-poor stars, as found at that time by Gratton et al. (2001).
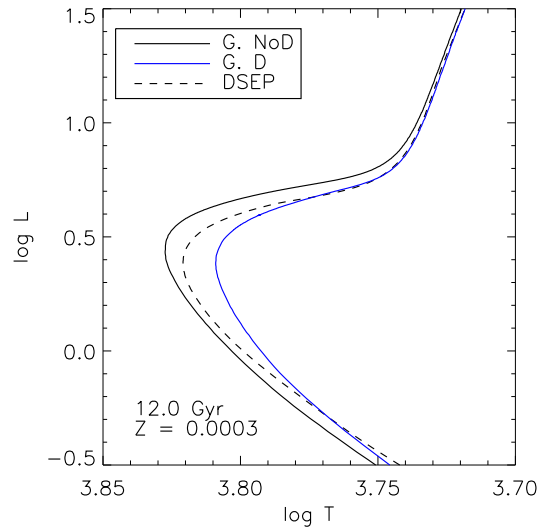

Figure 7.10: Comparison of Garstec and DSEP 11 Gyr isochrones with metal fraction of $Z = 3 \times 10^{-4}$. Solid lines correspond to Garstec isochrones fully- and non-diffusive isochrones, colored with blue and black, respectively. Dashed line corresponds to the DSEP one, which has an intermediate turn-off temperature and luminosity due to the partially-diffusion assumption.

The partial diffusion considered in the DSEP isochrones produces a MSTO temperature that is hotter than a fully GARSTEC diffusive isochrone and colder than a canonical one. This can be seen in Fig. 7.10, where we have plotted in the HR diagram isochrones of 12 Gyr and $Z = 0.0003$ obtained from the Garstec and DSEP evolutionary codes. Solid lines illustrate the Garstec isochrones, with the blue and black corresponding to the diffusive and canonical ones, respectively. The dashed line illustrates the DSEP isochrone, which MSTO lies in between the fully and zero Garstec isochrones, as expected.

We downloaded a set of isochrones from the DSEP database[4] and determined the MSTO age of our field stars as described in Chap. 6. The results are illustrated with the green line in panel D of Fig. 7.9, where we have also plotted the D10 ages for the globular clusters with asterisks. The agreement between clusters and field is excellent, which is expected because these clusters have similar TO colors as the field.

7.4.4   Discussion

We have adopted three different scales for ages and metallicities of 11 clusters to calibrate the MSTO age of the Galactic halo. We saw how the different scales show different results, where An09 yield relatively high ages in comparison with D10. This is expected, since An09 isochrones do not consider diffusion while D10 do, at least partially. As discussed extensively in Chap. 6, the inclusion of atomic diffusion in age determinations by using the MSTO temperature (or color) decreases the ages significantly. We saw an excellent agreement with the D10 scale and our MSTO ages agree if the same considerations about atomic diffusions are used. It should be noted the existence of an age spread or a gradient in the population of globular clusters is still under debate, some authors claim to see an age spread for [Fe/H] > −1.7 (De Angeli et al. 2005) while others for [Fe/H] > −1.2 (Salaris & Weiss 2002). The SW02 ages employ a very different method than An09, D10 and our own. It has the advantage of being independent of atomic diffusion, making them a more reliable calibration of absolute ages for the Galactic halo. It is encouraging to obtain a good agreement in the absolute scale given by the diffusive isochrones and these clusters. This reinforces our statement that the inner halo has an age of 10-12 Gyrs, where field and cluster stars were formed at the same time.

Note the result for the age of the field stars is in agreement with what was obtained by Schuster et al. (2006) and Allende Prieto et al. (2006), although they relied only in the turn-off color of isochrones that trace the cut-off represented by the MSTO of the field. The improvement given by the ages in this work is the careful study of globular clusters color properties and ages, which is used to consolidate the absolute age for the Galactic inner halo.

---

[4]http://stellar.dartmouth.edu/~models/

7.5   Summary and Conclusions

In this chapter we have studied 11 globular clusters observed with the SDSS telescopes, from which *ugriz* photometry was published in the web pages by An et al. (2008). To study these clusters in the frame of our field stars, we considered for the field the metallicities obtained with MAχ and the de-reddened $(g - r)$ colors taken from the SDSS databases.

After correcting the cluster photometry by extinction, we detected the turn-off using the Sobel Kernel method described in Sect. 5.2.2 for the field stars, which was adapted from temperature to colors. In some cases, the shape of the color magnitude diagrams of the clusters near the TO turned out to be too sparse or too narrow to detect the turn-off properly with the Sobel Kernel technique. For these clusters we used the TO-color given by the bluest point of the fiducial sequence of An et al. (2008).

We placed the turn-off as a function of metallicity of the clusters in a [Fe/H]-color diagram and compared this trend with the MSTO color found for the field stars. Considering the different de-reddening and photometry, we found an excellent agreement between them, with an offset smaller than the errors in the TO-determination. We then selected the field stars with the metallicity of the clusters and compared their color distribution with those of the clusters. The distributions were very similar, with the turn-off stars of the same color range for cluster and field. In addition, we found a second peak at red colors in the color distribution. We showed that this peak is the result of an accumulation in color of stars at the base of the red giant branch.

The color distribution and the TO-color as as function of metallicity are observational evidence of a common origin between cluster and field stars. This also fits well to the scenario that field and clusters consist on one dominating population. Based on the observations of tidal features of these clusters using SDSS data by Jordi & Grebel (2010), we discussed that if the halo was formed by disrupted globular clusters, then we would expect to observe similar color distributions between halo and field stars.

Motivated by the observational evidence, we used the GC ages from the literature to constrain our results. There was a scatter in the age-metallicity relations obtained by using the different metallicity scales and age-determination methods of An et al. (2009), Salaris & Weiss (2002) and Dotter et al. (2010). Even considering this scatter, we could see that the gradient and scale of the ages obtained by each method agreed relatively well with our own results. We could see that the clusters of each scale were coeval within 1-2 Gyr, as our field stars. We saw that the results obtained by Salaris & Weiss (2002) were robust under considerations of gravitational settling and that they agreed with our ages for the field using diffusive isochrones. This agreement consolidates the age of 11-12 Gyr given to the dominant halo population traced by the MSTO obtained in Chap. 6

Our absolute ages for the field stars agree with the results of Schuster et al. (2006) and Allende Prieto et al. (2006). The ages were firstly obtained based in the MSTO traced in [Fe/H] - T_{eff} diagrams (see Chap. 6 for details). The improvement in the age-determination here is that we have calibrated our results consistently on well studied properties in globular clusters. We finally conclude that the stars of the inner halo were formed 10-11 Gyr ago, with clusters and stars being coeval.

Chapter 8

Concluding Remarks

We have determined the age of the ancient Galactic halo by using a sample of field stars from the Sloan Digital Sky Survey (SDSS, York et al. 2000). The tasks performed during this work analyze and adapt ideas applied in different fields of astrophysics, and their combination allowed the age determination of halo field stars.

The first main task was to determine the stellar atmosphere parameters from the SDSS sample. The analysis of approximate 100,000 stellar spectra had to be efficient in order to obtain accurate parameters in a timely manner. In close collaboration with B. Panter, we created MAχ (Jofré et al. 2010), as a direct extension to the algorithm MOPED (Heavens et al. 2000; Panter et al. 2003). The MOPED method has shown an excellent performance in simultaneously and automatically estimating multiple parameters from SDSS galaxy spectra and medical images. Now MAχ is the new application to stellar spectra. The method is based on an intelligent compression procedure of the data, in which the information about the parameters in the data is not lost. The analysis of the compressed data produces an extreme speed-up in the parameter estimation.

As a second task, we determined the turn-off temperature for the Galactic halo, from which we could estimate the age of the halo stars. The turn-off was identified using a robust egde-detector kernel. This kernel has being used as the detector of the luminosity at the tip of the red giant branch estimate the distance of nearby galaxies (Lee et al. 1993; Tabur et al. 2009, and references therein). After examining our sample by color target selection, positions of the stars in the sky, quality in the parameter recovery and size of the stellar sample, we obtained the turn-off temperature as a function of metallicity. It could be ensured that this turn-off is unbiased by selection effects.

For the age determination, we used the temperature of the turn-off and the metallicity to find turn-off isochrones. We explored the effect of atomic diffusion in the resulting value for the ages and we found an absolute difference of 4 Gyr when using diffusive and canonical isochrones, respectively. Our results explain the age differences obtained over the years in the literature, where Schuster et al. (1996) and Unavane et al. (1996) obtained an age of $\sim 16 - 18$ Gyr and Schuster et al. (2006) obained a value of 13 Gyr for the age which

agrees better with our non-diffusive isochrones. Allende Prieto et al. (2006) obtained, on the other hand, ages of $\sim 10 - 12$ Gyr, in accordance with our diffusive isochrones. Given the current debate about the efficiency with which atomic diffusion acts in stellar interiors, our results show a strong argument against fully inhibited diffusion in metal-poor halo stars, because their ages would be larger than the age of the Universe. The isochrones employed for the age determination are well behaved in terms of diffusion, therefore we could give an age for the field stars of the Galactic halo of 10-12 Gyr.

The calibration of the absolute age for the Galactic halo was our third task. For that we considered the ages of globular clusters, for which the parameters can be better determined than for field stars. We found observational evidence that cluster and field stars share a similar history. For 11 clusters of An et al. (2008), which were also observed with the SDSS telescopes, we compared the color distributions to that of the field stars with the same metallicity value. We could see that both distributions agreed especially in the turn-off color as a function of metallicity. The agreement found between our ages for the field and those obtained by Salaris & Weiss (2002) for GCs serves as a consolidation of the fact that the Galactic inner halo is 10-12 Gyr old, with clusters and field stars formed at the same time.

Relevance of this thesis in Galactic astrophysics

The creation of tools and the scientific discussions are necessary to achieve a good understanding of the Universe. During this thesis we have contributed to the knowledge of the Milky Way by developing tools and discussing issues of Galactic formation.

We have developed a powerful tool, MAχ, which perfectly fits with the Galactic astronomy research of the modern era. There is currently a tremendous amount of activity in Europe and across the world related to spectroscopic surveys of the Milky Way Galaxy. RAVE (Steinmetz et al. 2006) and SEGUE are surveys that are on-going. The European Gaia mission (Perryman et al. 2001) will be launched in 2012, the Chinese LAMOST (Zhao et al. 2006), Australian HERMES (Wylie-de Boer & Freeman 2010) and American APOGEE (Allende Prieto et al. 2008a) will start in fall 2011. This will require a thorough knowledge of how to work with such a huge volume of spectroscopic data.

The effective temperature and metallicity obtained with MAχ were placed in a metallicity-temperature diagram. We could see that the majority of halo field stars from SDSS are part of a dominating coeval population. These stars belong to the inner halo, which are located at a distance where spectral observations is possible, i.e. metallicities and temperature estimates with MAχ are available. For the main-sequence turn-off given by the metallicity-temperature diagram, we could determine an age of 10-12 Gyr for the stars in the inner halo, having no gradient in the age-metallicity relation.

The results of this thesis can be summarized by Fig. 8.1, which illustrates a well-studied sample of halo field stars with metallicities and colors from Strömgren photometry (Schuster & Nissen 1988b; Schuster et al. 2006). The red line in Fig. 8.1 is our final result
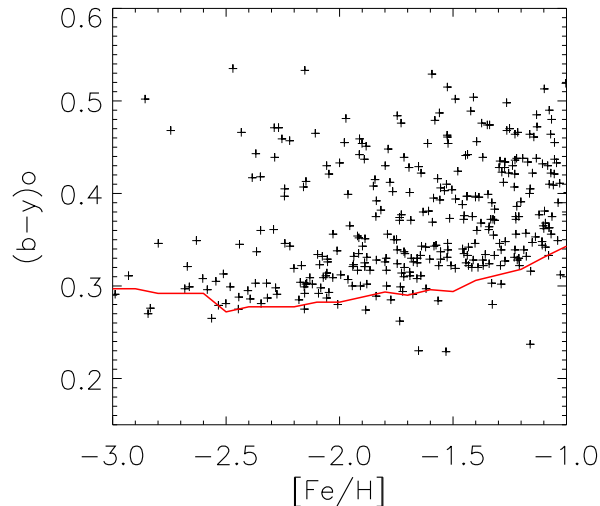
Figure 8.1: $(b - y) - [\mathrm{Fe/H}]$ diagram of the photometric sample of Schuster et al. (Salaris, priv. comm.). The red line corresponds to the MSTO determined from the SDSS sample as indicated in Appendix C and transformed to Strömgren photometry using the empirical relations of Ramírez & Meléndez (2005). There is a perfect agreement between the cut-off of SDSS and the $uvby - \beta$ samples.

for the turn-off $(b - y)$ color. It was transformed from the temperature detected for our SDSS sample using the temperatures and metallicities taken from their spectra using the MAχ method. We perfectly reproduce the cut-off of the Schuster sample, which implies that:

1. The SDSS low-resolution spectra contain valuable information about the metallicities and temperatures.

2. The MAχ method with our independent grid of synthetic spectra yield consistent stellar atmosphere parameters.

3. The Sobel Kernel edge-detector determines the hottest (or bluest) cut-off of the halo population well.

4. We have found the turn-off temperature as a function of metallicity of the Galactic halo, which is independent for the use of the SDSS or Schuster data set.

5. Based on the turn-off, the Galactic halo has an inner stellar population with an age of 10-12 Gyr.

A dominating population of 11-12 Gyr for the inner halo agrees with the current understanding of the formation of the Milky Way, which was formed rapidly during a collapse

of the proto-Galactic gas, where star formation took place 11-12 Gyr ago. The remaining stars in the halo formed at that time are those with low mass, because they take more time to evolve than the age of the Universe. This scenario supports the theory suggested by Eggen et al. (1962) and agrees with conclusions made from globular clusters (Sarajedini et al. 1997; Salaris & Weiss 2002; De Angeli et al. 2005; Dotter et al. 2010), where the metal-poor clusters are coeval. Note that the absolute ages obtained for the clusters by Salaris & Weiss (2002) are also 10-12 Gyr, which implies that GC's and field stars are coeval as well.

In Fig. 8.1 it is possible to observe a significant number of stars with bluer colors than the color cut-off, which were also seen in the rest of the SDSS [Fe/H] - T_{eff} diagrams of this thesis. These stars are referred to as blue metal-poor stars by Preston et al. (1994) and were later discussed by Preston & Sneden (2000). Furthermore, they have been noticed by Schuster et al. (2006, and references therein) and Unavane et al. (1996). An interesting explanation for them is that they were formed in small galaxies and have been accreted later on to the Milky Way halo. They experience a different star formation scenario than the Mikly Way and therefore are younger than the dominating population of the field stars. Further analyses on their kinematics and chemical abundances are necessary to prove this scenario. These blue stars and the existence of a dominant population of halo stars suggest that the two rivaling formation scenarios of the Galactic halo from Eggen et al. (1962) and Searle & Zinn (1978) actually complete in a composed manner the picture of how the Milky Way might have formed. Meaning that part of the halo has collapsed rapidly while the other part has been populated through collisions and mergers between the satellite galaxies and our Milky Way. These blue stars could also be blue stragglers of the same dominating field halo population. Detailed studies of these stars are crucial to quantify the ratio of accreted material and the rest of the dominating population.

In this thesis we have not only learned to develop useful tools in the current era of Galactic astrophysics using massive data sets. We have also learned to discuss fundamental problems of Galaxy formation and stellar evolution. A final conclusion of the thesis is that the majority of the Galactic inner halo stars are 10-12 Gyr old, where the field and clusters stars were formed rapidly at the same time.

Appendix A

The MAχ code

The implementation of the MAχ algorithm has been coded in the Interactive Data Language (IDL) programming environment. Although languages such as C++ and Fortran are perhaps quicker for some purposes and are free of license, IDL was chosen because it is easy to use and it contains many routines to analyze efficiently vectors and matrices, which are common in the MAχ algorithm.

Figure. A.1 shows a schematic plot of the MAχ core. The most relevant specific routines are explained with more detail below. In general terms, the scheme contains two main bodies, one at the left side working on the theoretical spectra and other at the right side assessing the observed spectra. Certain operations are done for both, model and data, which are indicated with boxes at the center of the diagram. In addition, the programs which make up the core of MAχ can be separated in three stages, which are separated with pointed lines in Fig. A.1: *Input*, where the initial values are defined; *preparation*, where the models and data are configured and the **b**$-$vectors and grid of $y-$numbers are calculated; and *fitting*, where the analysis is carried out and the atmosphere parameters are estimated.

A.0.1   Input

Two common blocks store the input values and are called in the routines of the core. The blocks define the properties of the parameter space and observed spectra, which are indicated with the grey boxes at the top of Fig. A.1.

- `common_grid.pro`: Creates the common block `GRID` containing the properties of the grid of models. The initial and final value of each parameter, including the step-size, create one array for each parameter. For example, if the initial and final effective temperature are 5500 K and 7000 K respectively, and the step-size is 250 K, then MAχ creates an array for the temperature as $T_{\text{eff}} = [5500, 5750, ..., 7000]$, which is stored as a common variable. Finally, the location of the synthetic spectra is indicated in this block.
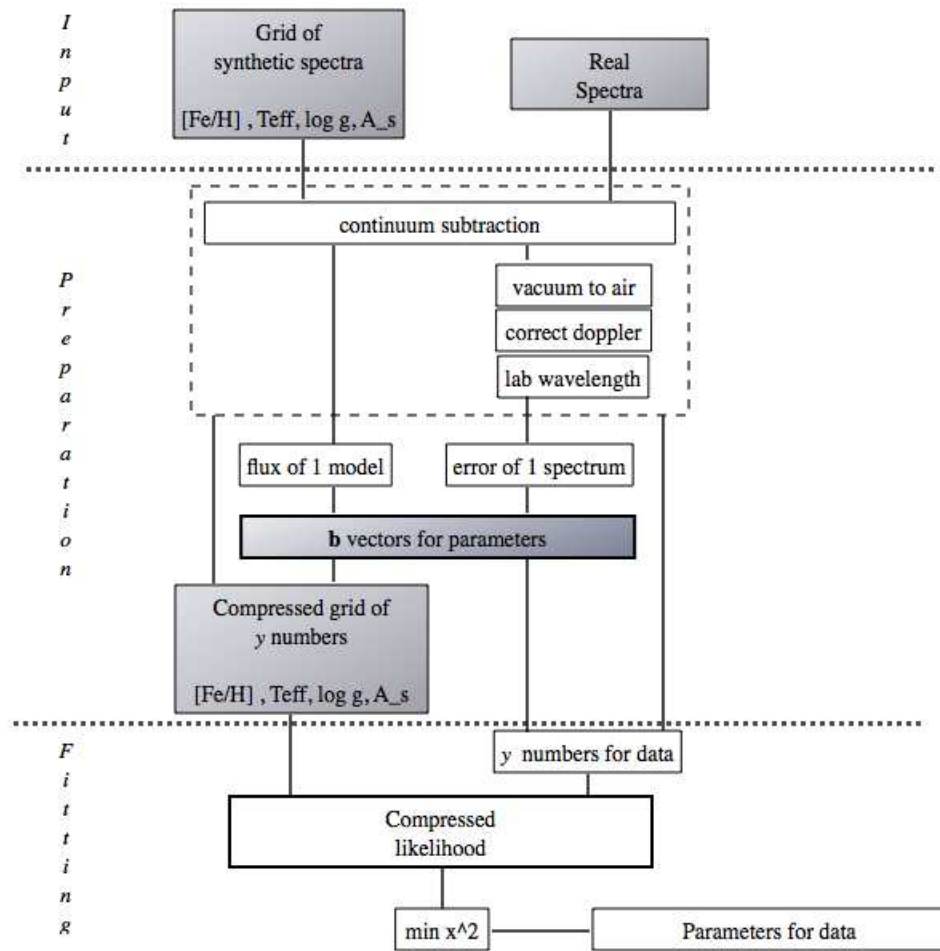
Figure A.1: Schematic diagram of the MAχ code. See text for the detailed explanation of the boxes.

- `common_numbers.pro`: Creates the common block `NUMBERS` containing the general quantities: The wavelength range for the analysis, which is written in an array with $2N_{win}$ elements, where N_{win} is the number of spectral windows. Another common variable is the array with the laboratory wavelength of the lines used for Doppler correction. The atmosphere parameters of the fiducial model for the **b**$-$vector calculation is defined in this block and finally, the location of the observed spectra.

A.0.2   Preparation

In this phase MAχ configures the spectra to an adequate environment for fitting (See Sect. 2.4.1). Once the spectra are configured, the **b**$-$vectors are created and the grid of synthetic spectra is compressed, which will be stored in a third common block.

Configuration of spectra

- `AP_rectification.pro`: The continuum subtraction box in Fig. A.1 is represented by this function and is used for model and data, The routine was kindly given by Carlos Allende Prieto (private communication) and its input are the order – in our case 6 – of the polynomial fit, number of fitting iteration and low and high rejection σ (see Sect. 3.4 for details). The output is an array with the continuum of the spectrum.

- `read_interp.pro`: Reads and configures a synthetic spectrum. Its input is the set of atmosphere parameters of the spectrum and returns the normalized spectrum in the wavelength range indicated at the block `NUMBERS`.

- `gauss_fit.pro`: Function that calculates the radial velocity of the observed star and correct its spectrum by Doppler effect. Its inputs are the spectral flux with its error, the wavelength range and the specific spectral line used to calculate the radial velocity. It fits a gaussian profile to the line and returns the minimum of the profile.

- `obsrest.pro`: The program was provided by Vivienne Wild (private communication) returns the new wavelength after the correction by Doppler effect. Its input are the redshift (or Doppler effect), flux, error and the old wavelength.

- `data_lab.pro`: Reads and configures the observed spectrum. Its steps are summarized by the operations indicated at the right side of the dashed box in Fig. A.1. With the observed wavelength, flux and its error it normalizes the spectrum, moves the wavelength from the vacuum to the air frame. It then finds the redshift to correct by Doppler and select wavelength range of interest by using the programs described above. Finally, it interpolates linearly the flux in order to have the wavelength array of the block `NUMBERS`. The output is an array with the normalized flux and error in the wavelength frame of the models.

Creation of weighting vectors and compressed grid

The creation of the **b**−vectors and y−grid happens after the dashed box in Fig.A.1 where the spectra were configured. The weighting vectors are needed to compress data and model, and are computed from a fiducial model and an observed noise. The box of the **b**−vectors is located at the center of the diagram and is grey, because the vectors are stored as a common block. These **b**−vectors are used to compute the y−grid, which is indicated also with a grey box as a common block for the fitting. The location of this box is at the left side in the diagram because it is related to the synthetic spectra. Details of the relevant programs that compute these quantities are below.

- `partial_derivatives.pro`: Calculates the dependence of the parameters in the spectral flux. The input is the set of atmosphere parameters ($\boldsymbol{\Theta}$) to read the spectrum. The derivative is calculated using the formula:

$$\frac{\partial \mathbf{F}}{\partial \theta_i} = \frac{\mathbf{F}(\theta_i) - \mathbf{F}(\theta_i - \Delta\theta_i)}{\Delta\theta_i} + \mathcal{O}(\Delta\theta_i^2) \tag{A.1}$$

  which is an approximation of the first derivative by final differencing. The routine reads the spectrum **F** and the neighbor spectra in the grid to compute partial derivatives for each parameter. It returns a matrix of $m \times N$, with $m = 4$ number of parameters and N number of data-points.

- `b_vector.pro`: Calculates the **b**−vectors for the parameters under study. The routine was written by Ben Panter and added to this code. Its inputs are the derivatives and inverse of the noise from an observed spectrum. We can use the noise of one spectrum only because all the spectra spectra have been observed with the same instrument, meaning that their error measurements – which depend strongly on the instrument – will have similar behaviors as a function of wavelength.

- `b_vector_calculation.pro`: Procedure to calculate the **b**−vectors, i.e. calculate derivatives and then the **b**−vectors itself. Its input are the atmosphere parameters of the fiducial model and its stores an array of $m \times N$ containing the **b**−vectors for the parameters.

- `y_vector.pro`: Creates the y−numbers, i.e. compresses the spectrum. As input needs the **b**−vectors and the spectral flux, which can be an observed or synthetic spectrum. Outputs a vector of m length with the components the y−numbers corresponding to each parameter.

- `create_y_grid.pro`: Performs the compression of the grid of synthetic spectra and saves it as a binary file.

A.0.3   Fitting

After the second dotted line in Fig. A.1, MAχ recovers parameters in the compressed space. To do so, it uses the **b**−vectors to calculate the y−numbers for the observed spectrum, indicated with the box at the right side in the schema of Fig. A.1. With these numbers and the compressed grid, MAχ computes the compressed likelihood, located in the center of the schema. The parameters that yield the maximum of the likelihood are given to the observed spectrum. The relevant programs that fit and recover parameters are explained below.

- `max2.pro`: MAχ core's main routine. It does not require inputs but needs the common blocks `GRID` and `NUMBERS`. This routine firstly restores the **b**−vectors and y−grid and puts them into a new common block `bY`. Then it defines a list of stars to be analyzed and enters to a loop through this list, printing as output the recovered parameters. The parameter recovery consists in several steps: reading the observed spectrum and preparing it for analysis as described in Sect.A.0.2, compressing the observed spectrum and creating a compressed likelihood. Finally, the parameters are those corresponding to the maximum point of the likelihood. For completeness, the full χ^2 is also computed for the best fit, which is printed out as well. The main subroutines that perform these steps are indicated below.

- `compress_chi2.pro`: Computes the compressed χ^2 for each y−grid point. The inputs are the configured observed spectrum and the local regions where the maximum should be looked at (See Sect. A.0.4). In the general case, the search of the maximum is free over the whole parameter space. The function first creates the y−vector for the observed spectrum and then computes using Eq. (2.6) the compressed χ^2. It saves in a binary file the compressed χ^2 for each y−grid point. The output is the position of the minimum χ^2 in the grid.

- `top_likelihood.pro`: The idea is to find a continuum parameter distribution and the position of the minimum χ^2 in the grid is the first step to find the maximum. This function finds the *real* maximum of the likelihood, which may not be at a grid point. With the position of the minimum χ^2 in the y−grid and the observed spectrum, MAχ moves to the full data set, where the full classical χ^2 is calculated for this particular point in the grid of synthetic spectra. It fits a parabola with the χ^2 of the minimum and the two neighbors for each parameter. The minimum of the parabola is thus interpreted as the *real* maximum of the likelihood and the interpolated values of the parameters for this minimum are the output of the function. For error calculation, see below.

A.0.4   Optional routines and flags

MAχ has routines and flags that are very useful for certain purposes and therefore it is worthy to list them. They are not necessary to recover parameters, therefore they are not included in the schema in Fig. A.1.

- `plot_results.pro`: If a visual check of the spectra is required, then this routine can be used to produce the best synthetic spectral fit to the spectrum, reconstructed from the parameters extracted by MAχ.

- `compressed_chi2.pro`: The computation of the compressed χ^2 has the option to fix certain parameter (see Sect. 4.5.2). This is done by using additional flags, which set the position of the parameter array where the fix value is located. For example, `pos_max = compressed_chi2(F0, T=5)` computes the χ^2 for the spectrum `F0` and the grid of models in the direction where $T_{\text{eff}} = \texttt{teff}(5) = 6250$ K only.

- `top_likelihood.pro`: The error calculation is done with a linear interpolation between the two points at the region where the value of $\chi^2 = \chi^2_{min} + \Delta\chi^2$ is located in the direction of each parameter as discussed in Sect. 2.4.3. The error calculation is optional because it slows down the parameter recovery and an additional flag of unity must be set in case that one wants to calculate the errors.

Appendix B

High-resolution tables

wavelength ($\AA$)	$\log gf$
FeI	
6136.62	-1.410
6137.69	-1.403
6191.56	-1.416
6219.28	-2.448
6230.72	-1.281
6246.32	-0.877
6252.56	-1.767
6265.13	-2.540
6335.33	-2.177
6336.82	-0.856
6393.60	-1.576
6411.65	-0.717
6430.85	-1.946
6494.98	-1.239
6592.91	-1.473
6677.99	-1.418
FeII	
6084.11	-3.881
6149.26	-2.724
6238.39	-2.754
6247.56	-2.329
6416.92	-2.877
6432.68	-3.501

Table B.1: FeI and II lines used for the high-resolution fits. The first column indicates the wavelength and the second the $\log gf$ value (see Chap. 4)

star	MAχ, free			MAχ, restr.			classical, EW			
	$T_{\rm eff}$ (K)	$\log g$	[Fe/H]	$T_{\rm eff}$ (K)	$\log g$	[Fe/H]	$T_{\rm eff}$ (K)	$\log g$	[Fe/H]	v_t (km/s)
HD3567	6103.5	4.79	-1.200	6176.0	4.20	-1.223	6035.0	4.08	-1.200	1.50
HD19445	–	–	–	5746.5	4.10	-2.293	5982.0	4.38	-2.075	1.40
HD22879	5770.6	4.31	-0.877	5778.1	4.31	-0.880	5792.0	4.29	-0.885	1.20
HD25704	5638.9	3.61	-1.094	5864.4	4.19	-0.912	5700.0	4.18	-1.010	1.00
HD63077	5795.5	4.21	-0.796	5787.7	4.21	-0.793	5629.0	4.15	-0.935	0.90
HD63598	6078.6	4.79	-0.681	5804.1	4.23	-0.901	5680.0	4.16	-0.885	0.90
HD97320	5601.1	4.65	-1.411	6025.1	4.24	-1.183	6105.0	4.18	-1.175	1.20
HD103723	5999.2	4.29	-0.896	6004.4	4.29	-0.896	6128.0	4.28	-0.805	1.50
HD105004	5802.5	4.33	-0.900	5802.5	4.33	-0.900	5900.0	4.30	-0.800	1.10
HD106038	5994.6	4.48	-1.392	5995.5	4.48	-1.392	5950.0	4.33	-1.390	1.10
HD113679	6037.3	4.73	-0.500	5757.5	4.35	-0.708	5759.0	4.04	-0.590	0.90
HD116064	5757.7	4.58	-2.41	5757.7	4.58	-2.401	5999.0	4.33	-2.000	1.50
HD121004	5509.2	4.05	-0.670	5657.8	4.40	-0.650	5711.0	4.46	-0.725	0.65
HD122196	5811.8	3.50	-1.954	5810.2	3.56	-1.954	6048.0	3.89	-1.760	1.20
HD126681	5556.9	4.44	-1.055	5521.6	4.68	-1.075	5532.0	4.58	-1.170	0.60
HD160617	5804.1	3.50	-1.961	5985.2	3.75	-1.794	6028.0	3.79	-1.785	1.30
HD175179	6080.5	5.00	-0.500	5779.5	4.47	-0.691	5758.0	4.16	-0.690	0.90
HD188510	5568.8	4.35	-1.341	5500.0	4.65	-1.231	5536.0	4.63	-1.600	1.00
HD189558	5610.8	3.58	-1.191	5500.0	3.75	-1.181	5712.0	3.79	-1.145	1.20
HD195633	6318.2	4.61	-0.500	6037.7	3.99	-0.687	6005.0	3.86	-0.625	1.40
HD205650	5693.7	4.93	-1.195	5754.0	4.47	-1.208	5842.0	4.49	-1.170	0.90
HD298986	5891.5	3.66	-1.592	6297.9	4.22	-1.304	6144.0	4.18	-1.410	1.40
CD-333337	5808.2	3.66	-1.598	5946.9	3.85	-1.490	5952.0	3.95	-1.435	1.40
CD-453283	5500.0	4.26	-0.978	5885.5	5.00	-0.685	5657.0	4.97	-0.835	0.80
CD-571633	5939.9	4.37	-0.893	5939.9	4.37	-0.893	5907.0	4.26	-0.930	1.10
CD-3018140	6143.1	3.50	-2.095	6246.5	3.50	-1.980	6340.0	4.13	-1.870	1.00
G005-040	6228.2	5.00	-0.584	5930.4	4.52	-0.794	5766.0	4.23	-0.840	0.80
G013-009	6529.5	4.58	-2.29	6556.0	4.08	-2.299	6416.0	3.95	-2.225	1.40

Table B.2: Parameters of the stars (Col 1) obtained with MAχ for both types of analysis discussed in the text. In the first analysis all three parameters are determined with only the spectrum, while in the second one $\log g$ was determined independently by using parallaxes according to Eq. (14), as for the classical method (EW; last four columns)

Appendix C

MSTO temperature for field halo stars

[Fe/H]	$T_{\mathrm{eff,TO}}$ (K)	σ_{TO} (K)
-3.00	6665.22	142.69
-2.90	6669.42	114.37
-2.80	6669.72	89.51
-2.70	6666.14	68.11
-2.60	6658.66	50.18
-2.50	6647.29	35.71
-2.40	6632.03	24.70
-2.30	6612.88	17.15
-2.20	6589.84	13.07
-2.10	6562.90	12.44
-2.00	6532.08	15.28
-1.90	6497.36	21.58
-1.80	6458.75	31.35
-1.70	6416.25	44.57
-1.60	6369.86	61.26
-1.50	6319.58	81.41
-1.40	6265.41	105.02
-1.30	6207.34	132.09
-1.20	6145.38	162.63

Table C.1: Final value of the turn-off temperature given by the field halo stars of SDSS. Atmosphere parameters were estimated with MAχ . The determination of the turn-off was done using the Sobel Kernel edge-detector technique using a sample of 100,000 stars. The errors correspond to the 3σ values from bootstrapping 500 times the stellar sample. For details see Chap. 5

Appendix D

Ages for the Galactic halo stars

[Fe/H]	$\mathrm{Age_{diff}}$ (Gyr)	$\mathrm{Age_{nodiff}}$ (Gyr)
-3.0	12.5 ± 1.5	17.5 ± 1.5
-2.9	12.0 ± 1.5	17.0 ± 1.5
-2.8	10.5 ± 0.75	14.5 ± 1.25
-2.7	11.0 ± 0.75	14.5 ± 1.25
-2.6	11.0 ± 0.25	15.0 ± 0.75
-2.5	11.0 ± 0.25	15.0 ± 0.5
-2.4	11.0 ± 0.25	15.5 ± 0.25
-2.3	10.5 ± 0.25	14.5 ± 0.25
-2.2	10.5 ± 0.25	15.0 ± 0.25
-2.1	10.5 ± 0.25	14.5 ± 0.25
-2.0	11.0 ± 0.25	15.0 ± 0.25
-1.9	10.0 ± 0.25	14.0 ± 0.5
-1.8	10.5 ± 0.5	14.5 ± 0.75
-1.7	11.0 ± 0.5	15.0 ± 1.00
-1.6	10.5 ± 0.75	15.0 ± 1.50
-1.5	11.5 ± 1.5	16.0 ± 2.00
-1.4	12.0 ± 2.0	17.0 ± 1.50
-1.3	11.5 ± 2.75	16.0 ± 2.75
-1.2	12.5 ± 3.75	18 ± 2.5

Table D.1: MSTO ages for different metallicity and turn-off temperature values obtained in Chap. 5. Garstec isochrones with and without atomic diffusion are considered (see Chap. 6). For the errors, only the uncertainties of the bootstrapping of the turn-off detection is considered.

Bibliography

Abazajian, K., Adelman-McCarthy, J. K., Agüeros, M. A., et al. 2004, AJ, 128, 502

Abazajian et al., K. N. 2009, ApJS, 182, 543

Allende Prieto, C., Majewski, S. R., Schiavon, R., et al. 2008a, Astronomische Nachrichten, 329, 1018

Allende Prieto, C., Sivarani, T., Beers, T. C., et al. 2008b, AJ, 136, 2070

Allende Prieto et al., C. 2006, ApJ, 636, 804

Alonso, A., Arribas, S., & Martinez-Roger, C. 1996, A&A, 313, 873

An, D., Johnson, J. A., Clem, J. L., et al. 2008, ApJS, 179, 326

An, D., Pinsonneault, M. H., Masseron, T., et al. 2009, ApJ, 700, 523

Asplund, M. 2005, ARA&A, 43, 481

Babu, G. J. & Feigelson, E. D. 1996, Astrostatistics, ed. Babu, G. J. & Feigelson, E. D.

Ballot, J., García, R. A., & Lambert, P. 2006, MNRAS, 369, 1281

Barklem, P. S. & Aspelund-Johansson, J. 2005, A&A, 435, 373

Baumgardt, H., Kroupa, P., & Parmentier, G. 2008, MNRAS, 384, 1231

Beers, T. C., Chiba, M., Yoshii, Y., et al. 2000, AJ, 119, 2866

Beers, T. C., Preston, G. W., & Shectman, S. A. 1985, AJ, 90, 2089

Beers, T. C., Preston, G. W., & Shectman, S. A. 1992, AJ, 103, 1987

Beers, T. C., Rossi, S., Norris, J. E., Ryan, S. G., & Shefler, T. 1999, AJ, 117, 981

Belokurov, V., Zucker, D. B., Evans, N. W., et al. 2006, ApJL, 647, L111

Bennett, C. L., Halpern, M., Hinshaw, G., et al. 2003, ApJS, 148, 1

Bensby, T., Zenn, A. R., Oey, M. S., & Feltzing, S. 2007, ApJL, 663, L13

Bergbusch, P. A. & Vandenberg, D. A. 1992, ApJS, 81, 163

Bergbusch, P. A. & VandenBerg, D. A. 2001, ApJ, 556, 322

Bessell, M. S. 2005, ARA&A, 43, 293

Böhm-Vitense, E. 1989, Introduction to stellar astrophysics. Vol. 2. Stellar atmospheres., ed. Böhm-Vitense, E.

Boley, A. C., Lake, G., Read, J., & Teyssier, R. 2009, ApJL, 706, L192

Bond, J. R. 1995, Physical Review Letters, 74, 4369

Bond, N. A., Ivezić, Ž., Sesar, B., et al. 2010, ApJ, 716, 1

Bromm, V. & Larson, R. B. 2004, ARA%A, 42, 79

Brun, A. S., Turck-Chièze, S., & Zahn, J. P. 1999, ApJ, 525, 1032

Carney, B. W., Latham, D. W., & Laird, J. B. 2005, AJ, 129, 466

Carney, B. W., Latham, D. W., Laird, J. B., & Aguilar, L. A. 1994, AJ, 107, 2240

Carollo, D., Beers, T. C., Chiba, M., et al. 2010, ApJ, 712, 692

Carollo, D., Beers, T. C., Lee, Y. S., et al. 2007, Nature, 450, 1020

Carretta, E., Bragaglia, A., Gratton, R. G., et al. 2010, A&A, 516, A55+

Carretta, E. & Gratton, R. G. 1997, A&AS, 121, 95

Carroll, B. W. & Ostlie, D. A. 2006, An introduction to modern astrophysics and cosmology, ed. Carroll, B. W. & Ostlie, D. A.

Casagrande, L., Flynn, C., Portinari, L., Girardi, L., & Jimenez, R. 2007, MNRAS, 382, 1516

Cassisi, S., Castellani, V., degl'Innocenti, S., & Weiss, A. 1998, A&AS, 129, 267

Cassisi, S., Salaris, M., Castelli, F., & Pietrinferni, A. 2004, ApJ, 616, 498

Castelli, F. 2005, Memorie della Societa Astronomica Italiana Supplementi, 8, 25

Castelli, F. & Kurucz, R. L. 2003, in IAU Symposium, Vol. 210, Modelling of Stellar Atmospheres, ed. N. Piskunov, W. W. Weiss, & D. F. Gray, 20P–+

Chaboyer, B. 2007, in EAS Publications Series, Vol. 26, EAS Publications Series, ed. C. W. Straka, Y. Lebreton, & M. J. P. F. G. Monteiro, 17–23

Chaboyer, B., Deliyannis, C. P., Demarque, P., Pinsonneault, M. H., & Sarajedini, A. 1992a, ApJ, 388, 372

Chaboyer, B., Demarque, P., Kernan, P. J., Krauss, L. M., & Sarajedini, A. 1996, MNRAS, 283, 683

Chaboyer, B., Fenton, W. H., Nelan, J. E., Patnaude, D. J., & Simon, F. E. 2001, ApJ, 562, 521

Chaboyer, B., Sarajedini, A., & Demarque, P. 1992b, ApJ, 394, 515

Christensen-Dalsgaard, J., Proffitt, C. R., & Thompson, M. J. 1993, ApJL, 403, L75

Christlieb, N., Bessell, M. S., Beers, T. C., et al. 2002, Nature, 419, 904

Christlieb, N., Wisotzki, L., Reimers, D., et al. 2001, A&A, 366, 898

Chun, S., Kim, J., Sohn, S. T., et al. 2010, AJ, 139, 606

Collet, R., Asplund, M., & Thévenin, F. 2005, A&A, 442, 643

Crane, P. & Banse, K. 1982, Memorie della Societa Astronomica Italiana, 53, 19

Croswell, K., Latham, D. W., Carney, B. W., Schuster, W., & Aguilar, L. 1991, AJ, 101, 2078

De Angeli, F., Piotto, G., Cassisi, S., et al. 2005, AJ, 130, 116

de Jong, J. T. A., Yanny, B., Rix, H., et al. 2010, ApJ, 714, 663

Dekker, H., D'Odorico, S., Kaufer, A., Delabre, B., & Kotzlowski, H. 2000, in Society of Photo-Optical Instrumentation Engineers (SPIE) Conference Series, Vol. 4008, Society of Photo-Optical Instrumentation Engineers (SPIE) Conference Series, ed. M. Iye & A. F. Moorwood, 534–545

Delahaye, F. & Pinsonneault, M. H. 2006, ApJ, 649, 529

Demarque, P., Guenther, D. B., Li, L. H., Mazumdar, A., & Straka, C. W. 2008, Ap&SS, 316, 31

Demarque, P., Woo, J., Kim, Y., & Yi, S. K. 2004, ApJS, 155, 667

D'Ercole, A., Vesperini, E., D'Antona, F., McMillan, S. L. W., & Recchi, S. 2008, MNRAS, 391, 825

Dotter, A., Chaboyer, B., Jevremović, D., et al. 2007, AJ, 134, 376

Dotter, A., Chaboyer, B., Jevremović, D., et al. 2008, ApJS, 178, 89

Dotter, A., Sarajedini, A., Anderson, J., et al. 2010, ApJ, 708, 698

Eggen, O. J., Lynden-Bell, D., & Sandage, A. R. 1962, ApJ, 136, 748

ESA. 1997, VizieR Online Data Catalog, 1239, 0

Finlator, K., Ivezić, Ž., Fan, X., et al. 2000, AJ, 120, 2615

Fisher, R. A. 1935, J. Roy. Stat. Soc., 98, 39

François, P., Depagne, E., Hill, V., et al. 2007, A&A, 476, 935

Fuhrmann, K. 1998, A&A, 338, 161

Fukugita, M., Ichikawa, T., Gunn, J. E., et al. 1996, AJ, 111, 1748

Gilmore, G., Wyse, R. F. G., & Kuijken, K. 1989, ARA&A, 27, 555

Girardi, L., Grebel, E. K., Odenkirchen, M., & Chiosi, C. 2004, A&A, 422, 205

Gratton, R., Sneden, C., & Carretta, E. 2004, ARA%A, 42, 385

Gratton, R. G., Bonifacio, P., Bragaglia, A., et al. 2001, A&A, 369, 87

Gratton, R. G., Fusi Pecci, F., Carretta, E., et al. 1997, ApJ, 491, 749

Gray, D. F. 1992, The observation and analysis of stellar photospheres., ed. D. F. Gray

Gray, R. O. & Corbally, C. J. 1994, AJ, 107, 742

Gray, R. O., Graham, P. W., & Hoyt, S. R. 2001, AJ, 121, 2159

Green, E. M., Demarque, P., & King, C. R. 1987, The revised Yale isochrones and luminosity functions, ed. Green, E. M., Demarque, P., & King, C. R.

Grevesse, N. & Noels, A. 1993, Physica Scripta Volume T, 47, 133

Grevesse, N. & Sauval, A. J. 1998, Space Science Reviews, 85, 161

Griffin, R. F. 1967, ApJ, 148, 465

Gunn, J. E., Siegmund, W. A., Mannery, E. J., et al. 2006, AJ, 131, 2332

Gustafsson, B., Edvardsson, B., Eriksson, K., et al. 2008, A&A, 486, 951

Gustafsson, B. & Mizuno-Wiedner, M. 2001, in Astronomical Society of the Pacific Conference Series, Vol. 245, Astrophysical Ages and Times Scales, ed. T. von Hippel, C. Simpson, & N. Manset, 271–+

Hansen, C. J. & Kawaler, S. D. 1994, Stellar Interiors. Physical Principles, Structure, and Evolution., ed. Hansen, C. J. & Kawaler, S. D.

Harris, W. E. 1996, AJ, 112, 1487

Heavens, A. 2009, in Lecture Notes in Physics, Berlin Springer Verlag, Vol. 665, Data Analysis in Cosmology, ed. V. J. Martinez, E. Saar, E. M. Gonzales, & M. J. Pons-Borderia , 51–+

Heavens, A. F., Jimenez, R., & Lahav, O. 2000, MNRAS, 317, 965

Helmi, A. 2008, A&AR, 15, 145

Helmi, A., Ivezić, Ž., Prada, F., et al. 2003, ApJ, 586, 195

Ibata, R. A., Gilmore, G., & Irwin, M. J. 1994, Nature, 370, 194

Iben, Jr., I. 1967, ARA&A, 5, 571

Ivezić, Ž., Sesar, B., Jurić, M., et al. 2008, ApJ, 684, 287

Jofré, P., Panter, B., Hansen, C. J., & Weiss, A. 2010, A&A, 517, A57+

Jonsell, K., Edvardsson, B., Gustafsson, B., et al. 2005, A&A, 440, 321

Jordi, K. & Grebel, E. K. 2010, ArXiv e-prints

Jurić, M., Ivezić, Ž., Brooks, A., et al. 2008, ApJ, 673, 864

Kapteyn, J. C. & van Rhijn, P. J. 1920, ApJ, 52, 23

Karhunen, K. 1947, Über lineare methoden in der Wahrscheinlichkeitsrechnung., ed. K. Karhunen

Kippenhahn, R. & Weigert, A. 1990, Stellar Structure and Evolution, ed. Kippenhahn, R. & Weigert, A.

Korn, A. J. 2008, in Astronomical Society of the Pacific Conference Series, Vol. 384, 14th Cambridge Workshop on Cool Stars, Stellar Systems, and the Sun, ed. G. van Belle, 33–+

Korn, A. J., Grundahl, F., Richard, O., et al. 2006, Nature, 442, 657

Kraft, R. P. & Ivans, I. I. 2003, PASP, 115, 143

Kupka, F. G., Ryabchikova, T. A., Piskunov, N. E., Stempels, H. C., & Weiss, W. W. 2000, Baltic Astronomy, 9, 590

Kurucz, R. L. 1992, Revista Mexicana de Astronomia y Astrofisica, vol. 23, 23, 45

Kurucz, R. L. 2005, Memorie della Societa Astronomica Italiana Supplementi, 8, 14

Law, D. R. & Majewski, S. R. 2010, ApJ, 718, 1128

Lee, M. G., Freedman, W. L., & Madore, B. F. 1993, ApJ, 417, 553

Lee, Y., Joo, S., Han, S., et al. 2005, ApJL, 621, L57

Lee, Y. S., Beers, T. C., Sivarani, T., et al. 2008a, AJ, 136, 2022

Lee, Y. S., Beers, T. C., Sivarani, T., et al. 2008b, AJ, 136, 2050

Lenz, D. D., Newberg, J., Rosner, R., Richards, G. T., & Stoughton, C. 1998, ApJS, 119, 121

Lind, K., Korn, A. J., Barklem, P. S., & Grundahl, F. 2008, A&A, 490, 777

Lucatello, S., Beers, T. C., Christlieb, N., et al. 2006, ApJ, 652, L37

Madore, B. F. & Freedman, W. L. 1995, AJ, 109, 1645

Majewski, S. R. 1993, ARA&A, 31, 575

Marquez, A. & Schuster, W. J. 1994, A&AS, 108, 341

Marsteller, B., Beers, T. C., Thirupathi, S., et al. 2009, AJ, 138, 533

Martell, S. L. & Grebel, E. K. 2010, ArXiv e-prints

Martínez Delgado, D., Dinescu, D. I., Zinn, R., et al. 2004, in Astronomical Society of the Pacific Conference Series, Vol. 327, Satellites and Tidal Streams, ed. F. Prada, D. Martinez Delgado, & T. J. Mahoney, 255–+

McCall, M. L. 2004, AJ, 128, 2144

Meissner, F. & Weiss, A. 2006, A&A, 456, 1085

Méndez, B., Davis, M., Moustakas, J., et al. 2002, AJ, 124, 213

Morel, P. & Thévenin, F. 2002, A&A, 390, 611

Morrison, H. L., Mateo, M., Olszewski, E. W., et al. 2000, AJ, 119, 2254

Nelder, J. A. & Mead, R. 1965, Comput. J., 7, 308

Newberg, H. J., Yanny, B., Cole, N., et al. 2007, ApJ, 668, 221

Nissen, P. E., Chen, Y. Q., Asplund, M., & Pettini, M. 2004, A&A, 415, 993

Nissen, P. E., Hoeg, E., & Schuster, W. J. 1997, in ESA Special Publication, Vol. 402, Hipparcos - Venice '97, 225–230

Nissen, P. E., Primas, F., Asplund, M., & Lambert, D. L. 2002, A&A, 390, 235

Noerdlinger, P. D. & Arigo, R. J. 1980, ApJL, 237, L15+

Nordström, B., Mayor, M., Andersen, J., et al. 2004, A&A, 418, 989

Norris, J. E. 2004, ApJL, 612, L25

Odenkirchen, M. & Grebel, E. K. 2004, in Astronomical Society of the Pacific Conference Series, Vol. 327, Satellites and Tidal Streams, ed. F. Prada, D. Martinez Delgado, & T. J. Mahoney, 284–+

Panter, B., Heavens, A. F., & Jimenez, R. 2003, MNRAS, 343, 1145

Pearson, K. 1900, Philosophical Magazine, 50, 157

Perryman, M. A. C., de Boer, K. S., Gilmore, G., et al. 2001, A&A, 369, 339

Pinsonneault, M. H., Steigman, G., Walker, T. P., & Narayanan, V. K. 2002, ApJ, 574, 398

Pont, F. & Eyer, L. 2004, MNRAS, 351, 487

Press, W. H. 1993, Science, 259, 1931

Preston, G. W., Beers, T. C., & Shectman, S. A. 1994, AJ, 108, 538

Preston, G. W. & Sneden, C. 2000, AJ, 120, 1014

Prialnik, D. 2000, An Introduction to the Theory of Stellar Structure and Evolution, ed. Prialnik, D.

Proffitt, C. R. & Vandenberg, D. A. 1991, ApJS, 77, 473

Ramírez, I. & Meléndez, J. 2005, ApJ, 626, 465

Re Fiorentin, P., Bailer-Jones, C. A. L., Lee, Y. S., et al. 2007, A&A, 467, 1373

Recio-Blanco, A., Bijaoui, A., & de Laverny, P. 2006, MNRAS, 370, 141

Rockosi, C., Beers, T. C., Majewski, S., Schiavon, R., & Eisenstein, D. 2009, in Astronomy, Vol. 2010, AGB Stars and Related Phenomenastro2010: The Astronomy and Astrophysics Decadal Survey, 14–+

Rowan-Robinson, M. 1985, The cosmological distance ladder: Distance and time in the universe, ed. Rowan-Robinson, M.

Sakai, S., Madore, B. F., & Freedman, W. L. 1996, ApJ, 461, 713

Salaris, M., Cassisi, S., & Weiss, A. 2002, PASP, 114, 375

Salaris, M., degl'Innocenti, S., & Weiss, A. 1997, ApJ, 479, 665

Salaris, M., Groenewegen, M. A. T., & Weiss, A. 2000, A&A, 355, 299

Salaris, M. & Weiss, A. 1998, A&A, 335, 943

Salaris, M. & Weiss, A. 2001a, A&A, 376, 955

Salaris, M. & Weiss, A. 2001b, in Astronomical Society of the Pacific Conference Series, Vol. 245, Astrophysical Ages and Times Scales, ed. T. von Hippel, C. Simpson, & N. Manset, 367–+

Salaris, M. & Weiss, A. 2002, A&A, 388, 492

Salasnich, B., Girardi, L., Weiss, A., & Chiosi, C. 2000, A&A, 361, 1023

Sandage, A. 1993, AJ, 106, 719

Sarajedini, A., Bedin, L. R., Chaboyer, B., et al. 2007, AJ, 133, 1658

Sarajedini, A., Chaboyer, B., & Demarque, P. 1997, PASP, 109, 1321

Sbordone, L. 2005, Memorie della Societa Astronomica Italiana Supplementi, 8, 61

Schlegel, D. J., Finkbeiner, D. P., & Davis, M. 1998, ApJ, 500, 525

Schönrich, R. & Binney, J. 2009, MNRAS, 396, 203

Schuster, W. J., Moitinho, A., Márquez, A., Parrao, L., & Covarrubias, E. 2006, A&A, 445, 939

Schuster, W. J. & Nissen, P. E. 1988a, A&AS, 73, 225

Schuster, W. J. & Nissen, P. E. 1988b, A&AS, 73, 225

Schuster, W. J. & Nissen, P. E. 1989, A&A, 222, 69

Schuster, W. J., Nissen, P. E., Parrao, L., Beers, T. C., & Overgaard, L. P. 1996, A&AS, 117, 317

Searle, L. & Zinn, R. 1978, ApJ, 225, 357

Sills, A., Pinsonneault, M. H., & Terndrup, D. M. 2000, ApJ, 534, 335

Sirko, E., Goodman, J., Knapp, G. R., et al. 2004, AJ, 127, 899

Skrutskie, M. F., Schneider, S. E., Stiening, R., et al. 1997, in Astrophysics and Space Science Library, Vol. 210, The Impact of Large Scale Near-IR Sky Surveys, ed. F. Garzon, N. Epchtein, A. Omont, B. Burton, & P. Persi, 25–+

Smolinski, J. P., Beers, T. C., Lee, Y. S., et al. 2010, ArXiv e-prints

Smolčić, V., Ivezić, Ž., Knapp, G. R., et al. 2004, ApJL, 615, L141

Smoot, G. F., Bennett, C. L., Kogut, A., et al. 1992, ApJL, 396, L1

Sneden, C. A. 1973, PhD thesis, AA(THE UNIVERSITY OF TEXAS AT AUSTIN.)

Snider, S., Allende Prieto, C., von Hippel, T., et al. 2001, ApJ, 562, 528

Soderblom, D. R. 2010, ArXiv e-prints

Spite, F. & Spite, M. 1982, A&A, 115, 357

Springel, V., Frenk, C. S., & White, S. D. M. 2006, Nature, 440, 1137

Steinmetz, M., Zwitter, T., Siebert, A., et al. 2006, AJ, 132, 1645

Tabur, V., Kiss, L. L., & Bedding, T. R. 2009, ApJL, 703, L72

Tegmark, M., Taylor, A. N., & Heavens, A. F. 1997, ApJ, 480, 22

Thakar, A., Szalay, A. S., & Gray, J. 2004, in Astronomical Society of the Pacific Conference Series, Vol. 314, Astronomical Data Analysis Software and Systems (ADASS) XIII, ed. F. Ochsenbein, M. G. Allen, & D. Egret, 38–+

Thoul, A. A., Bahcall, J. N., & Loeb, A. 1994, ApJ, 421, 828

Tojeiro, R., Heavens, A. F., Jimenez, R., & Panter, B. 2007, MNRAS, 381, 1252

Tolstoy, E., Venn, K. A., Shetrone, M., et al. 2003, AJ, 125, 707

Unavane, M., Wyse, R. F. G., & Gilmore, G. 1996, MNRAS, 278, 727

Vandenberg, D. A. 1983, ApJS, 51, 29

Vandenberg, D. A. & Bell, R. A. 1985, ApJS, 58, 561

VandenBerg, D. A., Swenson, F. J., Rogers, F. J., Iglesias, C. A., & Alexander, D. R. 2000, ApJ, 532, 430

Weiss, A. 2002, in ESA Special Publication, Vol. 485, Stellar Structure and Habitable Planet Finding, ed. B. Battrick, F. Favata, I. W. Roxburgh, & D. Galadi, 57–64

Weiss, A., Cassisi, S., Schlattl, H., & Salaris, M. 2000, ApJ, 533, 413

Weiss, A. & Salaris, M. 1999, A&A, 346, 897

Weiss, A., Salaris, M., & Rohr, D. 2005, in IAU Symposium, Vol. 228, From Lithium to Uranium: Elemental Tracers of Early Cosmic Evolution, ed. V. Hill, P. François, & F. Primas, 279–280

Weiss, A. & Schlattl, H. 2000, A&AS, 144, 487

Weiss, A. & Schlattl, H. 2008, ApS&SS, 316, 99

Wilhelm, R., Beers, T. C., & Gray, R. O. 1999, AJ, 117, 2308

Wylie-de Boer, E. & Freeman, K. 2010, in IAU Symposium, Vol. 262, IAU Symposium, ed. G. Bruzual & S. Charlot, 448–449

Yanny, B., Newberg, H. J., Johnson, J. A., et al. 2009a, ApJ, 700, 1282

Yanny, B., Rockosi, C., Newberg, H. J., et al. 2009b, AJ, 137, 4377

Yong, D., Meléndez, J., Cunha, K., et al. 2008, ApJ, 689, 1020

York, D. G., Adelman, J., Anderson, Jr., J. E., et al. 2000, AJ, 120, 1579

Zhao, G., Chen, Y., Shi, J., et al. 2006, Chinese Journal of Astronomy and Astrophysics, 6, 265

Zinn, R. & West, M. J. 1984, ApJS, 55, 45

Acknowledgments

The achievement of this work was only possible because of my supervisor Achim, who gave me the opportunity to come to Germany. I really appreciate how he insisted during the entire course of the thesis in "you must answer a scientific question". This made me learn to see beyond the tools and understand my topic. I am also very grateful to his support during my pregnancy and maternity leave and also for supporting my career. Additionally, the opportunity to come to Garching provided by the IMPRS program, together with the great MPA facilities were crucial to develop this work, for which I am grateful. The MPA also gave me the possibility to do a maternity leave, because I knew that my project and place here was save. I thank the MPA directors S. White, M. Asplund and W. Hillebrandt for being helpful during this entire period in many different aspects. Finally, I thank M. Kissler-Patig for being the second corrector of this thesis.

The advises and discussions with C. Allende Prieto were very fruitful in the development of this work. I also feel thankful with R. Gray, J. Sobeck, Y. Sun Lee, P. Demarque, Y. C. Kim, Z. Magic, M. Salaris, I. Ramirez, L. Sbordone, R. Collet and the SAGA group, for the exchange of ideas and programs. A. Reisenegger and B. Panter deserve a special thank because they have also supported my career. Finally, I want to thank Frau und Herr Meyer, Benedetta, Cornelia, Gabi and Maria for always asking me how things were going.

I am extreme grateful to Thomas, he read and questioned every single small detail of this work. His faith on me was one of the major motivations to give the best of me and achieve this PhD. This thesis is the result of working together, supporting each other as a "family project". In addition, I am very grateful to Damian. He did not really attempted to help me with the thesis, but he did. He offered me every day peaceful breaks and put my main the priority in being calm and happy. Because of him I realized that I was doing this PhD because I wanted to, which made me enjoy this thesis sincerely.

The good friends gained in Munich, Margarita, Payel, Fede, Michi, Eva, Julius, Rob, Dayela and Noah; Bogdan, Bere, Raul, Hauke, Heike($\times 2$), Paco and Paulinchen made my life in Munich just great. I want especially to thank Payel for the careful English corrections of the different documents written during this thesis and Andreas for his constant help during this time. I also want to thank Camilla and Monique, for their friendship and scientific discussions; the "latino lunch" and my old friends Paola, Timo, Manuel, Ignacio, Raul, Cata, Nacha, Andrea and Karin, for their company. I am grateful to Frank, Eva, Andrea, Usahma and Noaman for give me a family in Germany. I finally feel very thankful to my parents because they gave me the wings to come here for my PhD; and to my sisters Caro and Vale, to support me to stay here, even in the most critical moments.